

POLITECNICO DI TORINO

Corso di Laurea Magistrale in Ingegneria Aerospaziale



Tesi di Laurea Magistrale

Energy-Absorbing Origami Structure for Crashworthiness Design

Relatore:
Prof. Giacomo Frulla

Candidato:
Leonardo Marconi

Correlatore:
Prof. Enrico Cestino

Supervisore esterno:
Prof. Jae-Hung Han

Anno Accademico 2021/2022



Smart Structures & H/W Systems Laboratory

Declaration

The thesis entitled “Energy-Absorbing Origami Structure for Crashworthiness design” is carried out at the Smart Structures and H/W Systems Laboratory (Korea Advanced Institute of Science & Technology) in Daejeon, under the supervision of Professor Prof. Jae-Hung Han.

This document has been reviewed and determined not to contain export-controlled technical data. I hereby declare that except where specific reference is made to the work of others, the contents of this dissertation are original and have not been submitted in whole or in part for consideration for any other degree or qualification in this, or any other university.

Acknowledgments

I am truly grateful to Professor Jae-Hung Han, that welcomed me in his lab, guiding me into this exciting and mind-broadening experience. Your support, advice and consideration have been extremely important and profoundly appreciated. I felt really honoured to work with you.

My sincere gratitude to my advisor, Professor Giacomo Frulla, for sharing his deep experience with me and for the constant help throughout the thesis even from the other side of the globe. I am also really thankful to Professor Enrico Cestino for all the hours spent on video call.

Ai miei genitori, instancabili sostenitori da una vita, a cui devo i miei traguardi più alti. Un grazie sincero per aver sempre creduto in me ed avermi incoraggiato ad inseguire i miei sogni più impensabili. Non avrei potuto essere circondato da persone migliori.

A huge thanks to Yongha and to my nicest labmates for taking care of me in Korea.

To my friends in Tuscany, Turin, Daejeon and somewhere around this wonderful world.

I owe these years of deep change and invaluable satisfactions to all the nice people that passed through my life, leaving precious lessons and unforgettable memories.

I consider myself immensely fortunate to have met you along this path.

Table of Contents

Abstract.....	V
INTRODUCTION.....	VI
NOMENCLATURE	IX
1. CRASHWORTHINESS DESIGN.....	1
1.1 Energy-absorbers for rotorcraft application	3
1.2 Origami as energy absorption device	6
2. ENERGY ABSORBING ORIGAMI LITERATURE REVIEW.....	8
2.1 Thin-walled tubes crashworthiness design	8
2.1.1 Tubes buckling modes	8
2.1.2 Geometric patterns.....	13
2.2 Diamond-Mode Origami	15
2.2.1 Theoretical analysis	15
2.2.2 Geometry and Parametric analysis	17
2.2.3 Manufacturing method	21
2.2.4 Diamond mode stability.....	23
3. EXPERIMENT ON SLM MANUFACTURED SPECIMEN.....	28
3.1 Test aim and objectives.....	28
3.2 Specimens characteristics	29
3.2.1 Geometry	29
3.2.2 Manufacturing process	30
3.2.3 Materials	33
3.3 Quasi Static test settings.....	39
3.4 Numerical analysis	42
3.4.1 Explicit FEM	42
3.4.2 FEM model settings.....	49
3.5 Results	56
3.5.1 Experimental test on straight cylindrical tube	56
3.5.2 Experimental test on AlSi10Mg origami tube	57
3.5.3 Experimental test on SUS316L origami tubes.....	59
3.5.4 Comparative analysis with FE model for SUS316L origami	65
3.6 Considerations	71
4. DESIGN EXPLORATION.....	73
4.1 Goals and methodology	74
4.2 Correlation and model creation	76
4.2.1 Parametric Geometry.....	76

4.2.2 FE model	78
4.2.3 Parameter correlation.....	80
4.3 Optimization	85
Conclusions	91
References	94
List of figures	97

Abstract

This thesis presents an experimental and numerical investigation on the novel origami-patterned tube which is recognised as a promising energy absorption device. Its peculiar buckling mode leads to high performances in terms of specific energy absorption (SEA) and crushing force efficiency (CFE). The mode is triggered by prefolding a polygonal tube following an origami pattern, which is designed to act as geometric imperfection and mode inducer, to flatten the buckling force peak and to trigger a predictable and efficient “diamond crushing mode”.

The current work represents the first step in evaluating a potential application of the origami tube as crashworthy component on a Personal Air Vehicle, currently under development at the hosting university.

Two approaches are employed for this preliminary study:

First, a series of quasi-static crushing tests are performed on origami tubes with different materials and geometrical features. Specimens in SUS316L and AlSi10Mg are produced through Additive Manufacturing (AM), which allows to conveniently produce few samples with a complex shape. Finite Element Analysis (FEA) and Direct Image Correlation (DIC) are employed for a better insight into the complex crushing behaviour. The Aluminium tube shows a brittle behaviour while SUS316L specimens have extremely promising performance until local crack happens. Limits stemming from the employment of AM are explored and a new geometry is designed to avoid cracking.

Second, a numerical design exploration study is carried out to assess the sensitivity of origami pattern features over the energy-absorption performance. ANSYS Autodyn is utilized as explicit FE solver and the DesignXplorer tool for correlation and optimization. Benefits of new patterns are investigated through geometrical optimization, and an improved geometry is eventually proposed. The pattern stiffness is tuned to account for the external boundary conditions, resulting in a more uniform crushing behaviour. The optimised pattern force trend is maintained similar to the reference geometry while SEA is incremented by 51.7% due to a drastic weight reduction in areas with lower influence on post-buckling stiffness. The origami tube behaviour under dynamic loading, and the differences with the quasi-static case are eventually explored.

Keywords: Origami, CFE, SEA, Explicit FEA, Crashworthiness, Additive Manufacturing, Diamond Buckling Mode, Optimization.

INTRODUCTION

The present investigation is the starting point and a feasibility study for a future application of origami-patterned tubes as crashworthy components on a Personal Air Vehicle which is currently in its conceptual design phase at the hosting university.

A crashworthy design has become a main requirement for all manned vehicles, in particular, for helicopters it has always remained a top priority to prevent casualties [1]. The structure must be designed to lower accelerations on the occupants in the event of crash, until a survivable level. Therefore, an energy-absorbing device capable to reduce the magnitude of acceleration is fundamental to this end.

The origami-patterned crash box is a thin-walled energy-absorber which dissipates energy through its extensive plastic deformation. The prefolded origami pattern is designed to trigger the high Specific Energy Absorption (SEA) “diamond mode” and to act as induced geometrical imperfection to flatten the initial buckling force, resulting in high Crush Force Efficiency (CFE) and mode predictability. Recent investigations show the high potential of origami configuration. Numerical optimizations through explicit FEM analysis exhibit CFE up to 90% [2] and SEA up to 87% higher than the conventional square tube or 49% higher than the hexagonal configuration [3]. High performances, low weight and convenient manufacturability make this configuration a potential candidate for this aeronautic application.

The first chapter introduces the crashworthiness problem and the relevant performance indicators. A brief overview on helicopter crashworthiness design is also given, since the requirements for eVTOLs in fully rotorcraft configurations are expected to follow the already existent EASA CS-27 applicable to conventional small rotorcrafts [4]. Finally, the origami configuration is introduced as alternative approach to traditional energy-absorber devices

A literature review on the state-of-the-art of energy-absorbing structures, with a focus on origami tubes is performed. The outcomes of several publications are examined in the second chapter. C. Zhou and B. Wang performed quasi-static [5] and dynamic [6] compression of origami tubes, their outputs are also used for validation in a later stage of the thesis. J. Ma set a theoretical approach for describing the origami crushing [3] [7], whose terminology is also used in this dissertation. Together with the theoretical approach, the pattern influence is explored through numerical studies on various geometries [2] [8]. Finally, real-scenario effects such as geometrical imperfections [9] and oblique loads [10] are presented.

Two approaches are adopted in this preliminary study.

On the third chapter a series of quasi-static crushing tests are performed on origami tubes with different materials and geometrical features. Metal Additive Manufacturing was individuated as a cost-efficient method to produce a small batch of complex specimen and to have possibility of conveniently printing different geometries in view of a future optimization study. Two additive materials are chosen, AlSi10Mg aluminium alloy and SUS315L stainless steel. Finite Element Analysis (FEA) and Direct Image Correlation (DIC) are employed for a better insight on the crushing behaviour. The aim of this experimental phase is to study the behaviour of 3D printed origami tubes as energy absorbing devices and to use the results to validate the numerical FE model.

The aluminium specimen reveals a brittle behaviour which results in extensive crack nucleation and propagation, resulting in a sharp drop of energy-absorbing. The stainless-steel origami, characterized by excellent mechanical properties in terms of strength and elongation, also exhibits localised fractures at the lobe corners under tension.

The problem of stress concentration at the corners under tensile stress is numerically analysed and a revised geometry is eventually printed and tested. The new geometry is characterised by rounded edges and lower wall thickness which is expected to overcome the issue by enlarging the area undergoing deformation at the plastic hinge. Cracks appear in a much lower extent also in the revised specimen, which however partially preserve its stiffness.

Influence of pattern features, and material property uncertainty are numerically examined at this phase. Despite its convenience and accurate geometric tolerances, the Additive Manufacturing process imposes heavy limitations in terms of available materials, material properties uncertainty and minimum wall-thickness, which undermine the employment of 3D printing for producing effective energy-absorbing origami tubes.

Finally, on the fourth chapter, a numerical design exploration study is carried out with the aim of investigating potential benefits of a new pattern and to assess the sensitivity of origami features over SEA and CFE. Four geometrical parameters are studied, of which a new parameter is introduced with the aim of tuning each pattern segment according to their own boundary conditions.

The study suggests that tube stiffness is highly dependent on the lobe's geometry, in which most of the plastic deformation is concentrated. An optimized origami pattern is proposed, in order to achieve a similar mean and maximum force with a lower structural weight.

The experimental work from C. Zhou and B. Wang [5] (carried out on stamped mild-steel origami) is adopted for the FE model validation, while a stamping method based on embossing and folding is currently under development at the hosting university. Boundary conditions of the FE model are chosen to reflect the real application on the PAV and the material model is chosen to conveniently account the strain rate sensitivity at a later design stage.

A dynamic case is also run at the end of the chapter, for validating the optimization output. The buckling mode does not differ from the quasi-static case, even though the force reaction is offset at higher values due to the material strain rate hardening.

NOMENCLATURE

SEA	Specific energy absorption
CFE	Crushing force effectiveness
F_{max}	Maximum crushing force
F_m	Averaged crushing force
E_{abs}	Absorbed energy
W	Weight
t	Wall thickness
b	Side length
c	Origami lobe length
c_1, c_2	Trapezoid origami lobe lengths (sides, centre)
l	Module height
M	Number of modules in series
h	Tube height
δ	Crushing stroke
ϑ	Prefolding angle
α	Oblique load angle
α_{max}	Maximum oblique load angle for mode stability
A	Area
E	Young modulus
σ_Y	Yield stress
σ_{UTS}	Ultimate tensile stress
ν	Poisson's ratio
ε_p	Plastic strain
$\dot{\varepsilon}$	Strain rate
K	Ludwik equation strength coefficient
n	Ludwik equation strain hardening exponent
D	Cowper-Symonds strain rate hardening coefficient
q	Cowper-Symonds strain rate hardening exponent
EBM	Eulerian Bending Mode
(c_2/c_1)	Lobe aspect ratio
(h_{int}/h_{ext})	Module heights ratio
FEA	Finite Element Analysis
DIC	Digital image correlation

1. CRASHWORTHINESS DESIGN

The capability of a structure to manage and absorb the force of a serious crash and to reduce death and injury risk of the occupants is known as crashworthiness. The vehicle should be designed to decrease forces and accelerations on the human body below its survivability limit in the event of crash, preserve a safe volume inside the cabin and control the leakage of flammable liquids [11]. A crashworthy design has become a main safety criterion of the occupants-carrying vehicles such as aircraft, trains and cars. Their structure needs to be capable to reduce the magnitude of acceleration acting on the occupants through converting most of the kinetic energy during a crash situation into other forms of energy in a predictable and controllable fashion.

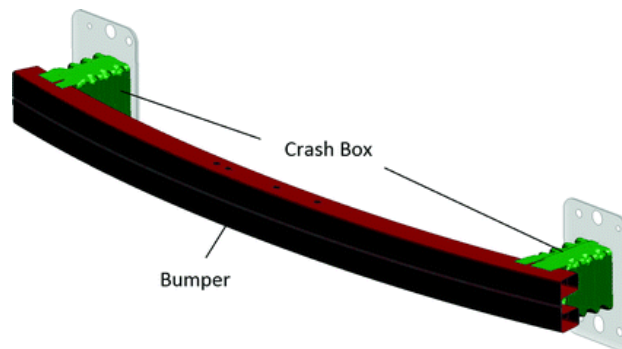


Figure 1 Typical car frontal bumper assembly configuration [12]

The most common energy absorber components, that are widely used to absorb kinetic energy and to improve the crashworthiness behaviour of a structure, are the thin-walled components. The widespread use of such components in crashworthiness design is due to several important aspects including superior performance under dynamic loading, cost-effectiveness, high efficiency, ease of manufacturing and installation [7].

It is important to observe that thin-walled members like plates, tubes, stiffeners and sandwich panels are already commonly employed in designing automobile bodies and aircraft fuselage structures [13].

Several characteristics are demanded to energy-absorbing components. The two primary performance parameters are the overall energy absorbed per unit of mass, called Specific Energy Absorption (SEA) and ratio between the maximum reaction force and the mean crushing force, called Crush Force Efficiency (CFE). An ideal absorption device has CFE=1, hence it is capable to transfer a constant load to payload, passenger, fuel tank, battery or any other sensitive part of the vehicle. The energy absorption is dependent on mean force and effective crushing stroke of the absorbing device, before it bottoms out.

The main characteristics demanded to an energy-absorber device are the following:

- Specific Energy Absorption (SEA):

$$SEA = \frac{E_{absorbed}}{W_{structure}} = \frac{\int_0^{\delta_{stroke}} F(x) dx}{W_{structure}} \quad \left[\frac{kJ}{kg} \right] \quad (1)$$

- Crush Force Efficiency (CFE):

$$CFE = \frac{F_{mean}}{F_{max}} \leq 1 \quad (2)$$

- Range of mode stability under oblique load
- Stable and repeatable deformation mode to ensure predictable performance
- Low manufacturing cost and convenient replaceability

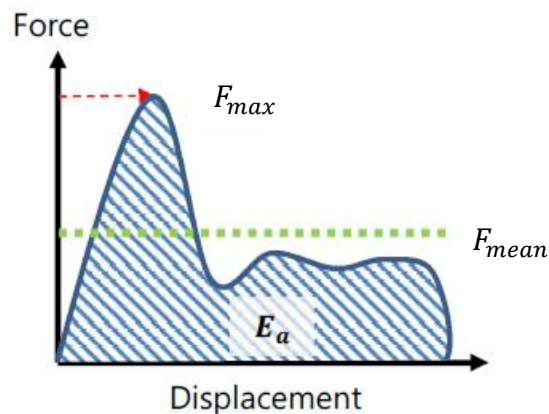


Figure 2 Qualitative thin-walled structure crushing behaviour

1.1 Energy-absorbers for rotorcraft application

The European Union Aviation Safety Agency (EASA) prescribes specific crashworthiness requirements for small rotorcrafts in the CS-27 regulation, which are imported from the corresponding US Federal Aviation Administration FAR-27. CS-27 involves a relation between impact velocity and survivability from which the main requirements are derived. *CS-27.561/562* deals with occupant protection while *CS-27.952* sets requirements for the energy storage assembly [14].

- *CS-27.562* requires the dynamic test of the crashworthy assembly (subfloor and seat on traditional helicopters) and the measurement of resulting loads, in particular, the lumbar spine load of a test dummy installed on the seat. The assembly is subjected to a 30 g acceleration pulse introducing a 9.1 m/s speed change (95th percentile of survivable crash occurrence), applied with a load pitch angle of 30° [11].
- *CS-27.952* aims to minimize hazards to occupants caused by the energy storage system in an otherwise survivable crash landing. The energy storage assembly is dropped from 15.2 m, (99th percentile of survivable crash occurrence), crashing on a 10° oblique rigid surface. The original *CS-27.952* which accounted only fuel tanks, will be extended to gaseous and solid storage systems, such as batteries. Post-crash fire and harmful substances leakage must be prevented in the drop test [4].

During a crash landing, the load is transferred from the ground to the occupants passing through landing gears, subfloor and dynamic seat which are designed to maintain a maximum value at the seat level in the range of 4500– 5500 N, to keep the lumbar load under the tolerable limit of 6670 N [15]. In a perfectly rigid case, the reaction force on the occupant spine would be considerably higher than the safety limit, therefore, all rotorcrafts are equipped with energy-absorbing systems, usually based on some metal plastic deformation.

Dynamic seat

During a crash landing, seat is the main responsible for the load transfer to the occupant and, therefore seats on helicopters are integrated with a set of energy absorbers. The most important factor that defines the seat response in a crash landing is the activation load of these energy

absorbers. The vertical motion is limited by the available stroke, that should not be fully exploited in order to avoid the device bottoming out and its consequent surge in reaction force which typically introducing a spinal overload [16]. Currently, almost all the military and many of the civil helicopters in are equipped with crashworthy energy absorbing seats that make use of different method for the energy dissipation. Some of them are shown in the picture below.

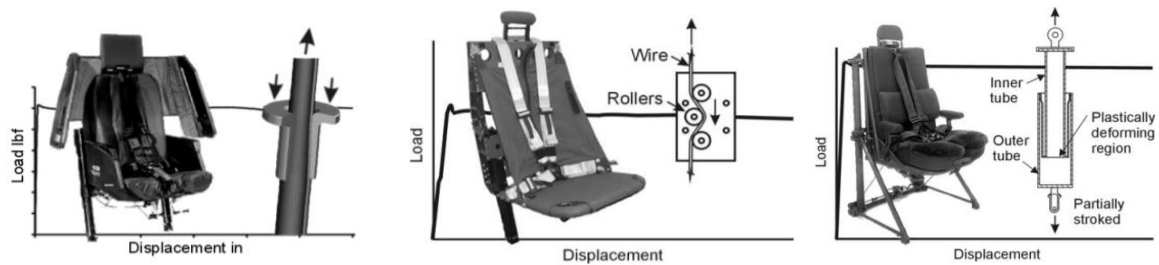


Figure 3 Crashworthy seat energy absorbing devices [16]

Subfloor

The design of this structure may contribute essentially to the overall crash response. It is integrated inside the fuselage belly under the cabin floor, and it is usually made of keel beams and transverse bulkheads. Subfloor provides an important space that could be exploited for energy absorption, if properly sized. The dynamic load of the full rotorcraft during a ground impact must trigger the buckling in the subfloor structure, which should keep crushing at constant load, still preserving its structural integrity.

Safety regulations issue only general recommendations with no specific certification tests on the subfloor assembly, however, the mutual interaction between the subfloor and seat could drive better design solutions [17].

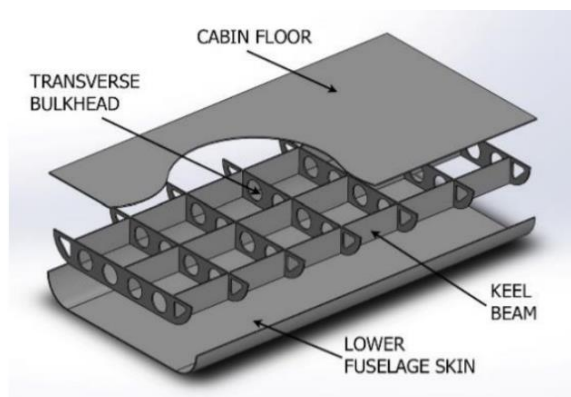


Figure 4 Helicopter subfloor layout [11]

Landing gear

This is the first element involved in the impact, and it significantly contributes to absorb the energy developed during the crash. Conventional landing gears are also equipped with special energy absorbers integrated in the shock absorbers. The work of M. Guida et al. [18] shows an interesting application for an auxiliary energy absorber which is coaxially bounded to the shock absorber. It is capable to enhance the energy absorption and reduce the bottoming out effect with only a little increment of mass. A similar example comes from Alessandro Airoidi [19] which studied a landing gear configuration based on a collapsible thin-walled energy absorber. In recent times, energy absorbers that make use of material plastic deformation are also employed for the vertical landing of reusable launch vehicles.



Figure 5 SpaceX Starship SN6 energy absorbers [20]

Possible aerospace crashworthiness applications of thin-walled structures have been introduced in this section. It is important to note that even though this chapter focusses on aeronautical applications, the automotive regulation also required high speed crashes at similar impact velocity [21]. UNECE requires a 56 km/h impact test, which is similar to the 9.1 m/s and 15.2 m/s of CS-27.562 and CS-27.952 applicable to small rotorcrafts [14].

1.2 Origami as energy absorption device

Origami is the traditional Japanese art of producing complex 3D models through exclusively folding paper sheets. The sheet can be formed into an infinite type of shapes following specific crease patterns. Nowadays, this ancient technique is employed in several engineering fields, with significant applications in controlling the deformation process and final configuration of thin sheet structures, as in the case of deployable structures.

A novel application of the origami pattern is found in the field of thin-walled energy absorbing devices. While straight tube requires a great force to be crushed axially, an origami patterned tube can be folded with ease if the pattern is carefully selected and its crushing follows the given pattern. Therefore, a proper pattern can be used to direct a thin-walled tube to collapse in a desired failure mode which involves extensive material plastic deformation, hence leading to increased energy absorption. A comparison between thin-walled straight tubes and origami energy absorbers clearly demonstrates the strong correlation between collapse mode and energy absorption capability [7].

The origami patterned crash box is recognized as a promising energy absorption device. It is capable to induce the cylindrical tube's peculiar buckling mode known as diamond mode which leads to high performances in terms of specific energy absorption (SEA). Furthermore, it acts as induced geometrical imperfection, hence eliminating the buckling force peak and increasing the crushing force efficiency (CFE), achieving a predictable and efficient collapsing mode. For this purpose, a particular rhomboid origami pattern is created on the corner edges of polygonal tubes.

The pattern can be conveniently manufactured from a sheet of metal without extensive plastic deformation, offering a cost-effective and high-performance solution in large scale production. Although the origami geometry offers a wide design space for optimization, many factors may affect its performance in a real application scenario, such as manufacturing imperfections, oblique load and impact velocity. An intensive study has been recently performed to assess strengths and weaknesses of the origami crash box configuration.

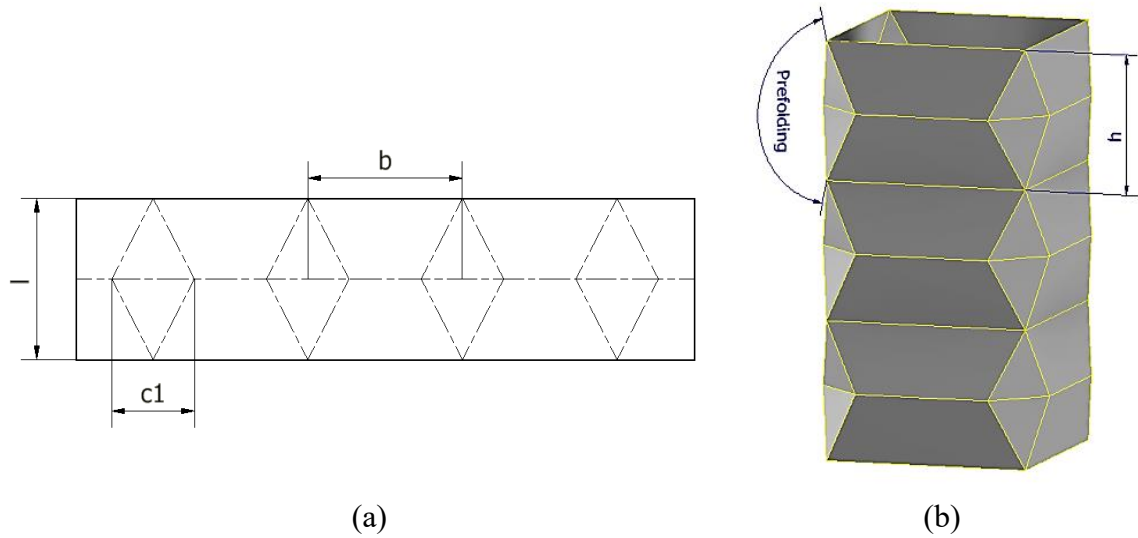


Figure 6 Origami patterned tube: (a) 2D folding lines on metal sheet, (b) folded tube

2. ENERGY ABSORBING ORIGAMI LITERATURE REVIEW

In this section a review of previous works and publications is presented, which represent the current state of the art and the starting point of my thesis. The first chapter deals with the behaviour of thin-walled structures for energy absorbing application. An overview on buckling modes is also given for a better understanding of the working principle of the origami patterned tube. The second chapter focuses on the origami configuration.

2.1 Thin-walled tubes crashworthiness design

By definition, an energy absorber is a system that converts, in a certain extent, kinetic energy into another form of energy. The conversion of energy can be either reversible, like pressure in compressible fluids and elastic strain in solids, or irreversible, such as material plasticization. It is known that thin-walled structures, and in particular circular tubes under axial compression provide a superior specific energy absorption capacity, therefore they are the most frequently used in energy absorbing systems [13]. The most important phenomenon from the perspective of energy absorption is the post-buckling crushing behaviour, when the tube undergoes large plastic deformations, and a major portion of the energy dissipation occurs.

2.1.1 Tubes buckling modes

An overview on natural buckling modes of straight tubes as given in order to gain a better understanding of the origami patterned tube working principle, which is studied in detail in a later section.

Buckling is an instability phenomenon which affects structures under compressive loads, typically slender or thin-walled structures, making them collapse following particular geometric patterns.

Slender tubes tend to buckle globally under “Euler Buckling” resulting in a sideward bending. The critical buckling load of a pinned slender beam can be estimated by the formula:

$$F_{crit} = \frac{\pi^2 E I}{h^2} \quad (3)$$

Based on their dimension, thin-walled tubes can also undergo global bending deformation mode during their axial crushing, this mode is very inefficient and should be avoided when designing an energy absorption structure because it is relatively unstable and it can lead to a considerable decrease in the effectiveness of the absorbing device [22]. The global bending deformation mode may occur in both square and polygonal tubes. The occurrence of global bending in axially loaded circular tubes depends on the diameter to thickness (D/t) and length to diameter (L/D) ratios [23].

Experimental observations on non-slender tubes, show that relatively thick cylinders (low D/t) fall in extensional mode as shown in Fig. 7(a), whereas thin cylinders (high D/t) collapse elastically in diamond mode as shown in Fig. 7(b). For the rest, the mixed mode usually takes place [24].

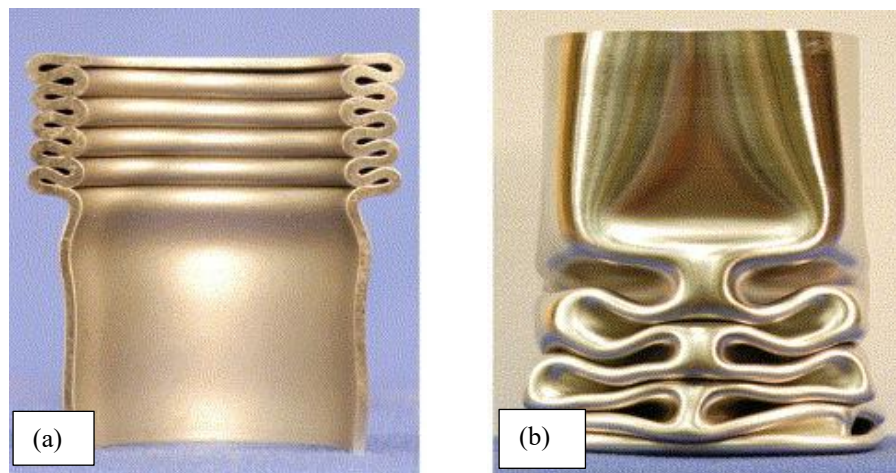


Figure 7 Cylindrical tube buckling modes: (a) Concertina, (b) Diamond [25]

When a square tube buckles, each side of the tube deforms into several axial waves. Each corner of the tube remains at right angles, indicating that there is no bending moment at the corner side and therefore each face of the tube can be treated as a plate simply supported at its edges [26]. Furthermore, very thin square tubes as well as cylindrical tubes typically with $b/t \approx 100$, may trigger a non-compact deformation mode dominated by large irregular folds, which is an undesirable mode for energy absorption, and it should be avoided [22].

In the same fashion as circular tubes, thicker squared tubes usually fail in an extensional mode. However, commonly employed thin-walled square tubes tend to assume an inextensional failure mode, the so-called symmetric/ asymmetric modes Fig. 8 (a,c,d). In fact, for thin-walled square tubes, the circumferential membrane deformation requires much more energy to be activated than bending [7].

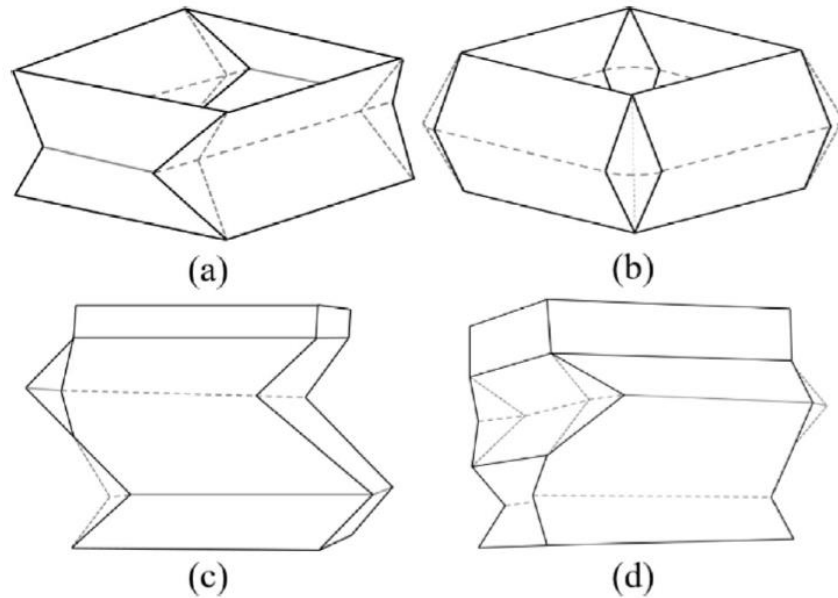


Figure 8 Squared tube buckling modes: (a) symmetric, (b) extensional, (c-d) asymmetric [27]

When a thin-walled straight tube crushes subjected to a compressive load, three main deformation mechanisms occur: stationary or travelling plastic hinge lines for diamond mode, symmetric mode and extensional mode and circumferential extension for extensional mode. Circumferential extension is efficient in terms of energy absorption but hard to be activated in thin-walled tubes since a sheet is more easily bent than stretched. Traveling plastic hinge line is responsible for two-thirds of total energy absorption in squared tube collapsing in the symmetric mode [28].

The mean crushing force can be estimated analytically through the super folding element procedure introduced by Wierzbicki and Abramowicz for the extensional and inextensional modes [7]. However, straight tubes, are highly dependent on initial imperfections. At the present time the values of buckling loads determined by experimental tests differ appreciably from the computed values, no matter what theory we use [29].

An extensive quasi-static experimental campaign on octagonal tubes shows the buckling modes typical of both square and circular tubes (such as concertina, diamond and symmetric/asymmetric). It is also found that their SEA is much higher than square tubes and close to the one of cylinders [30]. The influence of number of edges in polygonal tubes is investigated by Yamashita et al., which emphasises the enhancement of energy absorption when the number of corners increases, with a more pronounced effect as the wall thickness decreases [31]. A regular diamond mode is triggered for a number of edges higher than five, and a behaviour almost identical to the cylinder is achieved for a number of edges higher than eleven.

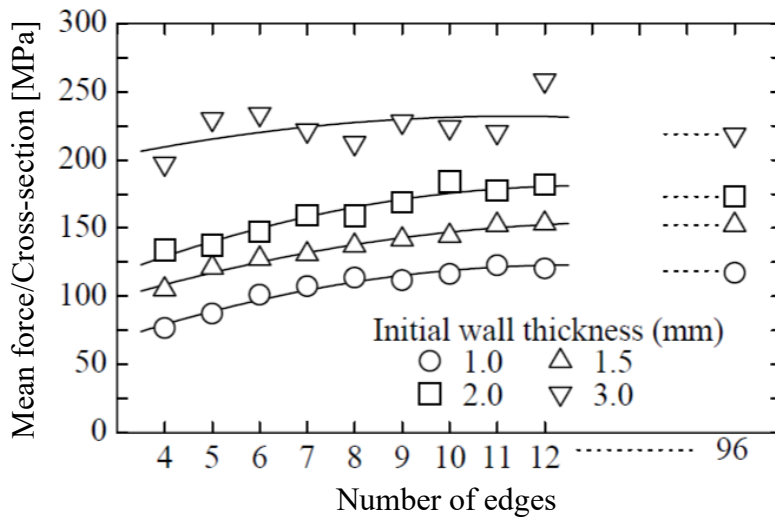
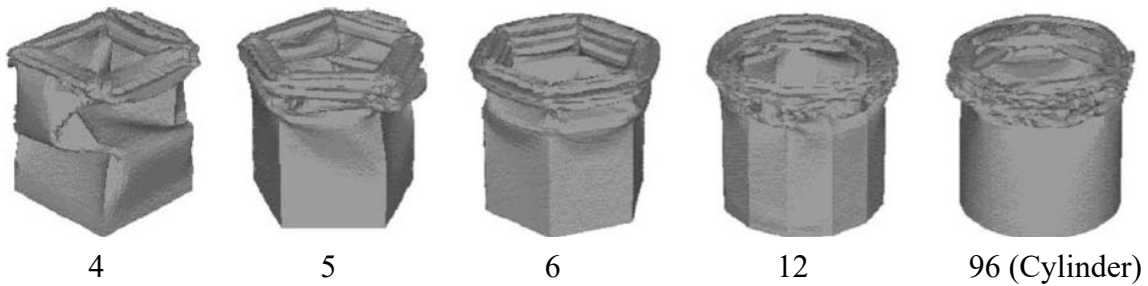


Figure 9 Deformed shape and specific mean force of polygons, with different number of edges and wall-thickness [31]

Tapered tubes are widely employed as energy-absorbing devices because of their stable response under oblique loads. Energy absorbers are subjected to oblique loading in real impact applications and therefore the behaviour under oblique load must be considered. As already discussed, the aeronautic regulation requires a crash test under non-axial condition. A critical oblique load angle was reported for tubes to indicate the transition from axial progressive folding to Eulerian global bending collapse, which implies a sharp drop in energy absorption capability [32].

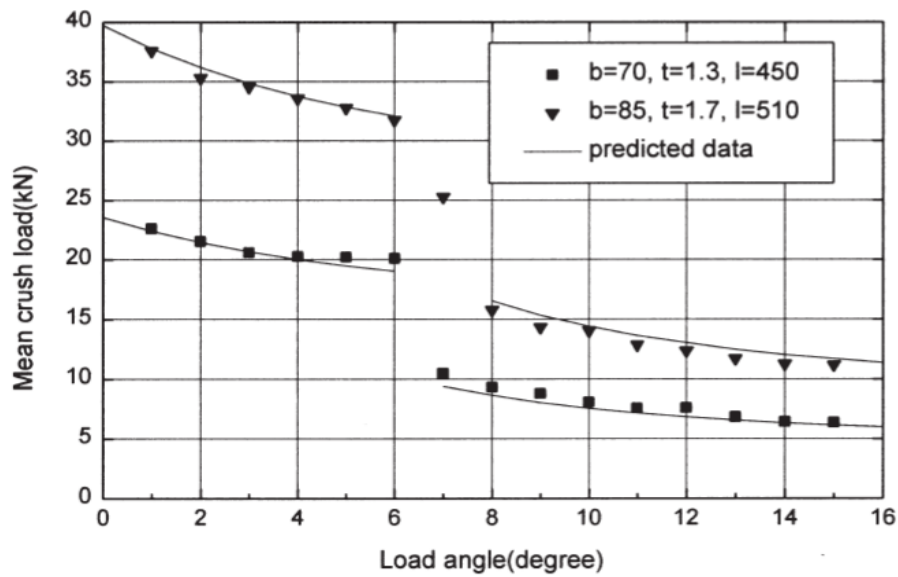


Figure 10 Mean force under oblique load for squared tubes [32]

Xiong Zhang and Hui Zhang also explored absorbing properties and critical oblique load angle of tapered circular tubes with graded wall-thickness under oblique dynamic load. For low taper values, the geometry does not effectively affect the reaction force trend under axial loading, but it drastically influences, together with the hardening due to the forming process, the behaviour under oblique load. An increment 80 % in energy absorption is found for loading angle of 15° [33].

2.1.2 Geometric patterns

In the past few decades, conventional tubes have been widely studied and used in vehicles crashworthiness design, such as squared and circular tubes. The collapse modes of those thin-walled structures belong to the category of natural modes (shape and wavelength are formed naturally) which suffer from high peak force or low energy absorption. Enhanced crashworthiness performance can be achieved by properly modifying the geometry, in order to trigger a non-natural buckling mode. Hence, some tubes with relatively complex geometry, such as multi-cell, tapered or patterned tubes have been proposed and studied as alternative designs to obtain higher absorption while maintaining a flat force trend.

Simple and effective design solutions involve the introduction of geometrical imperfection such as holes, dents or corrugations in the geometry. These geometrical discontinuities are designed to reduce the buckling force and act as buckling mode initiators. However, the specific energy absorption can be considerably lower than that of the corresponding straight tubes, like in the case of corrugated tubes [34].

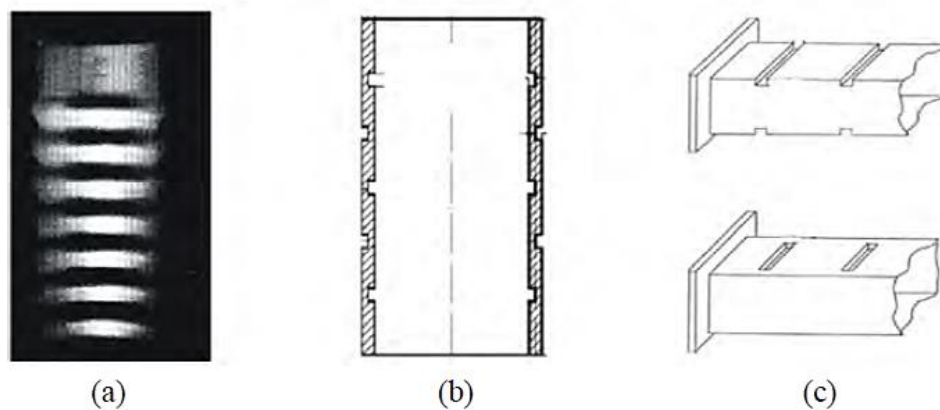


Figure 11 Tube patterns: (a) Corrugated tube, (b) Grooved tube, (c) Dented tube [7]

The structural response of a thin-walled structure is directly correlated to its specific failure mode. Therefore, several geometric patterns are proposed to trigger desirable buckling modes, such as extensional or diamond mode, that would not be naturally generated by the tube without such a pattern. Some examples of buckling initiators are ribs, pre-hit column initiators, kirigami pattern or origami pattern.

The working principle of the diamond-mode origami pattern is to induce a specific buckling mode by pre-shaping the tube with the post-buckling geometry of the desired “diamond mode”. The magnitude of the initial imperfection and wavelength of the mode are predefined by properly designing the origami pattern from which the tube is created.

The origami patterned configuration shows excellent properties in term of CFE and SEA. Furthermore, the manufacturing process is comparable with the one employed for conventional crash boxes, and it can be conveniently produced in large scale through stamping and welding. However, it suffers from local or global instabilities due to several factors, which may hinder its performance.

Some alternative origami concepts are also recently proposed, such as the Kirigami pattern [27]. This pattern is capable trigger an efficient extensional mode in thin-walled square tubes, in the range of thickness to edge ratio suitable for energy absorbing devices, while the natural extensional mode would appear only in thick square tubes [35]. Experimental quasi-static tests conducted on the Kirigami pattern show a CFE up to 72% and a SEA increment of about 30% (compared to the squared tube), while additional numerical optimizations achieve SEA increments as high as 250%.

2.2 Diamond-Mode Origami

Recent studies demonstrate the high potential of the origami configuration in comparison with straight tubes, conventionally employed in crashworthiness design. Numerical optimizations through explicit FEA achieved SEA up to 87% higher than the conventional square tube [2] or 49% higher than the hexagonal configuration [3], while CFE can be increased up to 90% [2].

This chapter presents a review of recent publications about the thin-walled origami with diamond pattern. Section 2.2.1 illustrates the theoretical basis through the super-folding element theory of the origami pattern subjected to axial compression. Section 2.2.2 presents the qualitative influence of geometric parameters on the overall performances by referring to previous studies of geometric sensitivity. Section 2.2.3 deals with the manufacturing methods involved in the production of the origami pattern. The ease in manufacturing is recognized as a strength for the origami energy absorber. Section 2.2.4 introduces several critical factors that can induce instabilities in the diamond buckling mode, strongly affecting the overall performances.

2.2.1 Theoretical analysis

A first theoretical approach from Wierzbicki and Abramowicz [36] established a kinematically admissible and circumferentially inextensional element [7] shown in Figure 12 also known as “super folding element”. Two types of plastic hinge lines are considered in the element construction: “stationary plastic hinge lines” which do not move throughout the folding stroke and “travelling plastic hinge lines” which move as the element collapses. The energy dissipation of the super folding element comes from three sources: folding across stationary plastic hinge lines, propagation of travelling plastic hinge lines, and localized in-plane stretching.

The theoretical approach acknowledges the plastic hinge lines movement as the main contribution to energy absorption. The formation of large plastic deformation is limited to the areas swept by the traveling plastic hinge lines and the neighbourhood of the stationary plastic hinge lines, whereas the remaining panels undergo small plastic deformation.

The contribution of shell in-plane deformation and bending, that is neglected in the theoretical approach, is analysed by Zhou et al. [5] through experiments, using strain gauges. The study reveals that only about 10% of the total energy is dissipated in the shells.

Recently, Jiayao Ma et al. [3] derived a theoretical solution to estimate the energy absorption of the origami crash box using the super folding element theory, dividing the crushing process in two successive steps. The energy absorption is found by the superposition principle, considering the contribution from the various energy abortion sources. During the first stage, traveling hinge lines account for most of the absorbed energy, and their contribution is strictly dependent on the “swept area”; the area crossed by the travelling hinge lines movement.

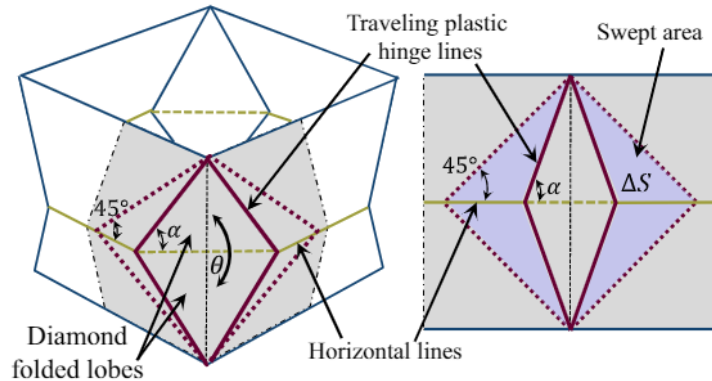


Figure 12 Single module origami: first crushing stage [37]

A qualitative description of the complex folding process is crucial for its understanding:

- The first stage is characterized by a lobe expansion. Travelling hinge lines (thick red line in Fig. 13.a) move until they reach $\alpha \approx 45^\circ$. During the first phase a second contribution from the circumferential stationary hinge line at the middle folding of the module is considered (thick black line in Fig 13.a).
- The second stage starts when the lobe is fully expanded. Many stationary plastic hinge lines (thick lines in Fig 13.b) are formed at this stage. The basic folding element is crushed entirely until it bottoms-out.

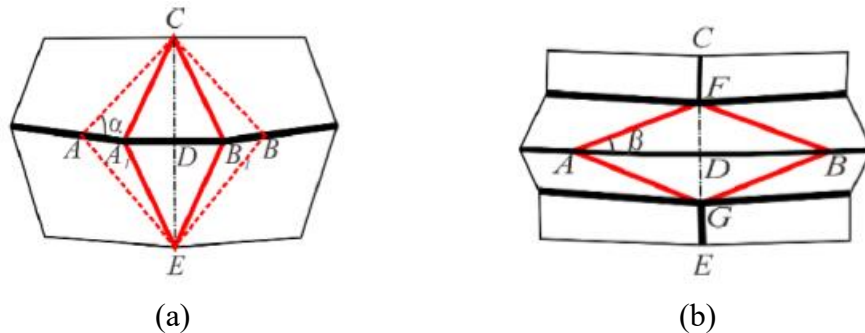


Figure 13 Basic folding element crushing phases: (a) stage I, (b) stage II [3]

2.2.2 Geometry and Parametric analysis

The geometry a crash box can be defined by a minimum of five independent parameters:

- Side length \mathbf{b}
- Pre-folding angle θ
- Sheet height \mathbf{l}
- Number of modules \mathbf{M}
- Number of edges \mathbf{n}

The remaining parameters can be found by mathematical relations since the origami tube is developable from a sheet of metal by only folding it.

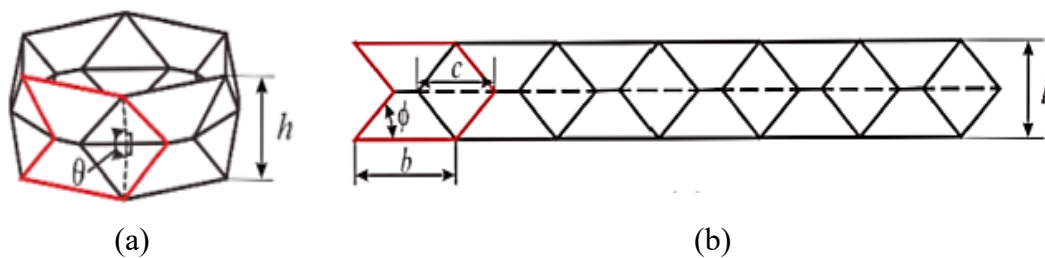


Figure 14 Hexagonal origami module: (a) folded tube, (b) folding lines on sheet [3]

A multi-layered crash box can be built by stacking multiple modules axially with equivalent interfacing cross-section. The layer height and pre-folding angle can be vary from layer to layer, which creates a tube with graded geometric properties. Mathematically complex tapered origami patterns can be also derived, which introduce taper ratio as additional design parameter [8].

An alternative to rhomboidal pattern origami, is represented by the trapezoidal pattern. This geometry modification introduces a new independent parameter \mathbf{c}_2 , transforming the semi-lobe from triangular to trapezoidal. In this case the mathematical bound between \mathbf{c} , \mathbf{h} and θ depends also on \mathbf{c}_1 , broadening the design space [2].

For rhomboidal-lobe origami the new parameter “area ratio” ω , defined as lobe area to total area ratio, is introduced to account the additional geometric degree of freedom.

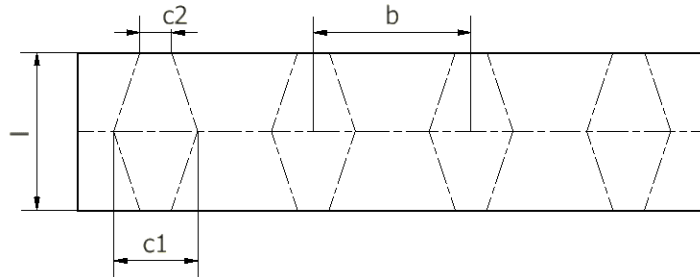


Figure 15 Trapezoidal lobes origami pattern

Prefolding angle

The major parameter affecting the origami performance is the prefolding angle (θ). It represents a compromise between stiffness (which implies higher mean force reaction) and low initial buckling force peak. The maximum prefolding angle is limited by a critical angle value (θ_{crit}) after which the diamond mode is no more correctly triggered [3]. It has to be noted that a prefolding angle of 180° coincides with a straight tube, which is more likely to collapse in symmetric mode rather than diamond mode.

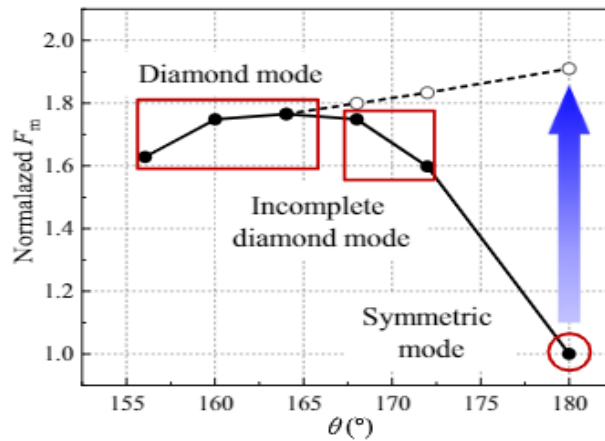


Figure 16 Effects of prefolding angle on mode stability and mean force [37]

In origami with graded prefolding angle, the overall energy absorption has a minor sensitivity on the graded property, with similar performances to uniform model [3]. However, a tapered pattern can be useful to localize and control the initial crushing zone and its evolution during the crushing. For the trapezoid origami, C. Zhou at al. claim that an increased area ratio benefits the mode stability of the origami structure, leading to a higher critical prefolding angle [2].

Number of modules

The number of modules (M) sets the axial wavelength of the buckling mode, as long as the deformation follows the predesigned pattern. In contrast, straight tubes follow their natural collapsing mode with naturally formed folds, which poses a limitation for their energy absorption capacity [38]. Previous studies show that short wavelength and low prefolding are desirable for the trapezoid origami crash boxes in terms of mean crushing force. However, they are detrimental for the diamond mode stability, and for the prefolded pattern to be followed. A higher number of modules leads to a lower critical angle value (θ_{crit}) that, in turn, decreases the energy absorption [7]. The desired performance can be eventually achieved through geometric optimization, according to the needs.

The following plot shows the mean force of origami tube with identical surface area and different number of modules (M). The design points in which the pattern is no more followed are not shown, as it happens for M higher than 4.

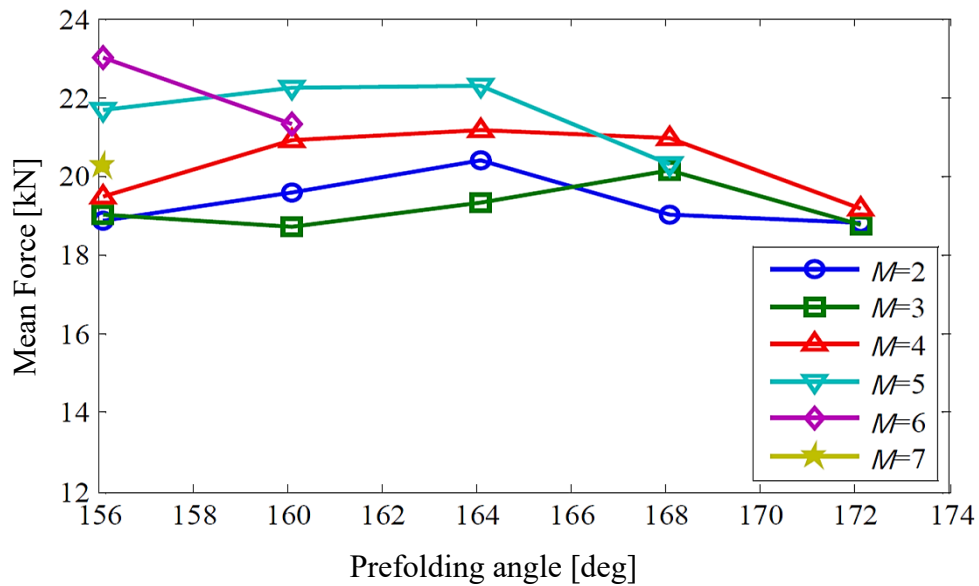


Figure 17 Influence of number of modules on mean force [7]

Wall thickness

The influence of wall thickness can be estimated analytically according to the Jiayao Ma et al. [7] theoretical approach previously introduced, which proposes a formulation for the non-dimensional parameter t/b influence on mean force. According to the analytical model, a higher t/b ratio benefits the ratio between mean force of diamond mode and mean force of symmetric mode. Hence, leading to a more substantial gain in using an origami patterned tube rather than a straight square tube.

$$\frac{F_{Mean\ Diamond\ mode}}{F_{Mean\ Symmetric\ mode}} = 0.94 + \frac{4.9}{\sqrt{\frac{t}{b}}} \quad (4)$$

Cross section

As already discussed in section 2.1.1, SEA of a circular tube is higher than a square tube. However, circular tubes are associated with a high initial buckling force. Therefore, polygonal tubes, are frequently used as a trade-off between square tubes and circular tubes [24].

Caihua et al. introduced the trapezoidal lobe pattern as an intermediate configuration between squared and octagonal tubes. Its parametric FE analysis shows that a high area ratio (ω), defined as total tube area divided lobe area, can benefit the mode stability [2].

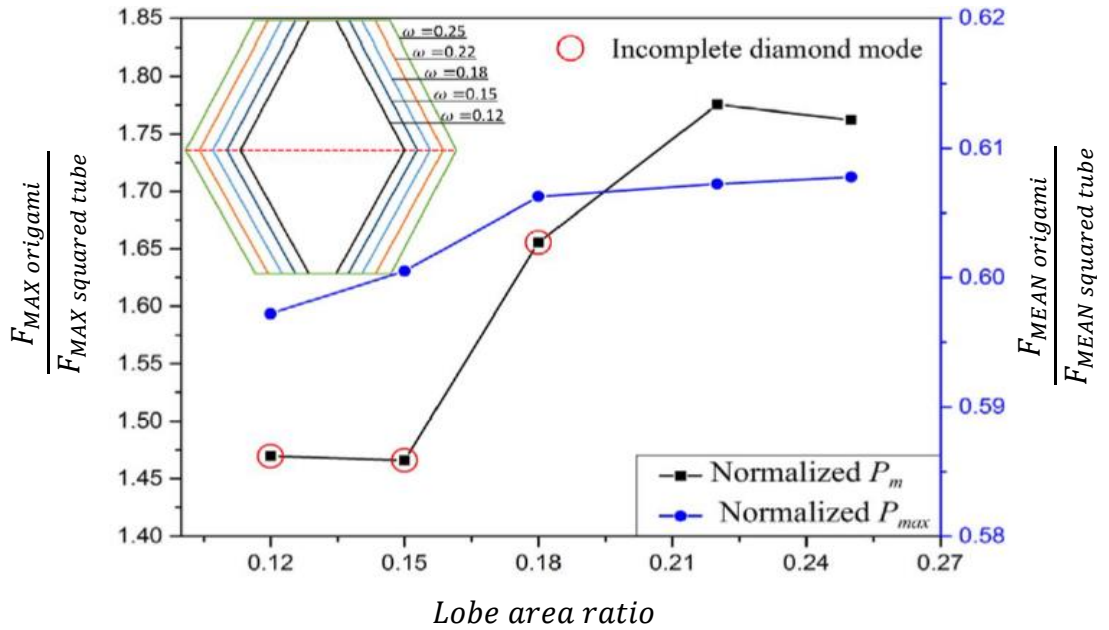


Figure 18 Area ratio influence on origami force output and stability [2]

2.2.3 Manufacturing method

The pattern can be conveniently manufactured by joining two half tubes which are stamped from metal sheets. The origami pattern is developable from a sheet theoretically without in-plane stretching, hence only limited deformation is employed for the production process [7].

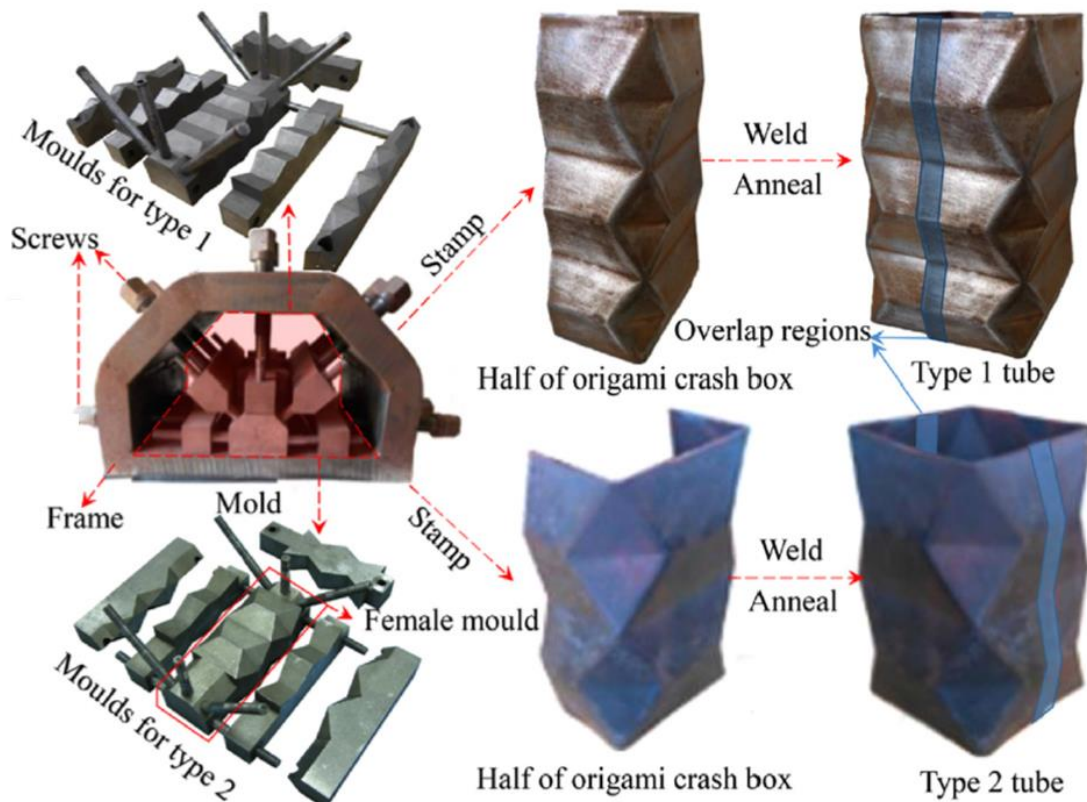


Figure 19 Example origami tube manufacturing process [5] [6]

The joint can be realized through riveting or continuous/spot welding, and it might require a material overlap in the bounding region. An example of a basic mould used by the Dalian university for their experimental campaign is reported in Figure 19 [5] [6]. In their case the joint is realized by spot welding an overlapped area at the edges.

This process is suitable for large scale production, since the production steps are identical to the ones employed for the manufacturing conventional shaped tubes. Therefore, the production cost for the origami tube is also comparable with conventional energy-absorbing tubes with pre-manufactured geometric imperfection, commonly used for crashworthiness applications. Casting and hydroforming can also be considered as possible alternatives to the process described above.

3D printed origami tubes

Yang et al. [39] employed Additive Manufacturing for producing brass origami tubes in a small batch. They also correlated experiments with FEM analysis. The author addresses the discrepancy between numerical and experimental data to the significant variation in wall thickness and pattern geometry due to the poor tolerance of the 3D printing process, and additionally, to the poor predictability of physical and mechanical properties of the printed material. Furthermore, the small number of specimens does not ensure the experiment repeatability (44.5% difference in mean force for two experiments with the same nominal geometry). A minor fracture is observed in the experiment, in the proximity of a folding line.



Figure 20 Crushing of origami patterned 3D printed brass tube [39]

End-origami Pattern

A new origami pattern, called end-origami, is claimed to represent a competitive alternative to the conventional origami for its ease in manufacturing [37]. The configuration can trigger the diamond buckling mode without the conventional prefolded rhomboid lobe at the edges. The lobe is instead developed during the crushing process as shown in the DIC capture in Figure 21.b, thanks to a mode inducer conveniently manufactured by folding the tube ends. Experimental quasi-static tests show excellent results, achieving CFE and SEA respectively 79% and 85% higher than the equivalent straight squared tube.

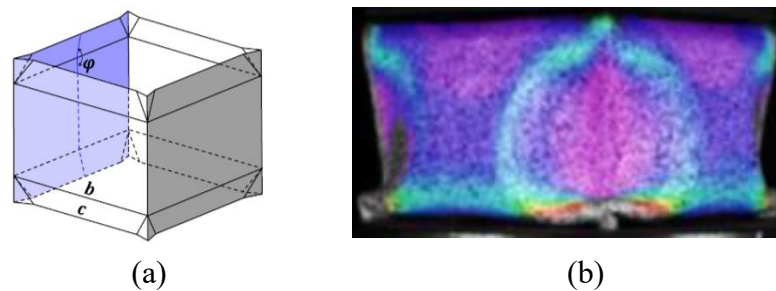


Figure 21 End-origami: (a) origami pattern, (b) lobe developing during crushing

2.2.4 Diamond mode stability

Buckling mode stability refers to the occurrence of the pure global diamond mode without any other global or local buckling mode interference. Under certain conditions other global modes can appear, such as Eulerian bending or symmetric/asymmetric. This situation is referred to as mixed mode. Additionally, stress concentration points can trigger local buckling phenomena which also affect the energy absorption performances.

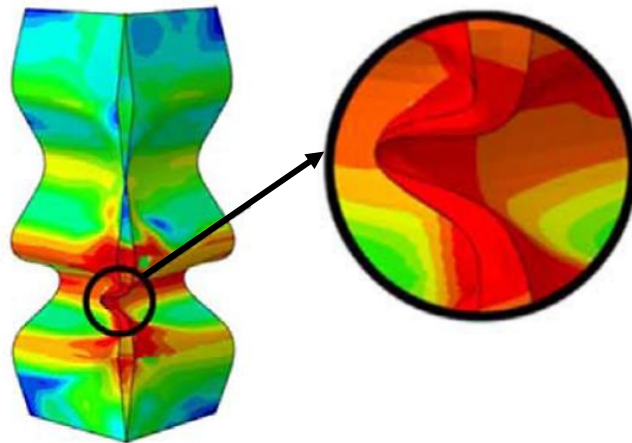


Figure 22 Local buckling in lobe intersection (quarter of tube FE model) [2]

As previously described in Chapter 2.2.2, it is possible to verify through experiments the existence of a critical prefolding angle (θ_{crit}), under which the geometric predesigned pattern is correctly followed throughout the crushing stroke. However, diamond mode stability is sensitive to oblique load [10], manufacture imperfections [9] and inertia effects [6] which are unavoidable in a real application scenario. These effects can trigger local buckling in lobe intersections for prefolding angles lower than θ_{crit} . Different methods are proposed for solving the issue, such as tapered origami, bulkhead cross-section reinforcement and trapezoidal lobes.

Caihua Zhou et al. introduced a noteworthy way to recognize the emergence of undesired modes by visual inspection. As shown in Figure 23, the cross-sectional shape becomes irregular under the influence of local or symmetric buckling mode. The ratio between post crushed diagonal and undeformed diagonal is proposed for distinguishing complete diamond mode, transition mode and symmetric mode from each other [9].

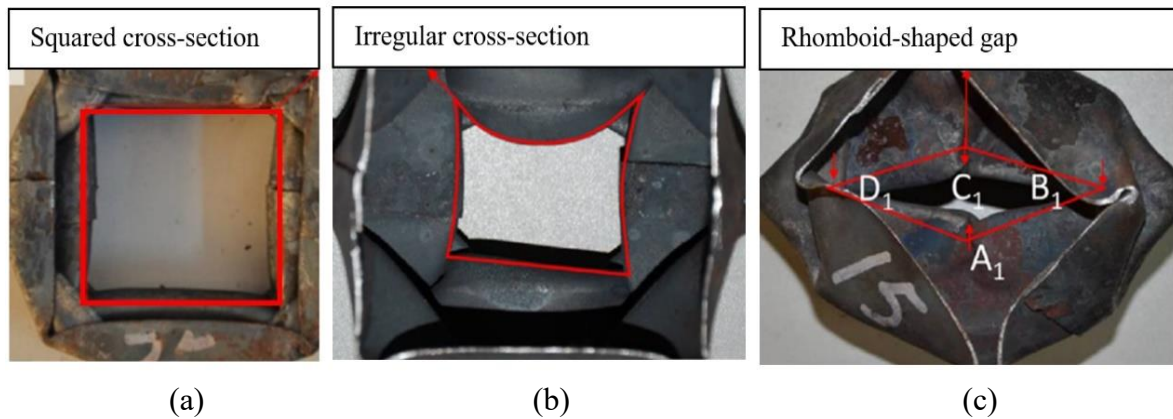


Figure 23 Crushed cross-sections modes: (a) diamond, (b) local, (c) symmetric [6]

During experimental tests, several specimens manifested local buckling at the modules interface. In a few cases the global symmetric mode is yet initialized. In that case, buckling occurs at the beginning of the compression in the slender section that connects two modules (A_1, B_1, C_1, D_1 points in Fig. 23). Such instability triggers buckling at the adjacent vertices at the centre of the module. In the end 10 buckling points are formed in a tube which collapses in symmetric buckling, generating only four folding elements (half of diamond mode) [6]. The main effects known to be responsible of triggering undesired modes are listed below.

Oblique loading

Energy absorbers are rarely subjected to pure axial loading in a real application and therefore the study of structural crashworthiness under oblique loading is essential. In a similar way to the critical prefolding angle, a critical load inclination angle ($\alpha_{stability}$) was reported for straight and patterned tubes to indicate the transition from progressive axial crushing to global bending collapse. A consequent drop in energy absorption is observed when the load angle, is larger than the critical value. [10]

The analysis of C. Zhou at al. points out a critical problem of this novel configuration. The relatively slender origami tube tested shows a mixed diamond (Eulerian Bending Mode (EBM) and Diamond mode) for a minimal load angle (starting from around 2°). The origami tube also collapses in complete EBM for lower load angles when compared to a straight tube, therefore the advantages of the origami can be less evident under oblique load.

A broad bibliography is available for thin-walled structures subjected to oblique load. A simple and effective solution comes from tapered origami tubes. Taper tubes are widely employed as energy absorption devices thanks to their high energy absorption efficiency when subjected to oblique loads, compared with that of straight tubes [33]. Studies on tapered origami tubes reveal that SEA is slightly influenced by taper ratio for axial crushing, as long as the diamond mode is triggered. [8]

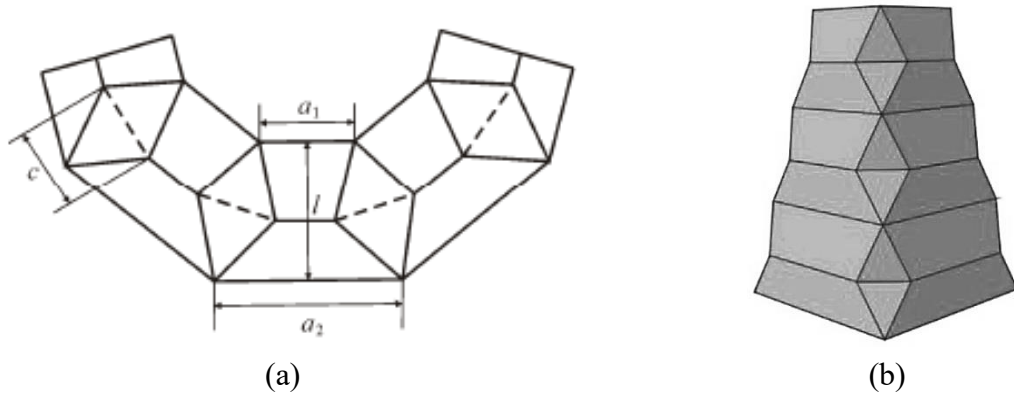


Figure 24 Tapered origami tube: (a) 2D folding lines on metal sheet, (b) folded tube [7]

Manufacture imperfection sensitivity

Induced imperfections are a common tool in crashworthiness design to reduce the initial force required to initiate the buckling until the desired value. The origami pattern intrinsically works as geometrical imperfection by concentrating stress at the edge folds. Wang and Zhou study [9] individuated a specific type of unwanted manufacturing imperfections capable to induce symmetric mode in the origami-patterned tube. They found a correlation between the cross-section distortion during manufacturing and symmetric buckling occurrence in the resulting crushing.

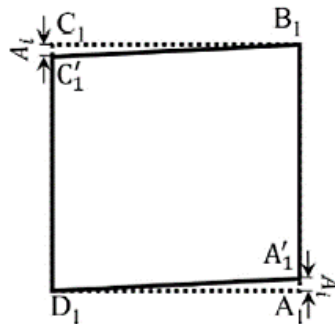


Figure 25 Manufacturing imperfection capable to trigger symmetric mode [9]

Dynamic effects

In the real world, axial crushing of energy absorption tubes occurs dynamically since they are always subjected to impact loading. Independent dynamic effects coming from structure's inertia and material's strain rate sensitivity substantially complicate the analysis.

In low velocity impacts (up to tens of meters per hour) the inertia effects which tend to preserve the unbuckled shape of a tube, are not strong enough to change the way the tube buckles [7]. Under these conditions the inertia effects within the device are considered unimportant and hence the kinetic energy is converted into plastic work in a quasi-static deformation mode [13]. On the other hand, under high velocity impacts the inertia forces plays an important role which transform the progressive buckling into dynamic buckling.

Material strain rate effects are significant for strain-rate-sensitive materials and thus they should be taken into account. Initial yield stress and overall plastic curve of a material experience a strengthening effect which often result in a greater energy absorption of the tube under dynamic load [22]. Strain rate effects are commonly numerically modelled in FE analysis by turning a static material flow stress model into a dynamic one, by introducing strain rate dependent material models, such as the Cowper-Symonds model reported below.

$$\sigma = [\sigma_{yield} + K \varepsilon_{pl}^n] \left[1 + \left(\frac{\dot{\varepsilon}}{D} \right)^{\frac{1}{q}} \right] \quad (5)$$

Where strength coefficient (K) and strain hardening exponent (n) coefficients are associated with the strain hardening model, while strain rate hardening coefficient (D) and strain rate hardening exponent (q) model the strain rate sensitivity. This particular material model is employed in previous publications about numerical simulations about dynamic crushing of thin-walled structures [10] [35]. The strain rate hardening model increases the yield stress as the strain rate increases, resulting in an offset of the plastic stress-strain curve to higher values. Since it represents a local phenomenon, the problem is subjected to a higher degree of complexity.

The strong influence of the strain rate hardening for mild steel energy absorbers can be observed by comparing quasi-static and dynamic experiment carried out on the same geometry by C. Zhou and B. Wang [6] [5]. In the dynamic case, the mean and maximum force reactions are around twice the ones in static case.

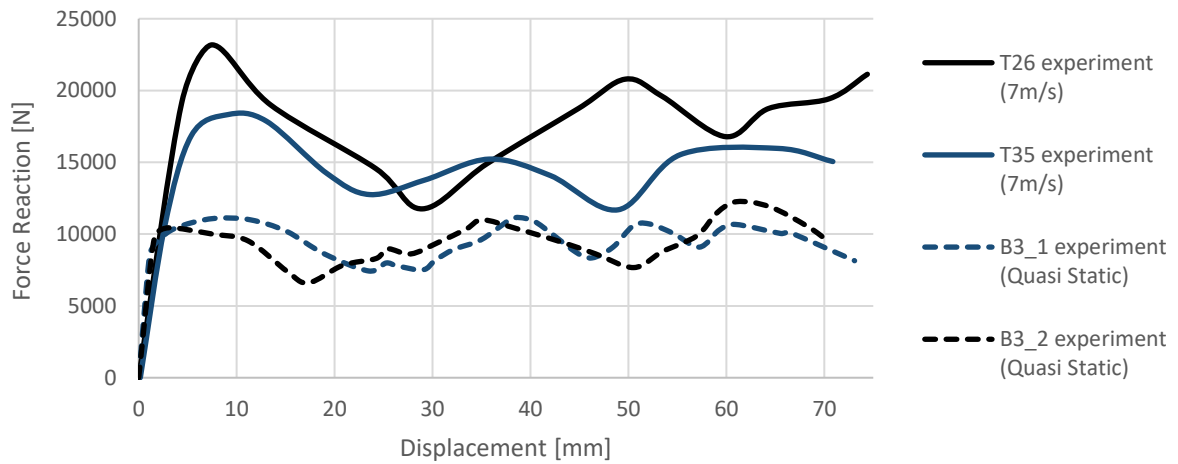


Figure 26 Crushing force trend in quasi-static [5] and dynamic case [6]

For the origami tube, it is found an increased sensitivity to geometric imperfection under dynamic load if compared to a quasi-static crushing [6]. Comparative experiments show that while in quasi-static case the correct mode is correctly achieved [5], in dynamic case only few specimens properly trigger diamond mode, while the vast majority shows several local buckling points or even symmetric mode.

A bulkhead between two modules, as shown in figure 27, is found to be helpful in preventing local buckling by stiffening the edge region, which is known to be the most sensitive point to geometrical imperfections and oblique load. Nevertheless, the introduction of a plate between modules implies more weight and manufacturing complexity. The solution is studied for reducing both imperfection and oblique load mode sensitivity, and it shows good performances in FEM analysis [9] [10].

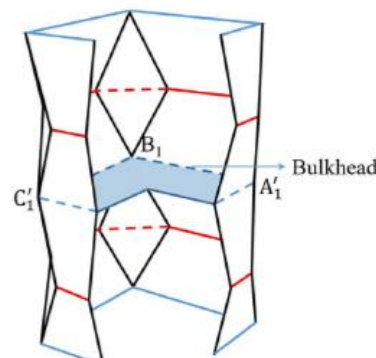


Figure 27 Bulkhead stiffener [9]

3. EXPERIMENT ON SLM MANUFACTURED SPECIMEN

3.1 Test aim and objectives

Experimental tests are fundamental for validating the FEM explicit model employed for the optimization procedure. Therefore, it is crucial to find a manufacturing process that allowed to test the outcomes of the optimization and explore different designs in a convenient and reliable way. For this purpose, selective laser melting (SLM) is selected as manufacturing process. The employment of metal 3D printing technology allows to produce a small number of complex specimens with different geometries, involving lower cost and time compared to the traditional stamping and welding procedure, which is instead preferable for mass production thanks to its scalability.

The present investigation aims to assess the prospect of manufacturing energy-absorbing origami tubes through the additive processes. The experimental outcomes are evaluated in terms of triggered collapsing mode, performances, and predictability of the behaviour through numerical analysis.

With this experimental test it is intended to derive the reference case, and thus the starting point, for the following geometrical optimization of the pattern for a future application in PAV crash-worthiness design. The desired outcome should not show fractures, mixed buckling mode and it needs to be eventually modelled through finite element analysis. If such a behaviour is achieved, additive manufacturing would result in a cost-effective approach for the optimization study, where a small number of specimens with different geometries are needed, in order to perform experimental tests and try different solutions.

It is important to note that the experiment does not aim to demonstrate the improvement of the origami configuration compared to the equivalent straight tube, since a broad bibliography is already available about this topic, as discussed in the previous section [28] [2].

3.2 Specimens characteristics

3.2.1 Geometry

The reference geometry is recognized to successfully trigger a complete diamond mode in the tube stamped from a mild steel sheet.

The surface geometry is realized on the commercial CAD software Inventor by Autodesk and exported in STL to the manufacturer. The STL format describes the CAD model through decomposition and approximation of its geometry with a combination of triangular elements, thus removing any construction and modelling history data.

The nominal dimensions of the CAD surface model are summarized in the following figure, while wall-thickness and edge rounding are discussed in the following sections.

b	ϑ	h	M	c
60 mm	156°	117.38 mm	3	20 mm

Table 1 Specimen dimensions

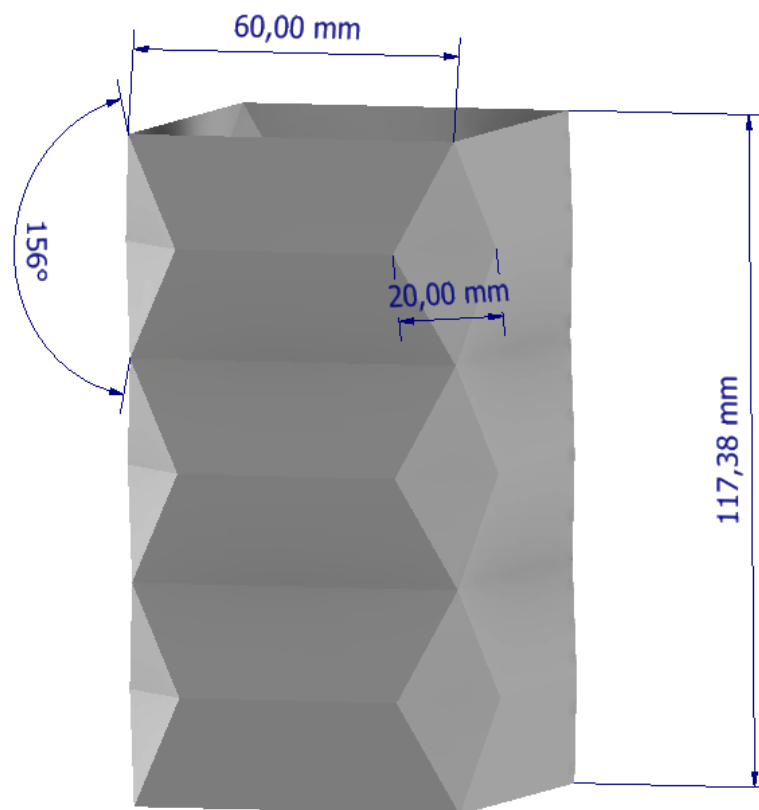


Figure 28 Nominal surface geometry

3.2.2 Manufacturing process

Different approaches were considered to produce the origami specimens. Finally, additive manufacturing (AM) is selected as manufacturing method. Metal AM guarantees the possibility of producing small batches of samples with a high geometrical complexity to size ratio with advantages in terms of cost and production time, compared to a traditional manufacturing process [40], such as stamping and welding. The tubes were realized through selective laser melting (SLM) from a local company outside the university with the printer EOS M290 (Build size: 250x250x320mm). All specimens underwent a stress relief heat treatment after being printed.

SLM is a rapid prototyping technique designed to use a high power-density laser to melt and fuse metallic powders together. This powder bed based layer-by-layer additive procedure is capable to build metal parts that approach a density of 100%. In order to reach such a high density, the metallic powder particles are locally molten, which results in high thermal gradients and residual stress in the material. Residual stress, in turn, can cause distortion of the geometry and trigger cracks or delamination in the material. Furthermore, the layer-by-layer process induce an anisotropy in material properties, dependant on its build direction.

Hence, parts produced by metal AM have mechanical properties that can substantially differ from wrought or cast metals, which is proven to be one of the biggest limits that prevented the widespread adoption of this technology [41].

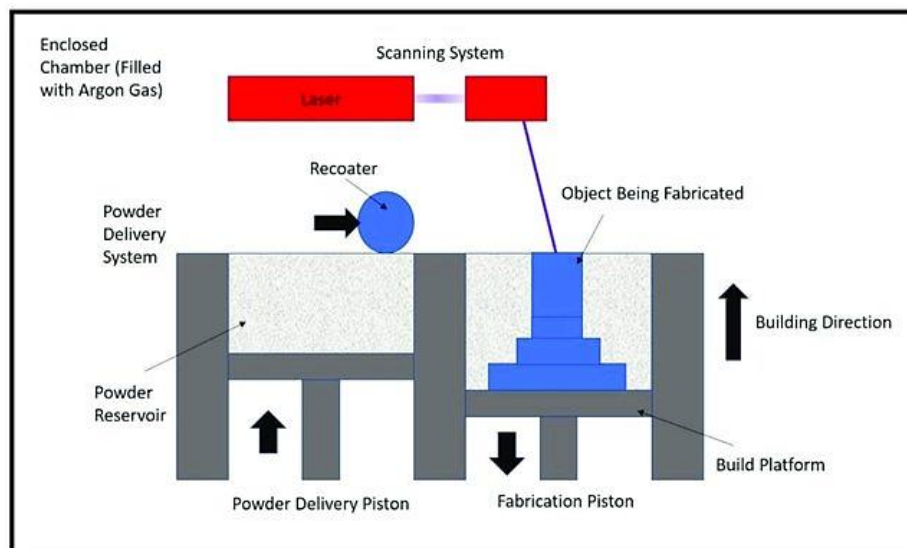


Figure 29 Schematic illustration of powder bed SLM process [42]

The build direction is coincident with the tube vertical axis, in order to avoid an extensive use of supports which are necessary to hold the tube wall while printing and dissipate the heat locally generated by the laser beam.

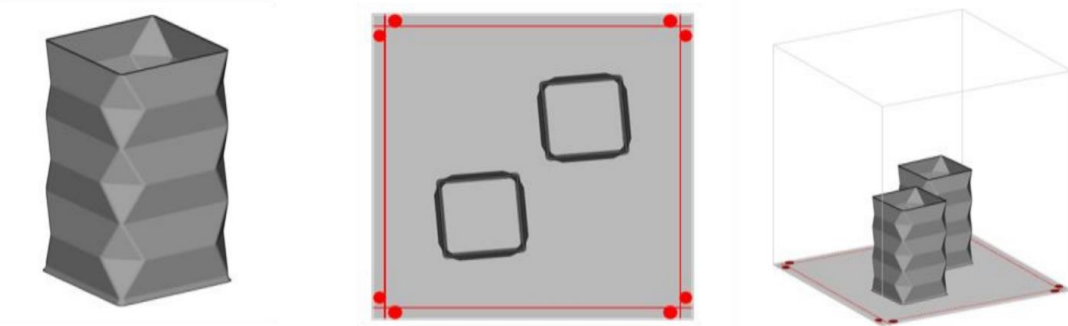


Figure 30 Printing configuration

The tube dimensions are measured before performing the test, due to concerns about the strong correlation between buckling mode instabilities and initial geometrical imperfections.

No major geometric imperfections are found in the specimens, although a very high rugosity is introduced by the layer-by-layer additive process.

A minor difference from the reference CAD geometry is observed in external and internal crests as represented in the figure below. The edges are found to be slightly rounded on the plane perpendicular to the built direction. The radius is approximated from a three-points measure (the scale of defect in the picture below is magnified in order to better display it).

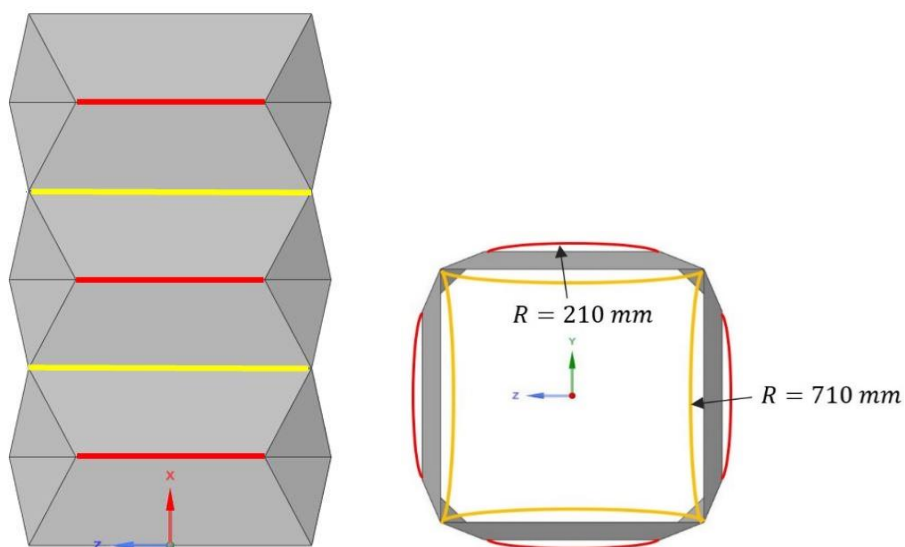


Figure 31 Edge rounding in the 3D printed origami tube

This defect can be due to thermal stresses during the additive process; however, the radius does not affect the symmetry of the problem, because it is measured to be almost identical on the four edges and on the three modules. This slightly rounded shape is represented and analysed with FEM and no observable difference are found in force trend, mean and maximum force.

The cross-section distortion is included in the measurement, since it is recognised to be an important indicator of mode instability [9], as already discussed in the previous chapter. The imperfection is accounted by the ratio between the two diagonals of the squared cross-section, which is always found to be close to 100%, which should not affect the correct mode induction.

The total mass of each specimen is evaluated. The mass is an important quality indicator in additive manufacturing, a high variation between specimens can indicate density variations, porosity and in general a poor quality of the samples. The few specimens available show a minor difference in total mass from each other.

The maximum difference in tube height, measured on the four edges of the tube is controlled for ensuring a perfectly axial loading. The axial direction coincides with the build direction; therefore, a good tolerance is always observed.

Due to the elevate surface roughness of the SLM printed part, the determination of the effective thickness is a challenging operation. All specimens are measured with a micrometre with flat hands. The wall thickness is found to be slightly higher around the lobes, the value of deviation is indicated together with the averaged value.

The measured values are summarized below:

<i>Specimen material</i>	<i>AlSi10Mg</i>		<i>SUS316</i>			
	<i>A1_t1.5</i>	<i>A2_t1.5</i>	<i>S1_t1.5</i>	<i>S2_t1.5</i>	<i>S3_t1</i>	<i>S4_t1</i>
<i>Specimen name</i>				Annealed		
<i>Diagonal ratio [%]</i>	99.5	99.7	99.6	99.7	99.8	99.7
Δh_{MAX} <i>tube [mm]</i>	0.1	0.1	0.1	0.2	0.1	0.1
<i>Mass [g]</i>	111.81	112.35	344.46	344.34	224.54	224.87
<i>Thickness [mm]</i>	1.56	1.56	1.58	1.58	1.04	1.02
	± 0.02	± 0.02	± 0.02	± 0.02	± 0.02	± 0.02

Table 2 Measured specimens characteristics

Lastly, the 3D printed tube has a bevel in the slender edge region of the lobes. This feature has been proved through FEM analysis not to have influence on the tube behaviour and output performances.

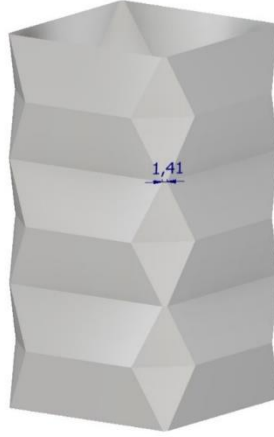


Figure 32 Lobe intersection bevel

For all samples, the final geometry exhibits excellent geometrical tolerances in comparison with the stamped geometry showed in literature [6]. Furthermore, the current specimens are stamped as one solid part, avoiding non-homogeneous regions resulting from welding lines or material overlaps.

3.2.3 Materials

Two high performance materials are chosen for the case study: SUS316L stainless steel (equivalent to SAE 316L) and AlSi10Mg aluminium alloy. The mechanical properties are found through the tensile test data sheets provided by the manufacturer.

For both materials, several Force-Displacement curves are available. True stress and true strain are found from the engineering stress and strain through the approximated formulas below:

$$\varepsilon_{eng} = \frac{\delta_{displacement}}{l_{gauge}} \rightarrow \varepsilon_{true} = \ln(1 + \varepsilon_{eng}) \quad (6)$$

$$\vartheta_{eng} = \frac{F_{measured}}{A_{cross-section}} \rightarrow \vartheta_{true} = \vartheta_{eng}(1 + \varepsilon_{eng}) \quad (7)$$

The “Plastic strain” formulation used for modelling material properties in the FEM solver refers to the total strain reduced by the elastic strain [43].

$$\varepsilon_{pl} = \varepsilon - \frac{\sigma(\varepsilon)}{E} \quad (8)$$

The material stress-strain curves in plastic regime are modelled through the Ludwik equation [44] for the successive FEM analysis.

$$\sigma = \sigma_{yield} + K\varepsilon_{pl}^n \quad (9)$$

Where the strain hardening exponent (**n**) and strength coefficient (**K**) are found by applying a first order regression method to the bi-logarithmic stress to plastic strain curve [45]. MATLAB is used for this numerical calculation.

$$\ln(\sigma - \sigma_{yield}) = n \ln \varepsilon_{pl} + \ln K \quad (10)$$

The resultant stress to plastic strain curves are shown in the next sections, a good agreement is found between the tensile test output and the employed strain hardening material model.

The analytical Ludwik material model is employed in order to make the model strain rate sensitive in a future investigation without changing the plastic strain hardening curve. In fact, the Ludwik model is employed for representing the Cowper-Symonds strain rate model implemented in ANSYS Autodyn [43].

$$\sigma = [\sigma_{yield} + K\varepsilon_{pl}^n] \left[1 + \left(\frac{\dot{\varepsilon}}{D} \right)^{\frac{1}{q}} \right] \quad (11)$$

SUS316L stainless steel

Five tensile tests data for each printing direction (parallel and perpendicular to load application) are provided from the manufacturer for the 3D printed SUS316L material. Mean value and standard deviation of tensile output properties are computed for each printing direction. Major variations are only found in the elastic Young Modulus.

<i>Direction respect to build direction</i>		E [GPa]	σ_{Yield} [MPa]	<i>Elongation</i> [%]	ϑ_{UTSeng} [MPa]
<i>Parallel</i> <i>(Nr. 5)</i>	Average	199	431	48.9	647
	St. Deviation	13.1	2.8	0.49	1.90
<i>Perpendicular</i> <i>(Nr. 5)</i>	Average	209	410	57.8	604
	St. Deviation	60	7.2	0.75	1.35
<i>Averaged properties for the isotropic material model</i>		204	420.5	53.3	625.7

Table 3 Additive manufactured SUS316L mechanical properties

The tested rounded specimens have a diameter of 6.25 mm, with 20 mm gauge length and 36 mm overall length. The engineering Stress-Strain curves are extrapolated from the tensile test Force-Displacement data for two specimens, which are chosen to be the most representative of the averaged mechanical properties in parallel and perpendicular direction respectively. Their trend is used to derive the strain hardening coefficients

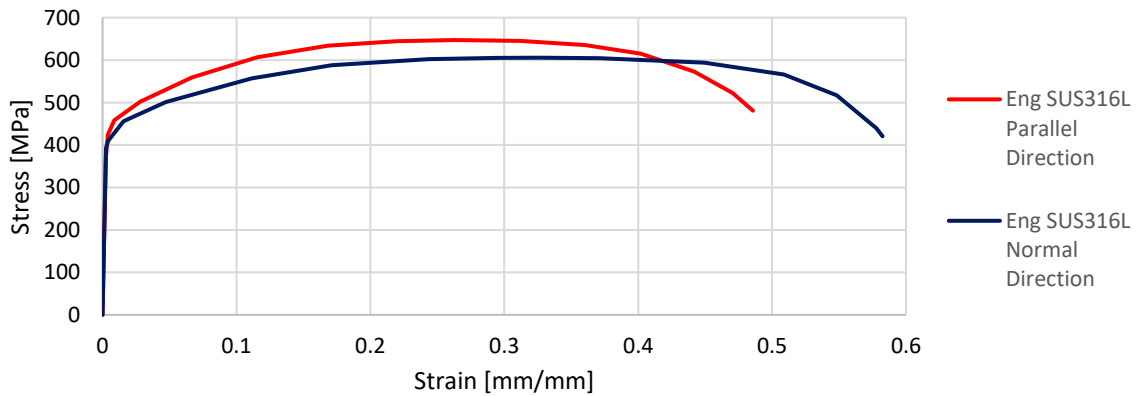


Figure 33 Stress strain 3D printed origami along two printing directions

The 3D printed material is known to be orthotropic. However, tensile tests show a minor difference between specimens printed in a parallel and normal direction respect to the tensile load. Therefore, an isotropic material model is employed for modelling elastic and plastic behaviour in the following FEM analysis. Averaged values of Young’s modulus and yield strength calculated from all the available data, and the plastic curve shown below are used for this purpose. The curve in figure 34 has no elastic slope since it represents the “plastic strain”.

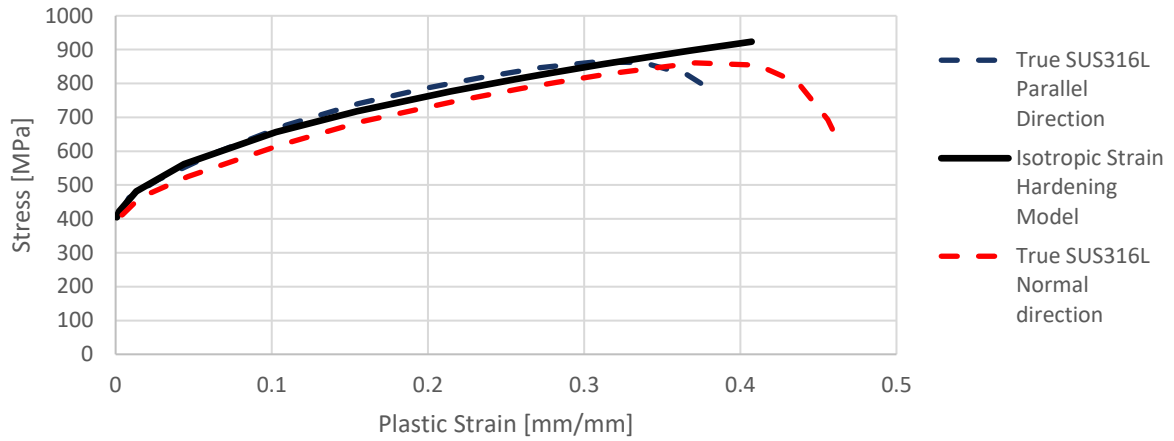


Figure 34 Modelled isotropic strain hardening SUS316L material

Density is assumed to be 7900 kg/m³ from EOS datasheet, since production process information are not available [46].

No data are provided about the behaviour of the material under compressive load.

AlSi10Mg aluminium

The Stress-Strain curves extrapolated from the tensile Force-Displacement output are shown in the next plot. Tensile and compressive tests are provided by the manufacturer for modelling the material numerically. The material properties are found to be reasonably similar in both the characteristic directions, therefore the material is modelled as isotropic in the following FEM analysis.

<i>Averaged properties</i>	<i>E</i> [GPa]	σ_{Yield} [MPa]	<i>Elongation</i> [%]	$\vartheta_{UTS_{eng}}$ [MPa]
<i>Tensile</i>	68.7	227	3.8	280.7
<i>Compressive</i>	73.6	252		

Table 4 Additive manufactured AlSi10Mg mechanical properties

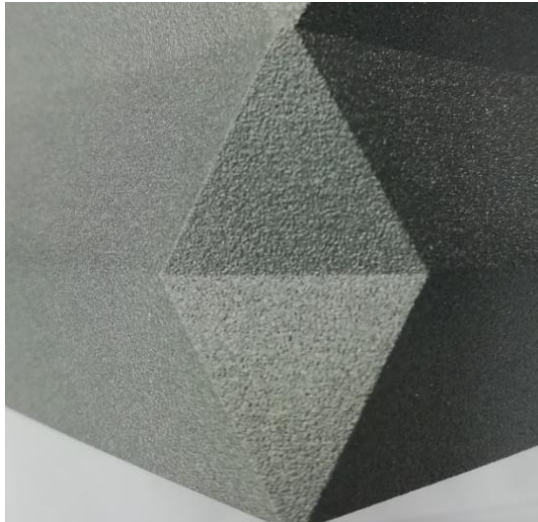
The investigation follows the ASTM E8/E8M-16a standard for tensile tests (rounded specimens ϕ 4.75 mm and 25.4 mm gauge length) and the ASTM E9-19 for compression test (rounded specimens ϕ 15 mm and 41 mm total length). Only an overview of AlSi10Mg mechanical properties is given due to confidentiality reasons.

In the same manner as SUS316L, both tensile and compressive tests show a minor difference between specimens printed in parallel and perpendicular direction. However, averaged values of Yield stress and Young's modulus are found respectively 11% and 7% higher in the compressive test. The engineering Stress-Strain curves are extrapolated from a representative tensile test, which is chosen to be the most representative of the averaged mechanical properties. Strain hardening coefficients are derived from that curve.

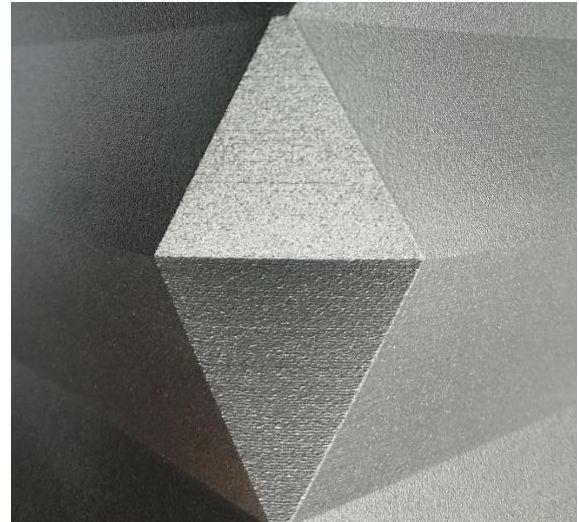
The material density is assumed to be 2670 kg/m³ from EOS datasheet since production process information are not available [47].

AlSi10Mg fabricated by AM technology is found to have a considerable strain rate hardening under dynamic loading [48], in contrast to isotropic aluminium alloys which are considered almost strain rate insensitive [49].

Through visual inspection is possible to notice that the aluminium tube shows a rougher surface than the stainless-steel tube. Previous studies have pointed out that SLM processing of aluminium alloys is much more difficult than titanium alloys, nickel alloys or steels. This can be attributed to the physical properties of the aluminium powder characterised by low absorptivity to the laser beam and the high heat conductivity [50].



(a)



(b)

Figure 35 Specimens surface roughness: (a) AlSi10Mg, (b) SUS316L

3.3 Quasi Static test settings

The present investigation aims to obtain a reference case with neglectable influence of strain rate hardening and strain rate effects, in order to have a better understanding of the complex crushing phenomenon.

The ASTM E9-19 standard (Standard Test Methods of Compression Testing of Metallic Materials at Room Temperature) is followed for the procedural indications. Thus, a strain rate of 0.005 [1/min] is chosen as representative of quasi-static condition. The test is performed in displacement control throughout the crushing stroke.

For the experiment, a crosshead speed of 0.6 mm/min is chosen to have approximately the strain rate recommended by the ASTM E9-19 chapter 8.6. The formula below is used to estimate the strain rate in a 1D case tensile test.

$$\dot{\varepsilon} = \frac{\Delta l}{\Delta t l} = \frac{v}{l} \quad (12)$$

The approximation does not account strain rate concentration at the folding edges and the rigid deformation of the tube while crushing. The actual strain rate in the tube with the approximate crushing speed is analysed through 3D DIC technique and it is found to have a maximum value around 0.000125 [1/s], thus representative of the quasi-static condition.

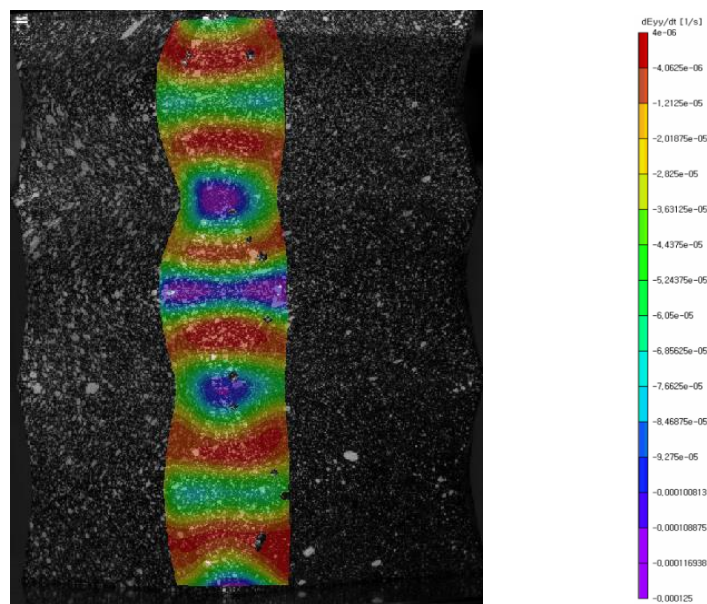


Figure 36 Strain rate field from DIC data

The Instron UTM has upper loading limited to 120 kN, due to the load cell maximum force of 150 kN, which is suitable for this analysis. Prior FEM analysis gave a first force evaluation, which was used to choose an adequate UTM machine.

The tube stands on a thick plate while the crosshead connected to the load cell moves downward to compress the tube. Both ends of the tube are free of constraints. The tube free edges and the UTM rigid plates were previously cleaned and measured to be horizontal (ASTM E9-19 chapter 8.2). In addition, the whole 2 hours 16 minutes long crushing was monitored and recorded with two cameras, while the load was sampled by the load cell with rate of 0.1 points per second.

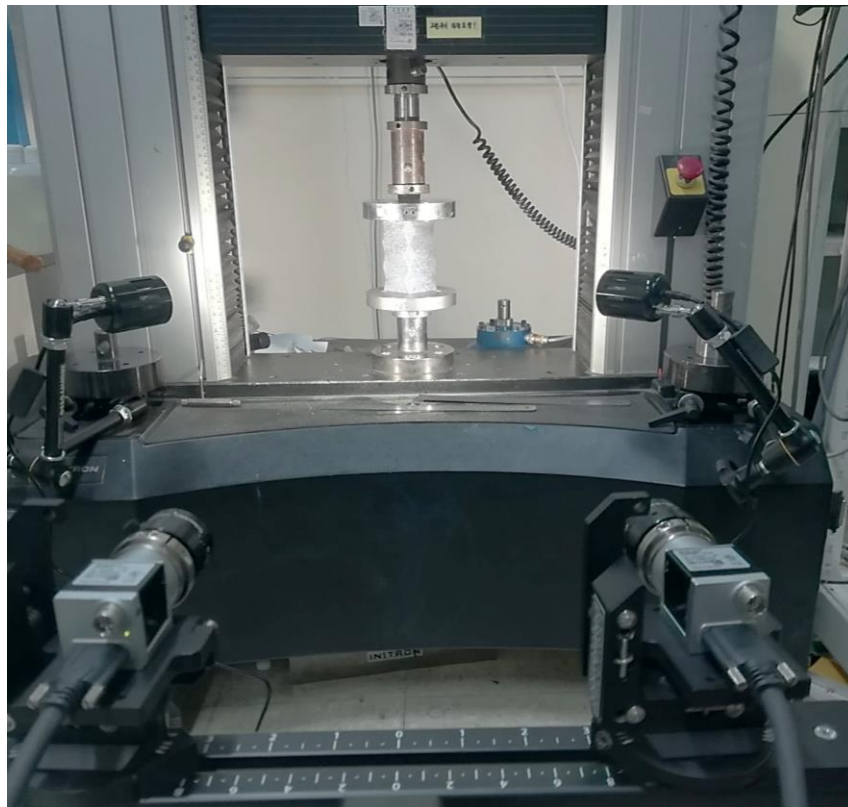


Figure 37 Experimental setup

Strain and displacement fields are computed using a Digital Image Correlation (DIC) on a series of sequential pictures of the tube during the crushing process. The images are taken by two digital cameras (Basler ace acA2440-75um) at a rate 0.033 frames per second, according to the large timespan of the process. The DIC analysis is based on a 2D surface recognition, using a QUAD element formulation which creates virtual extensometers between the mesh nodes [51]. The tube surface is previously painted black and sprayed with an adequate white speckle pattern. The origami lobes represent the area of interest of this DIC study; therefore, a good resolution and low noise is required in that zone.

The commercial software “VIC-Snap9” by Correlated Solutions is utilized for image acquisition and calibration. A low level of noise in the area of interest is achieved by adjusting camera’s aperture, exposition time and focus with a proper position of lights and cameras. The presence of sharp edges and surfaces laying on different angled plans makes the calibration process quite challenging.

A calibration phase is needed before capturing tube images. A 10 mm calibration dotted plate was imaged in different angles simultaneously by both cameras.

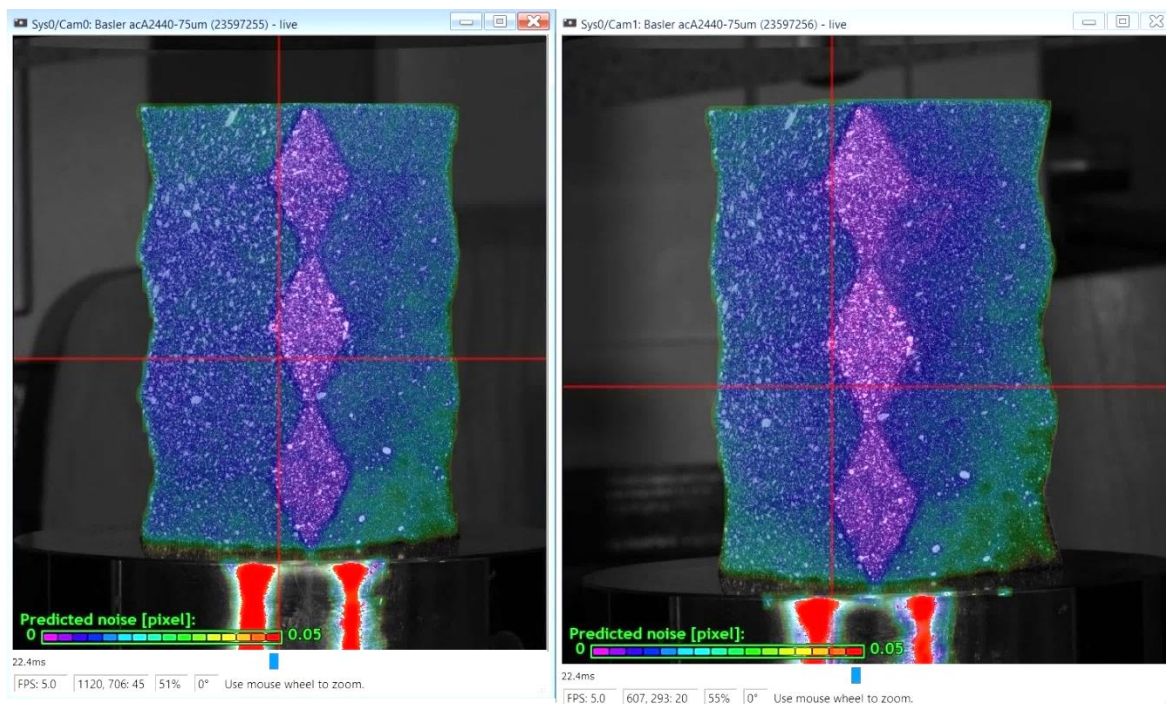


Figure 38 Predicted noise level in DIC analysis

The post-processing of the resulting images is computed with the software “VIC-3D” by Correlated Solutions. The DIC correlation computes in output a two-components vector (in-plane components) of coordinates, directional displacements and their derivatives, directional and principal strains and their derivatives.

3.4 Numerical analysis

For the present numerical analysis, the explicit solver AUTODYN, part of ANSYS Workbench 2021R1 is employed. The geometry is modelled with the CAD software Inventor 2019 by Autodesk (Student licence) and later imported in ANSYS Workbench. Meshing, Pre-processing and Post-processing are performed in ANSYS Workbench environment, while the explicit solver AUTODYN is chosen thanks to the standard licence available at the Smart Structures and Hardware Systems laboratory. Widely employed alternative explicit solvers are also LS-DYNA by Livermore Software and ABAQUS Explicit by Dassault Systems. Excel and MATLAB are employed for data post-processing.

Previous numerical investigations regarding quasi-static buckling of origami or straight tubes made use of explicit FE codes due to the large deformations and complex contacts experienced during crushing. Furthermore, the quasi-static explicit model employed can be conveniently converted in a dynamic model for future studies.

3.4.1 Explicit FEM

Explicit solvers are widely used in automotive and aerospace field, for manufacturing problems, crashworthiness design or impact analysis thanks to the capability of dealing with highly nonlinearities and dynamic problems. The nonlinearity can come from boundary conditions (in particular complex contacts), geometric large deformation (typical of thin structure with low strain and large rotations), material nonlinearity, material failures or dynamic effects involving inertia forces [52].

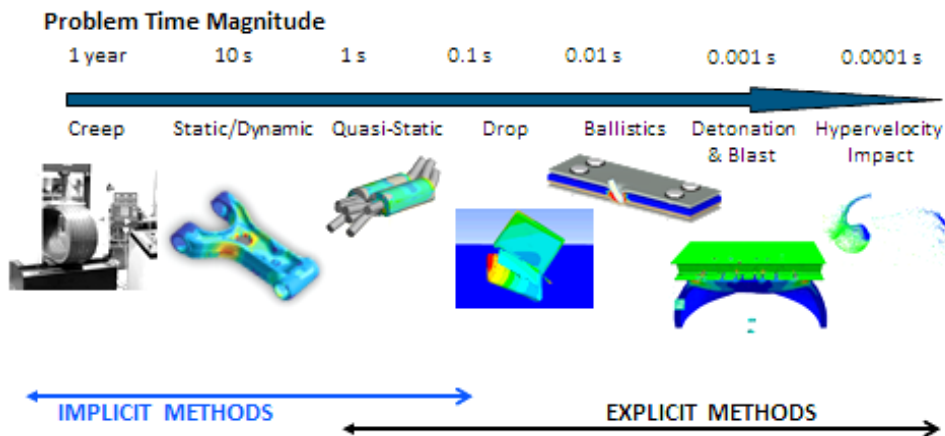


Figure 39 Explicit and Implicit FEM applications [43]

In the same way of implicit analysis, the problem formulation is expressed through partial differential equations (PDE) to be solved through matrix equations. Explicit methods are employed when the degree of nonlinearity in the model is starting to pose problems for Implicit methods.

Implicit methods do not place intrinsic limitations on the time increment size; increment size is generally determined from accuracy and convergence considerations. On the contrary, explicit models typically require several orders of magnitude more increments than implicit ones (smaller increment size), but their computational cost per increment is far lower.

For the conceptual understanding of the different solving procedures, a simple fixed-free truss problem is proposed [52]. The stress-wave model is shown in its time evolution.

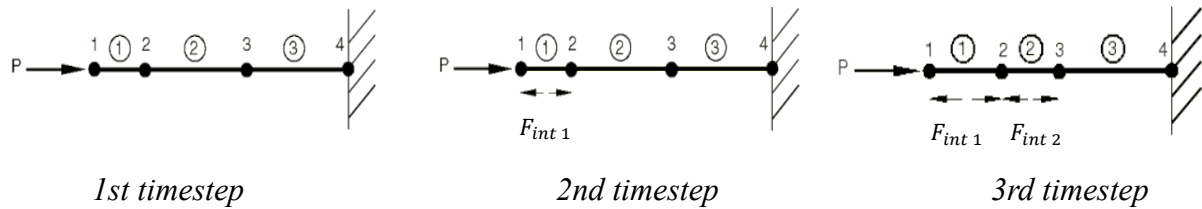


Figure 40 Free body diagram of stress wave propagation [52]

The initial configuration at the left-hand side is perturbed by an axial force P. At the first timestep, the first element experiences an acceleration from which strain and stress can be calculated by integration. At the second timestep, the second element experiences the reaction force from the first element, and so forth.

First timestep computation:

1. *Dynamic equilibrium equation* $\ddot{u}_1 = \frac{P}{m_1}$
2. *Explicit integration* $\dot{u}_1 = \int \ddot{u}_1 dt \quad u_1 = \int \dot{u}_1 dt$
3. *Compute strain and stress* $\Delta \varepsilon_1 = \int \frac{\dot{u}_2 - \dot{u}_1}{l_1} dt \rightarrow \varepsilon_1(t) = \varepsilon_1(t-\Delta t) + \Delta \varepsilon_1 \rightarrow \sigma_1(t) = E \varepsilon_1(t)$
4. *Compute nodal internal forces* $F_{int 1} = \sigma_1 A$
5. *Proceed with the 2nd timestep*

At the second time step, the dynamic equilibrium equation will involve also the second element on which the reaction force of the first element is applied:

$$\ddot{u}_1 = \frac{P - I_{int1}}{m_1} \quad , \quad \ddot{u}_2 = \frac{I_{int1}}{m_1}$$

m_1 and l_1 are mass and length respectively of the first element while \ddot{u}_1 refers to the acceleration of the first node. F_{int1} is the internal reaction force of the first element employed to calculate the dynamic equilibrium between the two adjacent nodes.

With this simple example it's clear that the explicit method has no need to calculate the stiffness matrix. Thus, the solver do not have to invert the matrix in order to obtain a solution which requires high computational cost.

Generalizing the computation procedure:

1. Dynamic equilibrium equation

$$[M]\{\ddot{u}(t)\} = \{F_{external}(t)\} - \{I_{internal}(t)\} \rightarrow \{\ddot{u}(t)\} = [M^{-1}] (\{F_{ext}\} - \{F_{int}\})$$

Where the mass matrix $[M]$ is usually a diagonal or lumped matrix and therefore inexpensive to invert.

2. Explicit integration

$$\text{Velocity: } \dot{u}_{(t+\frac{\Delta t}{2})} = \dot{u}_{(t-\frac{\Delta t}{2})} + \ddot{u}_{(t)} \frac{\Delta t_{(t+\Delta t)} + \Delta t_{(t)}}{2}$$

$$\text{Displacement: } u_{(t+\Delta t)} = u_{(t)} + \dot{u}_{(t+\frac{\Delta t}{2})} t_{(t+\Delta t)}$$

Accelerations are integrated using the central difference rule under the assumption of constant acceleration between two successive timesteps (this type of integration satisfies the dynamic equilibrium equations at the beginning of the increment). Velocity is integrated and added to the previous timestep displacement.

The term “explicit” refers to the fact that the state at the end of the increment is based solely on the displacements, velocities, and accelerations at the beginning of the increment. For the method to produce accurate results, the time increments must be small enough so that accelerations are nearly constant during an increment.

3. *Compute strain and stress*

The strain rate is calculated from the difference between nodal velocities, its explicit time integration results in the element strain increment. The element stress is computed from the constitutive equation of the material and the element strain.

4. *Compute nodal internal force vector*

The nodal internal force is used to solve dynamic equilibrium equation of the following timestep.

5. *Timestep increment and return to step 1*

To ensure stability and accuracy of the solution, the size of the timestep used in Explicit time integration is limited by the Courant-Friedrichs-Lewy (CFL) condition [43]. This condition entails a limitation to the maximum timestep, such that a stress wave cannot travel farther than the smallest element characteristic dimension of the mesh on a single timestep. Therefore, this timestep criteria is employed for ensuring the solution stability.

$$\Delta t_{timestep} \leq f_{STF} \cdot \text{MIN} \left(\frac{l_c}{c} \right) \quad (13)$$

Where f_{STF} is the stability timestep factor (0.9 by default in Autodyn), l_c is the characteristic element dimension (square root of shell area for QUAD elements) and c is the speed of sound in the element. This speed depends solely on material properties, in particular on density and stiffness while it is independent on loading type and duration. Care should be taken when generating meshes for explicit dynamics simulations, to ensure that few very small elements do not control the global timestep.

Alternatively, it is possible to increase the density of some smaller element of the mesh in order to increase its CFL minimum timestep. This technique, known as “Selective Mass Scaling”, allows to make the timestep more homogeneous throughout the mesh. In ANSYS, the addition of mass is controlled by the minimum timestep to be achieved. This value has to be set up manually with few iterations, by controlling the mass added (output) to achieve the set CFL timestep (input). It is necessary to make sure that the mass values are still realistic and do not interfere with the physics of the results.

Because of the nature of the two methods, the explicit solver is more suitable for nonlinear problems, working with a large number of computationally inexpensive iterations (simulations often require around 10^5 cycles). Furthermore, while local mesh refinements are preferable for implicit solvers, in explicit solvers a uniform mesh size is needed since the smaller element

directly controls the whole model solving time. ANSYS manual points out that explicit problem intrinsically works better with evenly distributed QUAD elements which benefit the solution accuracy regardless the time needed to solve the model [43].

Finite Elements

For the analysed thin-walled structure, shell elements (Triangular, Quadrilateral) are considered more appropriate than solid finite elements (Tetrahedron, Hexahedron) which would need to have more elements across the wall thickness, resulting in a non-feasible small timestep. Furthermore, shell elements are already successfully employed all the numerical analysis mentioned in the literature review chapter.

Shell elements are used to model structures in which one dimension, the thickness, is significantly smaller than the other dimensions [53]. Surface elements are used to define the geometry while thickness is only given as a section property.

ANSYS Autodyn supports only linear elements with reduced integration:

- Quadrilateral 4 noded shell element based on Belytschko-Tsay formulation [54] which is affected by hourglass effect, and it needs to be stabilized by hourglass control techniques.
- Triangular 3 noded shell element based on Belytschko formulation [55].

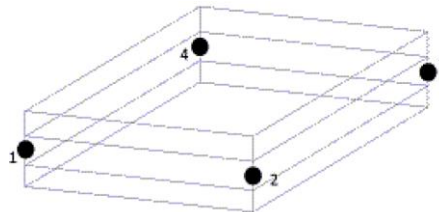


Figure 41 Quadrilateral element with 3 integration points through the thickness [43]

Reduced integration linear elements have only one integration point per layer at the element centroid. This number of layers through thickness is set to five. More shell layers are also tested but no significant differences occurred.

A limitation of this finite element is the stress in thickness direction which is set to zero. The thickness is instead updated in accordance with the material properties (such as deformation due to Poisson's ratio).

Hourglass Effect

The particular 4 node QUAD elements with only one integration point used in Explicit Dynamics can suffer from their own typical numerical problem, called “hourglass” deformation mode.

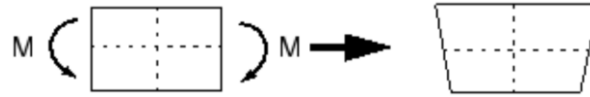


Figure 42 Hourglass deformation mode [56]

In the illustrative example above, none of the dotted lines has changed in length or angle. Therefore, components of stress and strain at the element's single integration point remain unchanged when calculated with explicit strain formulation previously described. This results in a zero-energy unphysical mode which does not increase the strain, and as direct consequence, does not increase the element resistance to such a distortion [43]. The Hourglass damping methods implemented in Autodyn attenuate the hourglass mode by adding corrective forces in the element which create the so called artificial “hourglass energy”. The Flanagan Belytschko [57] formulation is recommended if large rotations are involved in the model.

Energy error

Energy conservation is a measure of the quality of an explicit dynamic simulation. Poor energy conservation usually implies a non-optimal model definition. The energy conservation is accounted through the energy error defined below:

$$E_{error} = \frac{|E_{Current} - E_{Reference} - E_{Work done}|}{MAX(|E_{Current}|, |E_{Reference}|, |E_{Work done}|)} \quad (14)$$

$E_{Current}$ accounts internal, kinetic and hourglass energy of the current cycle, $E_{Reference}$ is the energy of the reference cycle (initial timestep by default) and $E_{Work done}$ includes the energy contribution from loads, constraints, body forces, erosion and penalty contact forces. A simulation with more than 10% energy error should not be considered accurate.

Contact

Trajectory of nodes and faces is tracked during each cycle. A contact event is detected when the trajectory of a node and a face intersects. The option “body self-contact” implemented in the solver allows the contact detection algorithm to check all interactions automatically. This option allows to consider both body self-contacts and contacts with other bodies, which makes the analysis more robust even though it requires more computational effort.

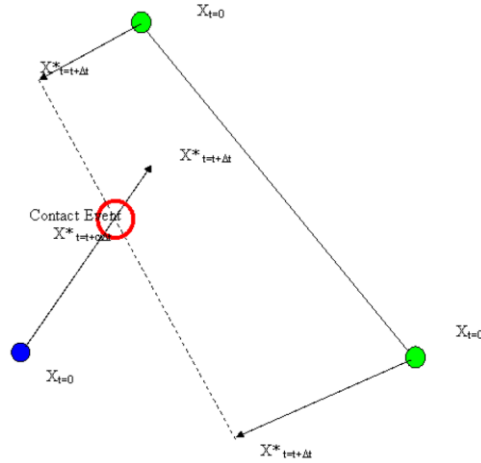


Figure 43 Contact detection by trajectory method [43]

When contact is detected, a local “penalty force” is calculated to push the nodes and eliminate the penetration. This force is linearly proportional to the depth of penetration and dependent on the mass of node and face involved, acting like a spring.

$$F_{penalty} = \left[\frac{0.1}{\Delta t^2} * \frac{m_{node} * m_{face}}{m_{node} + m_{face}} \right] * \Delta D_{penetration} \quad (15)$$

Linear and angular momentum is conserved since opposite forces are calculated on the nodes of the intersected face. However, the process takes several cycles to meet the contact condition after the penetration and still a perfect zero-penetration is never achievable. The contact option “Shell Thickness Factor” and “Nodal Shell Thickness” implemented in the solver, allows to simulate the actual thickness of the surface body by offsetting the shell element faces and points radius of influence on which the contact is detected.

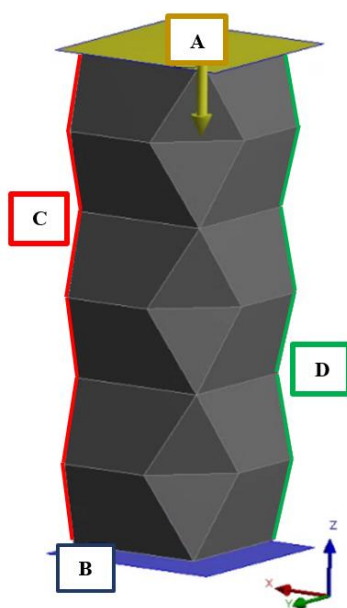
3.4.2 FEM model settings

The crushing scenario was modelled to replicate the experimental test conditions. The origami tube stands between two rigid panels modelled with rigid shell elements with fully constrained nodes. One rigid plate has fixed displacement and rotation while the other one has a velocity boundary condition which allows the plate to move in axial direction with a predetermined speed while having no displacement in the other directions.

The maximum crushing stroke is set to 70 mm in accordance with previous works [5], in such a way the bottoming out of the tube is avoided, which implies high reaction force and large mesh distortions.

The upper and lower free edges of the origami tube are initially placed at 0.05 mm from the rigid plate in order to avoid contact interference from the first timestep of the analysis which leads to high noise and contact force oscillation in the first part of the simulation. The first iterations are subjected to noise because of the initial contact shock and the high stiffness of the tube in elastic regime. For the same reason, a ramped velocity starting from a lower velocity value, is applied in the first part of crushing.

A frictional contact is set for both contacts, between rigid plates and tube and tube self-contact. A value of 0.3 for both static and dynamic friction is employed. This value shows a good agreement in induction of the mode between FEM simulation and experiment.



- A) Rigid shell elements plate
 - X and Y displacements fixed
 - Downward Velocity in Z direction
- B) Rigid shell elements plate
 - All displacements fixed
- C) Symmetry B.C. on ZY plane
- D) Symmetry B.C. on ZX plane

Figure 44 Quarter of model FE geometry and boundary conditions

Quarter tube model rather than full tube model is used in the numerical simulation. Symmetric boundary conditions were assigned to the tube edges at the two planes of symmetry. The present tube with height to minimum cross section width ratio around than 2 and cross section width to thickness ratio higher than 30 which is expected to buckle progressively [58].

A full tube, half tube and quarter tube FEM analysis is conducted to further validate the hypothesis and no differences are found in the models.

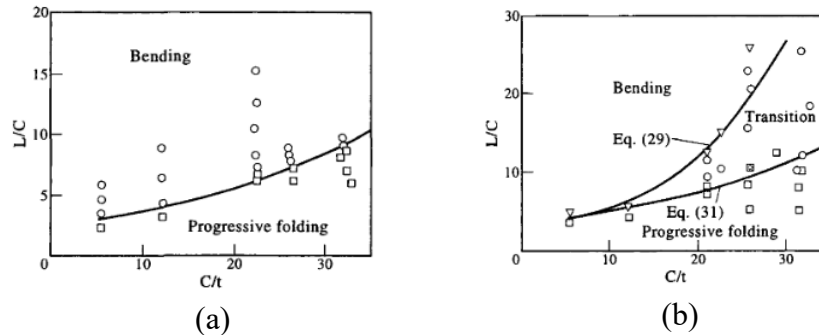


Figure 45 Buckling mode map for squared tubes: (a) Quasi static, (b) Dynamic [58]

Mesh

As already discussed, present geometry is modelled through Shell elements since they were successfully employed in the previous analysis regarding thin-walled structures.

According to ANSYS Dynamics Analysis guide [43], for explicit solvers the mesh needs to have a uniform characteristic dimension, due to CFL condition and solution accuracy considerations.

The patch-independent meshing methods available in ANSYS meshing generally produce a more uniform mesh with a higher timestep than patch-dependent meshing methods. This meshing algorithm can apply a gross defeaturing on edges and vertices of the geometry, still respecting manually selected topologies or geometries related to boundary conditions, which are not crossed [59].

In particular, the “Uniform MultiZone Quad/Tri method” mesh algorithm is used for the global mesh generation. This patch independent method decomposes the geometry into structured (or “mapped”) or unstructured regions to be meshed with Quad elements if possible (few Tri elements are used to avoid large mesh distortions and achieve a better overall quality of the mesh). A uniform global mesh is achieved thanks to this method.

Two main problems were detected in the “non-mapped” mesh. Firstly, the element next to the slender edge can suffer from high distortion caused by high stress concentration, which results in an energy conservation error. Secondly, element distortion leads to a drastic reduction of characteristic length and therefore a drop in minimum timestep, until ten times smaller than the one of the undeformed initial shape. This configuration implies a considerably longer computation time.

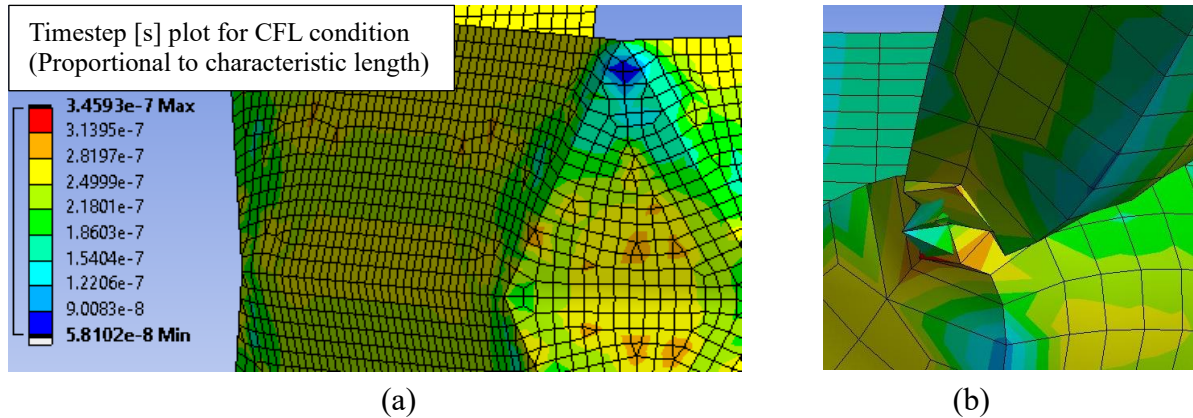


Figure 46 Non-mapped mesh problems: (a) element distortion, (b) energy error

A manually-defeatured geometry has been tested in order to solve the problem. A 45° bevel was applied to the edge to allow allows a 2 element / 3 nodes discretization of the edge. The configuration does not show any benefit due to the further refinement of the edge, principally due to the fact that the characteristic dimensions of the bevel and of the other tube features have different orders of magnitude, in contrast to the uniform mesh size needed in the analysis.

The most stable solution in term of timestep stability is found in a fully Quad mapped surface, in which “Uniform MultiZone Quad/Tri method” is maintained as global mesh method. Furthermore, the mapped mesh shows better mesh quality compared with the non-mapped one.

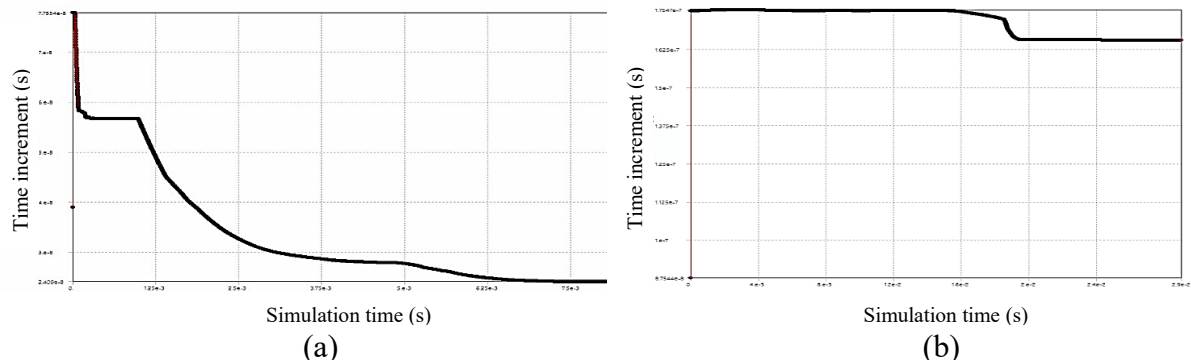


Figure 47 Time increment plot: (a) Non-mapped mesh, (b) Fully Quad mapped mesh

A sensitivity analysis is performed in order to achieve a compromise between computational time required to solve the mathematical problem and solution accuracy. A global sizing of 1.5 mm is set as fine mesh case which represent the reference force value for the relative error computation in the following mesh convergence analysis.

The solution has a little sensitivity, in terms of medium force, for global sizes close to 1.5 mm (6700 elements), therefore the global mesh size of 1.5 mm offers a good reference output. The maximum force is also symptom of quantity of noise in the FE problem which is affected by mesh sizing.

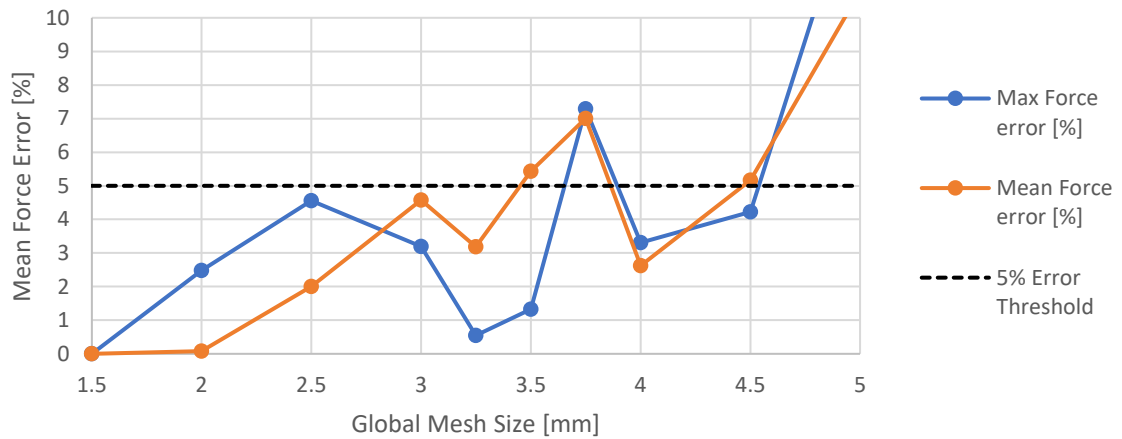


Figure 48 Mesh sensitivity – Mapped mesh

With a very coarse mesh, apart from the force errors, several other problems arise. The high noise in the solution output leads to oscillating force reaction that implies non-physics high force peaks and a change in force trend. Compenetration problems and hourglass due to the severe mesh deformation, are evident in coarser meshes.

$$Error = \left| \frac{Value - Ref}{Ref} \right| \times 100 \quad (16)$$

The mesh size of 2 mm (3800 elements) is chosen for the following analysis to avoid undesirable outcomes such as noise or change in force trend. The model guarantees a reasonable computational time, around (25 minutes) and a CFL time increment of $1.75 \cdot 10^{-7} \text{ s}$ which remains almost constant throughout the computation.



Figure 49 Meshed tube

The mesh criteria are calculated in ANSYS Workbench environment.

<i>Mesh properties</i>	<i>Averaged</i>	<i>St. deviation</i>	<i>Recommended [59]</i>
<i>Aspect ratio</i>	1.14	0.13	
<i>Jacobian ratio</i>	0.94	0.06	
<i>Warping Quad</i>	$1.5 \cdot 10^{-7}$	$2.1 \cdot 10^{-7}$	max 0.1
<i>Max corner angle Quad</i>	101°	9°	
<i>Skewness</i>	0.13	0.10	max 0.25
<i>Tri to Quad ratio</i>	0 %	0 %	max 5%

Table 5 Mesh quality criteria

An illustrative description is showed in the following picture.

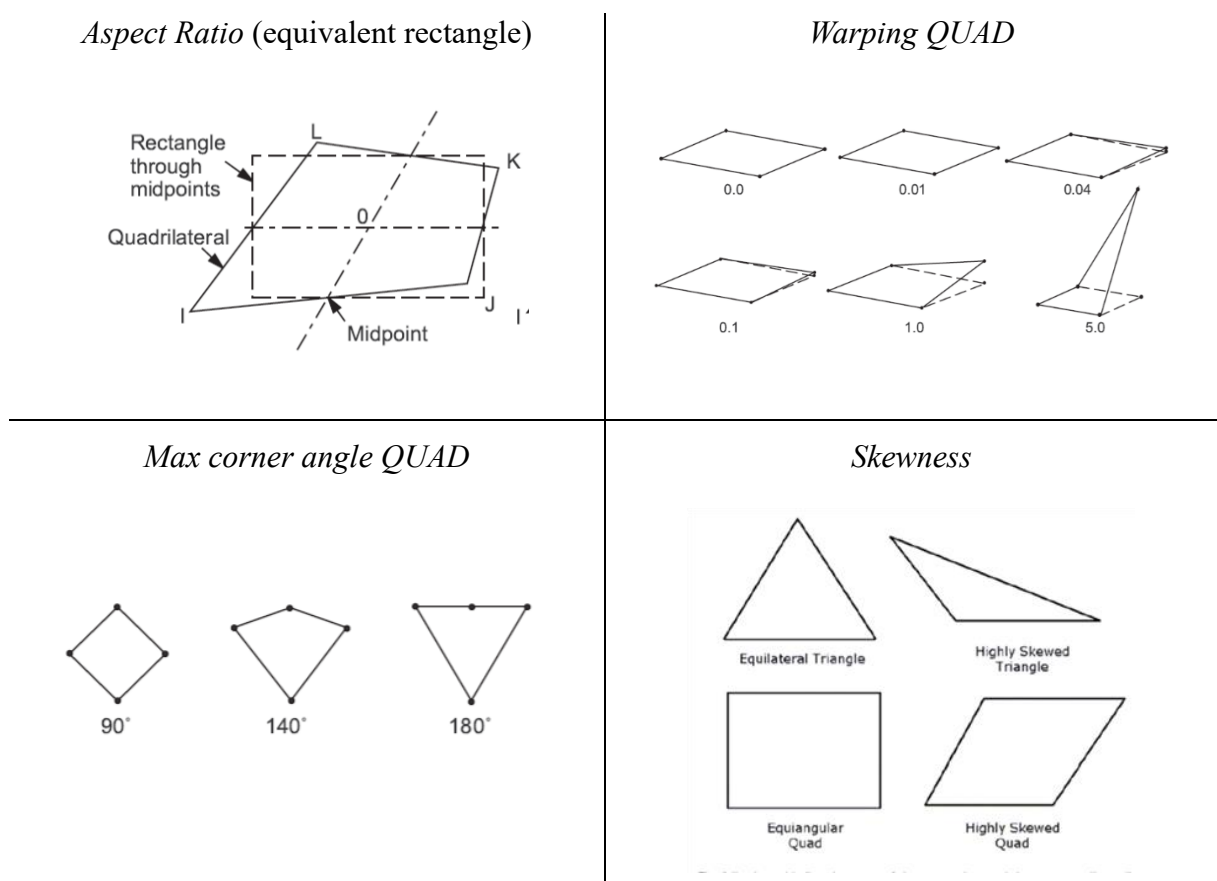


Figure 50 Mesh characteristic parameters illustration [59]

Timestep sensitivity

Ideally the FEM solver should simulate the velocities of the actual time event. However, this is not practically feasible for a Quasi-Static explicit analysis. The event time span (called “end time”) is directly proportional to the number of iterations to be solved and therefore it heavily influences the final computation time. For instance, for the present FE model the CFL minimum time increment between two following cycles is in the order of magnitude of 10^{-7} s while the Quasi-Static experiment duration is in the order of 10^4 s.

An end time of 0.02s (3.5 m/s crushing velocity) is chosen for the Quasi-Static simulation. The choice is based on the output examination of different time scaled solutions. In the same fashion as for mesh size sensitivity; the ending time and the related crushing velocity are chosen for ensuring a Quasi-Static regime (no force peaks due to dynamic events and kinetic to internal energy ratio conservatively less than 5%). Furthermore, according to the ANSYS dynamic manual, the velocities inside the model should be kept in the range from 1 to 10 m/s to be correctly modelled.

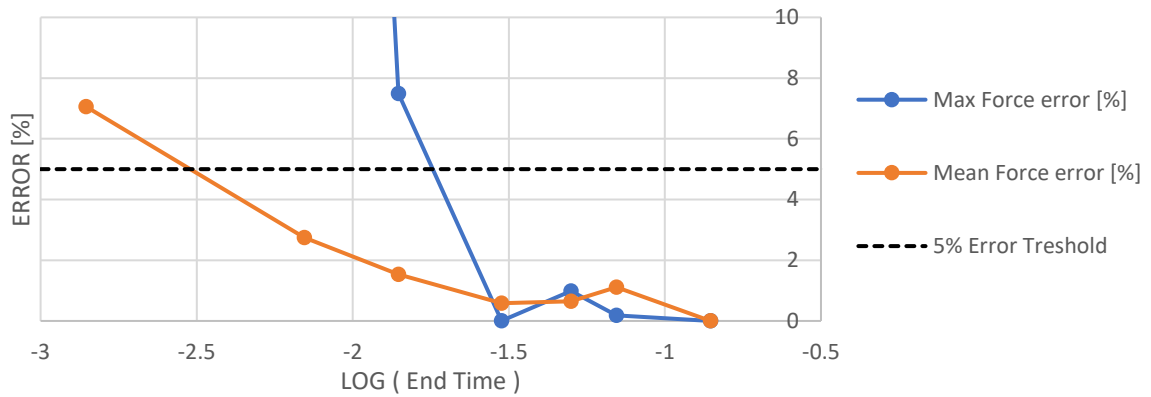


Figure 51 Timestep sensitivity

3.5 Results

3.5.1 Experimental test on straight cylindrical tube

A first experimental investigation on a Al6063 cylinder tube is performed in order to study the naturally triggered diamond mode. Aspect ratio ($l/d=2$) and thickness diameter ratio ($d/t=35$) are chosen to be comparable to the one of the origami tubes select as reference geometry.

Several conclusions can be drawn from this phenomenological study.

The low crushing efficiency of 44% is due to the initial high buckling force, while the post-buckling crushing has a flatter reaction force trend.

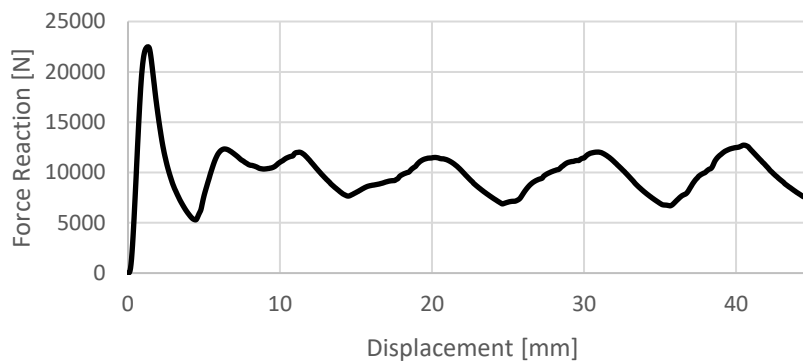


Figure 52 Cylindrical tube Force – Displacement curve

The resulting mixed mode starts as concertina mode for the first folding, while it continues in diamond mode. Its particular mode shape has only three lobes in tangential direction, while a squared origami-patterned tube should induce four folding lobes tangentially, which create more plastic hinges.

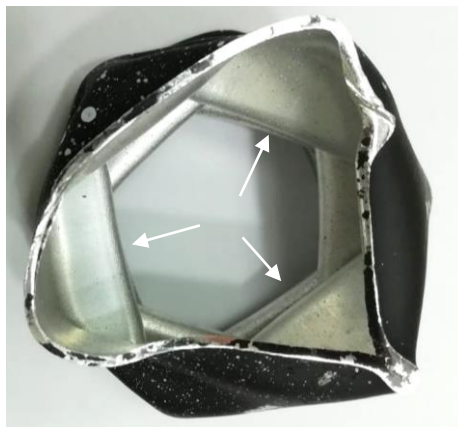


Figure 53 Natural 3 lobes diamond mode

DIC data show that strain rate concentrates on folding lobes, while the rest of the tube experiences around one order of magnitude lower strain rate.

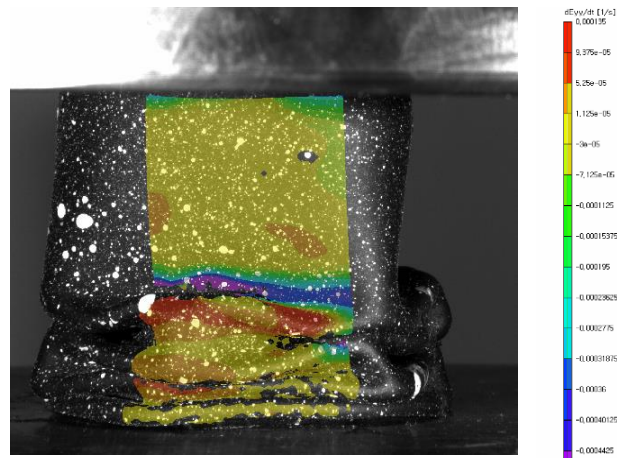


Figure 54 Straight tube strain rate distribution

3.5.2 Experimental test on AlSi10Mg origami tube

The employment of 3D printed aluminium alloy can considerably reduce the structure weight, with a density around one third the steel alternative, which potentially benefits the specific energy absorption. However, the quasi-static analysis crushing of the 1.5 mm thick origami tube shows an extensive occurrence of fractures which localises the crushing phenomenon in the cracking zone, causing a sharp drop in performances.



Figure 55 AlSi10Mg specimen fractures

The tube started cracking at 20 kN during its initial elastic slope, while it was expected to buckle at 35 kN (estimated from prior FE analysis). The material failed in a completely brittle manner, therefore, AlSi10Mg cannot be utilised for realizing such a crushing structure which is expected to undergo large plastic deformation. This material will not be further investigated in this dissertation.

The first crack emerged at the interface between tube free edge and UTM rigid plate. It suddenly propagates in axial and tangential direction along the edges of the patterned geometry. Its crushing process is dominated by a large crack propagation, which results in a load localization at the cracking zone as showed by the DIC analysis. The reaction force, that keeps increasing during the elastic crushing slope, suddenly drops until around 2 kN.

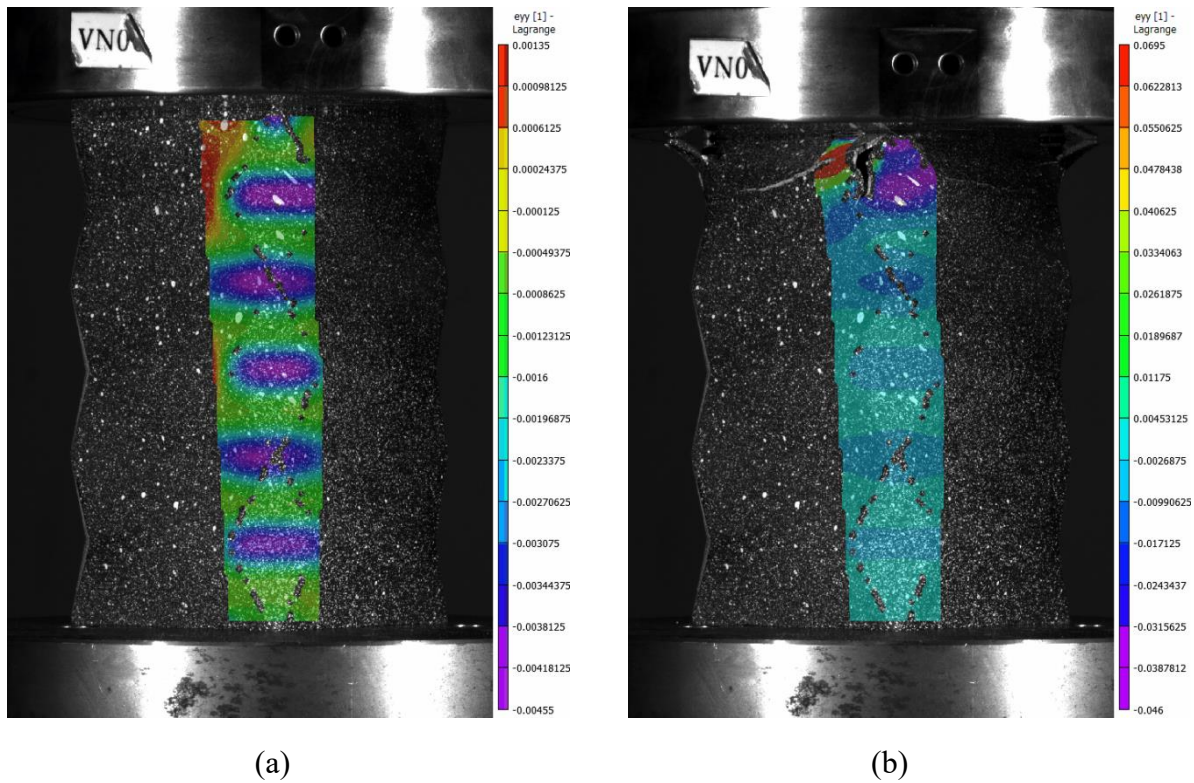


Figure 56 DIC axial strain: (a) pre-fracture, (b) post-fracture

3.5.3 Experimental test on SUS316L origami tubes

Lastly, several additively manufactured specimens in SUS316L are tested. According to specifications given by the manufacturing company, the material has excellent mechanical performance, which made it a good candidate for a high specific energy absorption.

Three different configurations are tested in this study. Annealed, filleted edges and lower thickness configurations are tested, in order to solve the fracture problem encountered in the first specimen. In total, two different geometries are printed.

Sharp-edged 1.5 mm thickness specimen

The first SUS316L specimen exhibits exceptionally promising results in the first part of the crushing, while it suffers of localized cracking at the lobe folding stage. This specimen correctly reaches its buckling load and successfully trigger diamond mode, maintaining a nearly constant force reaction in its post-buckling stroke.

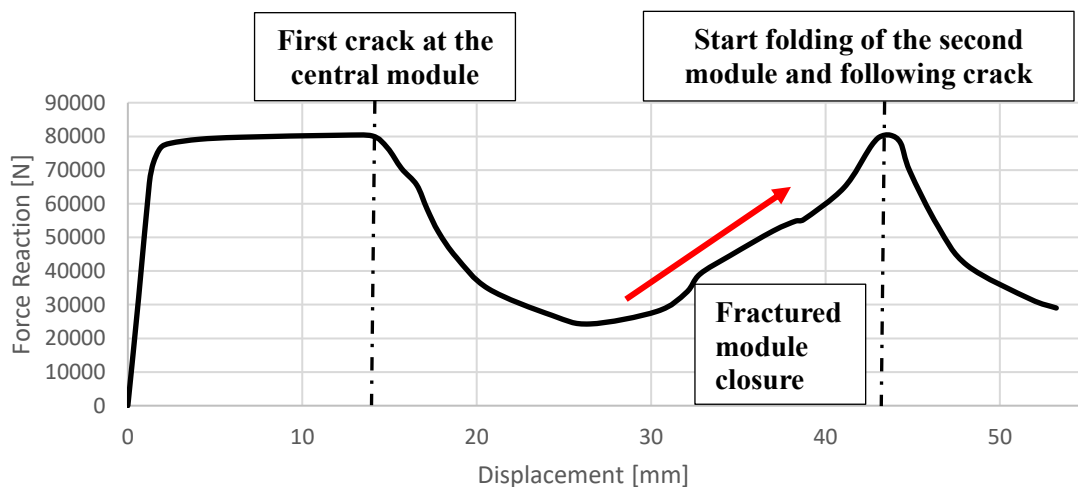


Figure 57 SUS316L 1.5 mm thick origami Force – Displacement curve

By referring to the distinction of first and second crushing stage, introduced by Jiayao Ma et al. [3] and introduced in chapter 2.2.1, it is possible to notice that the crack happened at the beginning of the folding phase of the single module.

Since the fracture was on an edge which was surrounded by an area under compressive load, the crack did not extensively propagate like the case in AlSi10Mg. However, it compromises the tube stiffness, resulting in a low crushing reaction force, until the fractured lobe bottomed out, and the folding stage started in the neighbouring lobe, which cracks in the same manner.

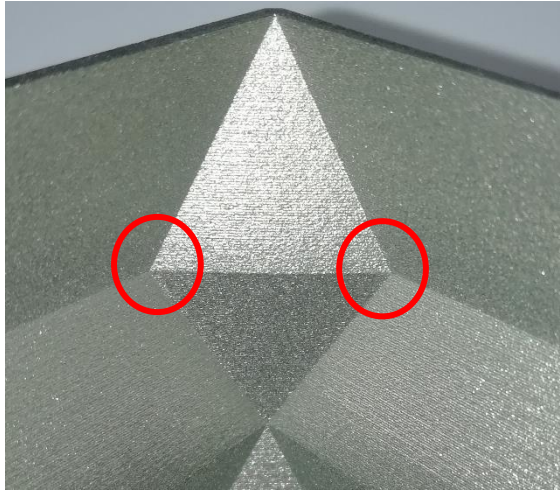


Figure 58 Fracture initiation points

The following picture is representative of the complex 3D strain field at the edges. A high strain zone is noticeable on the right-side corner, while the opposite edge is already fractured.

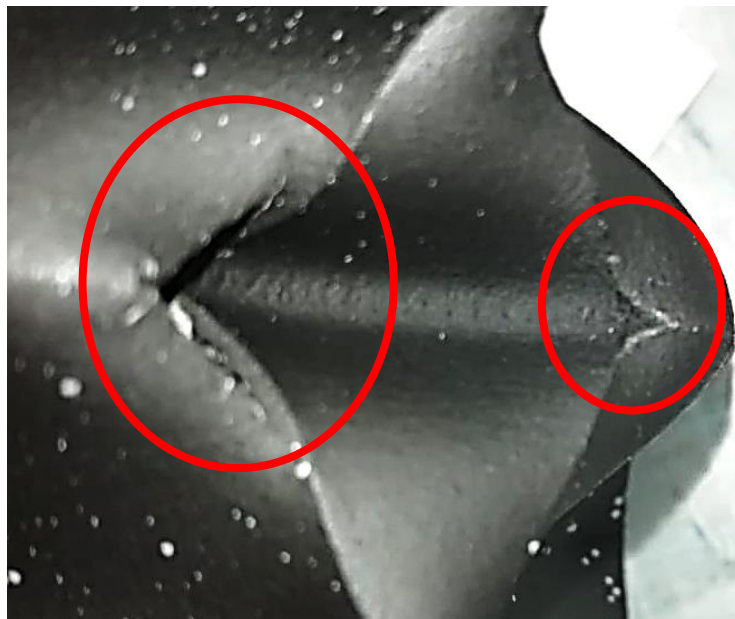


Figure 59 Partially crushed second module

The two in-plane principal strain components are computed through DIC technique, the following image shows their field right before the fracture start:

- The first principal strain component indicates a concentration of tensile strain on the area that undergoes cracking. This component reaches +7% at the start of cracking.
- The second principal strain component shows compressive load at the narrow section between module interface and the edge of the folding lobe with a magnitude of -17%.

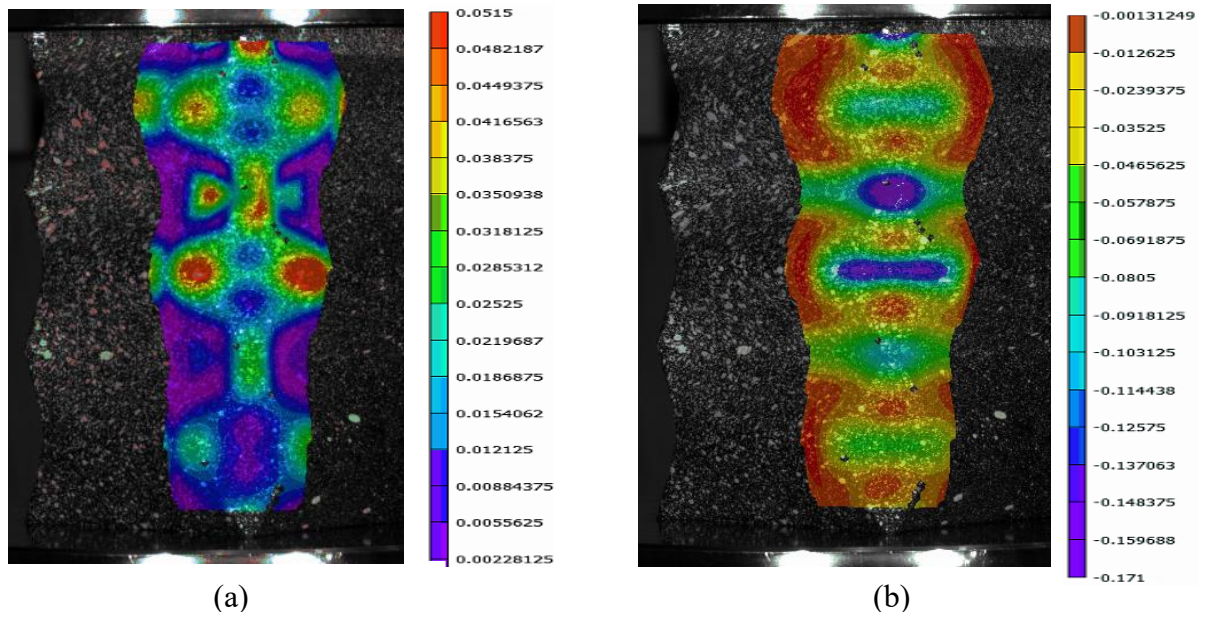


Figure 60 Principal strain field components: (a) 1st tensile, (b) 2nd compressive

The extensive cracking issue is not reported in any of the publications in literature. The fracture initiation point happens to be the convergence point of several sharp edges. Previous works dealt with stamped tubes, which are technologically bound to have rounded edges.

Annealed sharp-edged 1.5 mm thickness specimen

A second specimen of the same geometry is annealed in order to seek an increased ductility as a first trial to avoid cracking. The annealing procedure is performed at the maximum temperature of 1050°C in vacuum atmosphere, following three temperature steps (500°C – 1h, 850°C – 2h, 1050°C – 2h) for avoiding thermal shocks and thus geometrical deformations. The original additive manufactured specimen had already a stress-releasing heat treatment, after the additive process.

The annealed specimen cracks in the same fashion as the as-built origami tube. The first part of crushing is shown in the following plot, along with the as-built case for comparison. The crack emergence is delineated by the dashed line at around 15 mm of crosshead displacement.

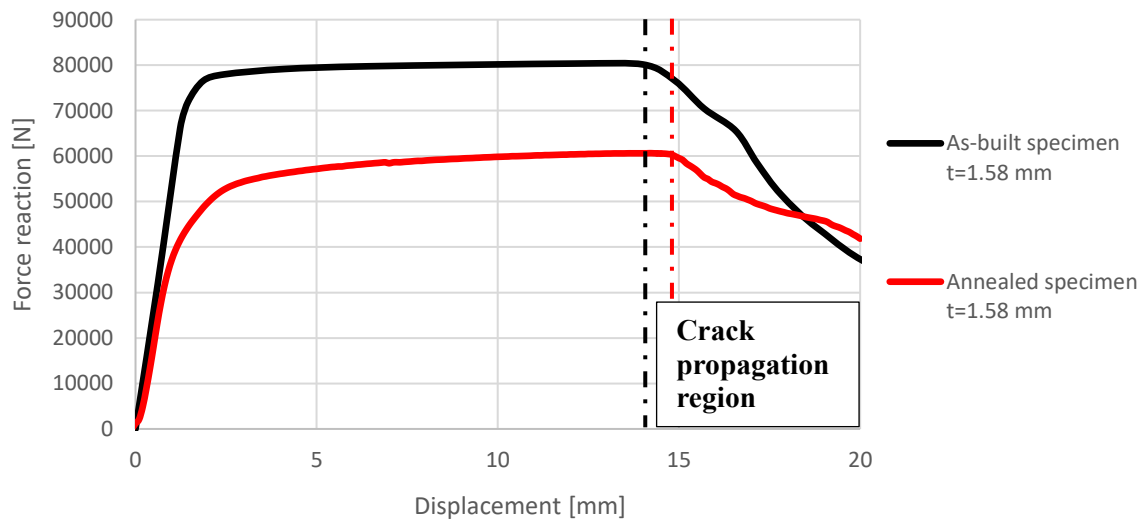


Figure 61 Comparison between as-built and annealed SUS316L origami

While the force reaction drops from 80 kN to 60 kN, there is not a visible advantage for the problem of interest. Previous studies on AM SUS316L detected a much lower sensitivity to annealing compared to the wrought material; while strength decreases, ductility does not necessarily increase with higher annealing temperatures [60].

It is interesting to notice that by changing the material properties, the collapsing mode starts from the side module instead of the central one (previous case). DIC shows a concentration of tensile strain up to +12% principal in-plane strain at the start of cracking .

Rounded edge 1 mm thickness specimen

This specimen was realised after a comparative analysis with its finite element model, presented in the next chapter. Thinner wall thickness and fillet radius at the edges were considered as features potentially capable to avoid fracture.

An attenuated but similar trend is found for this last specimen. Cracks happen at the external module (dashed line), which subsequently bottoms-out and triggers buckling in the following module which results in a new fracture. This cycle is repeated for all the three modules. The following plot shows its force-displacement trend.

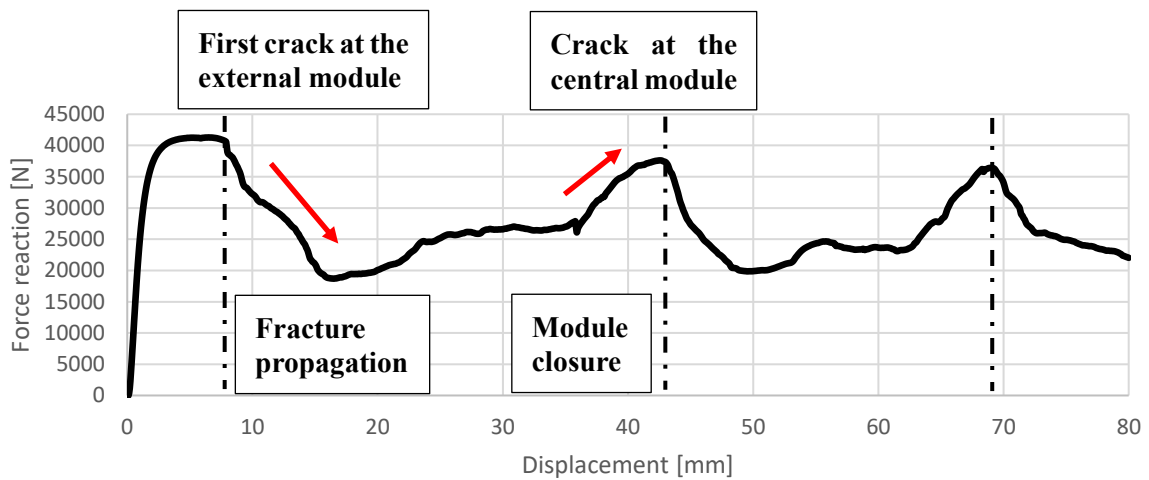


Figure 62 SUS316L 1 mm thick origami Force – Displacement curve

The first crack happens at 8 mm of crushing stroke, since the lobe-folding phase is already reached in the thinner specimen. As expected, a larger area undergoes deformation around the plastic hinge under tension which triggers the crack. As a result, a smoother transition is achieved between the lobe surface and the adjacent side surfaces.

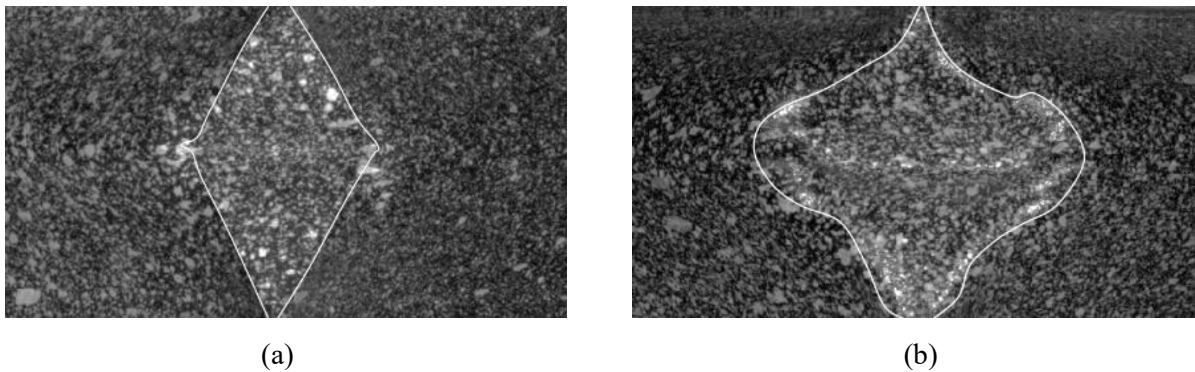


Figure 63 Lobe geometry before cracking: (a) 1.5 mm thick, (b) 1 mm thick rounded

In this experiment only one side of each lobe fractures. Consequently, the tube stiffness is in some extent preserved and thus, the drop in reaction force lowered, if compared with the previous case.



Figure 64 Crack developed on one side

The DIC analysis indicates that the principal strain component reaches +11% at the lobe edge, right before the fracture initiation at 8 mm of stroke.

3.5.4 Comparative analysis with FE model for SUS316L origami

The causes of the problem encountered in the first SUS316L specimen have been investigated through explicit FEM analysis. The geometry is known and material properties are given from the manufacturer through a series of tensile tests.

The explicit FE model slightly underestimate the buckling force of the origami tube, while the subsequent crushing force has an upward trend which is not reported in the experiment. At 15 mm of displacement, the experimental reaction force drops because of the crack and the consequent loss of stiffness. Another difference is found in the elastic slope at the beginning of crushing, which results in a stiffer behaviour. This discrepancy is also visible in all previous works reviewed in the literature section [3] [8] [5] [39] [61].

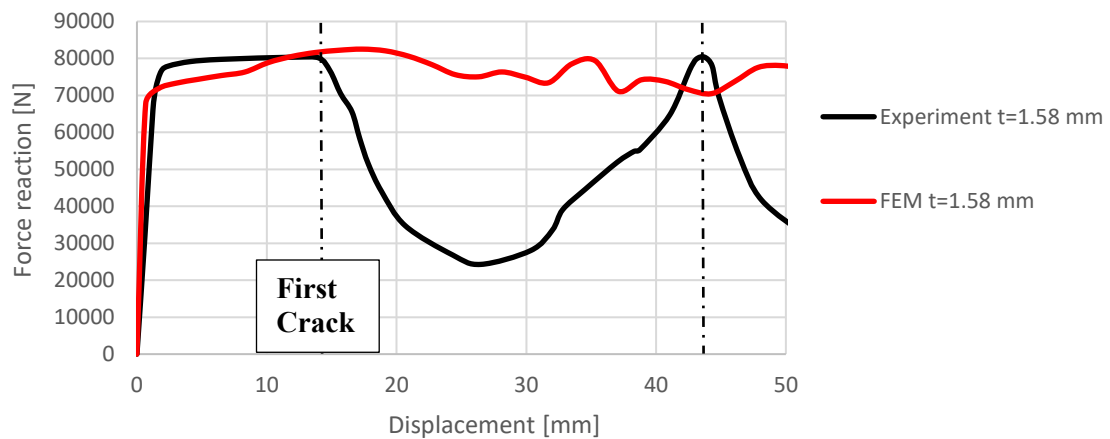


Figure 65 Comparison between numerical and experiment force reaction

The model was proofed have a minor sensitivity to module intersection bevel and external edge rounding due to the AM procedure (both outlined in section 3.2.2), oblique or straight plate-to-tube contact surface, mapped and unmapped mesh. A high sensitivity is found in yield point and strain hardening, which might be poorly predicted by the available data, since material properties are extremely dependent on the printing settings.

Material properties sensitivity

The tensile tests provided by the manufacturer are not representative of the specific printing job of the origami tubes, therefore an analysis on the sensitivity of material properties on tube force trend is performed.

Data on compressive behaviour of AlSi10Mg suggest that yield stress can substantially increase under compression, furthermore, the EOS M400-4 material specifications [46] indicate an average yield stress up to 550 MPa for SUS316L. This range is used to model new material properties and perform the sensitivity analysis. Hardening coefficient (K), ultimate elongation and UTS are maintained constant for constructing the new Ludwik material models. It must be noted that in the chosen model, a higher yielding point implies a lower initial plastic tangent modulus.

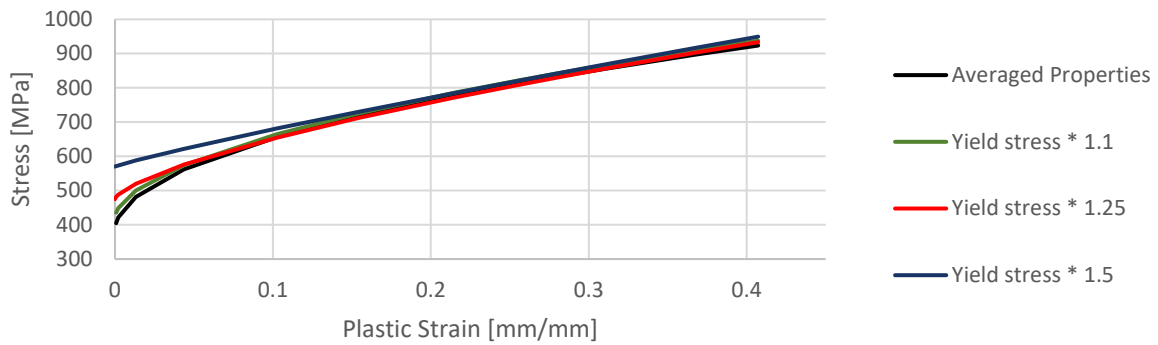


Figure 66 Strain hardening curves for yield stress sensitivity

Material yield stress has a primary influence on the initial buckling force, which is underestimated in the correlation between FEM and experiment.

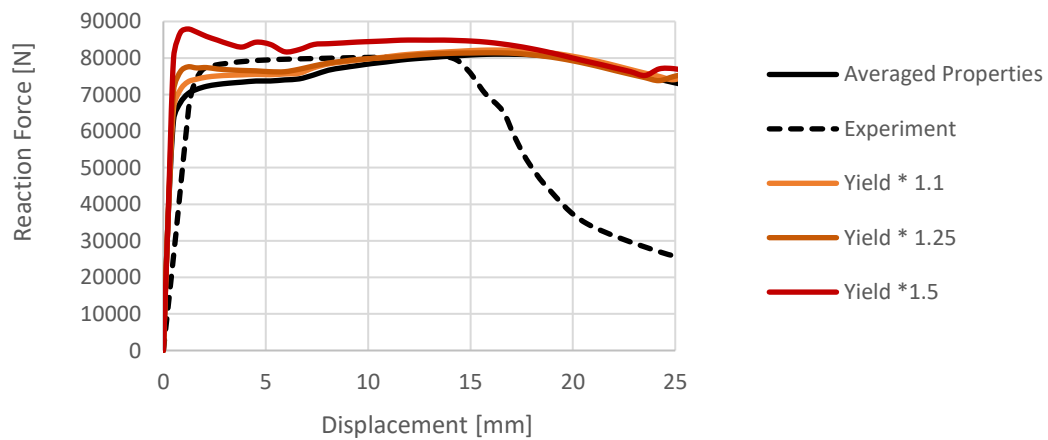


Figure 67 Sensitivity to yield stress variation

Tensile tests data show a high standard deviation in Young modulus (60 GPa), therefore this range is used for the following sensitivity analysis.

Elastic module variations create a neglectable offset in reaction force, and a minor reduction in stiffness during the initial elastic slope. Both maximum and medium force calculated over the 70mm stroke are in the range of $\pm 4\%$ from the averaged value case.

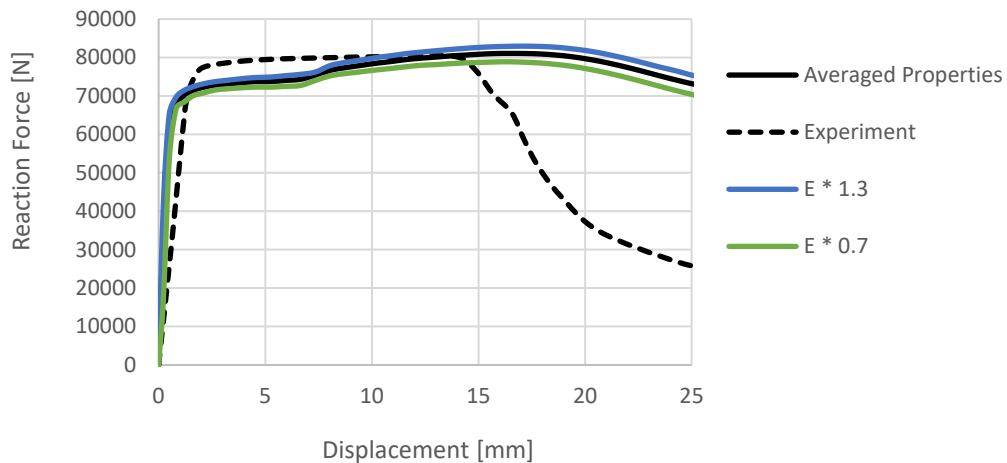


Figure 68 Sensitivity to elastic module variation

Investigation on stress field at the cracking point

At 15 mm of stroke (first crack in the experiment) the modelled Von-Mises stress field at the fracture point shows a stress that is lower than the estimated true ultimate stress for this material. It suggests that the shell FE model employed in this analysis is not representative of the complex 3D stress field at the stress concentration point.

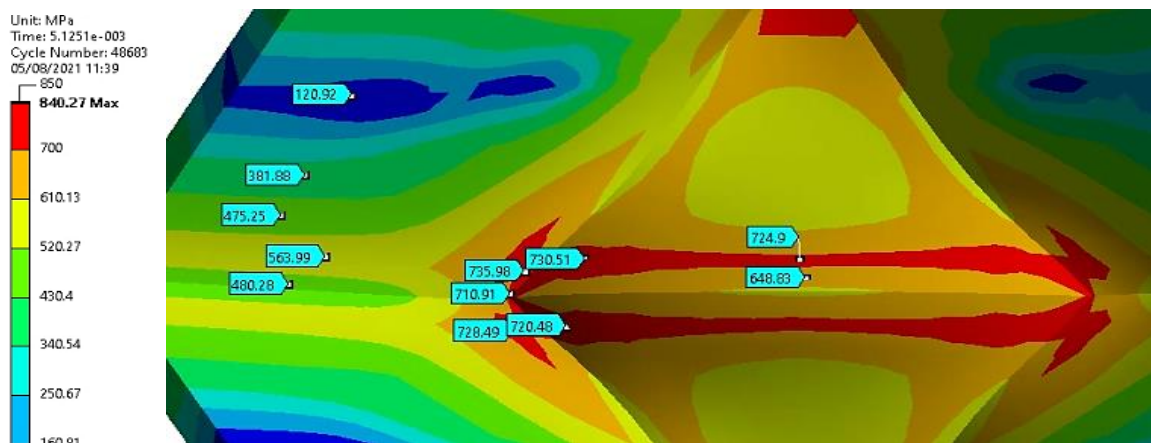


Figure 69 FEM Von-Mises stress, 1.5 wall thickness at 15mm stroke

Wall thickness influence

For the first specimens, the 3D printing company set their technological limit to a minimum thickness of 1.5 mm. After the first printing job they confirmed the feasibility of manufacturing tubes up to 1 mm of wall thickness. Therefore, a numerical comparative study using FEM is conducted to assess the pro and cons of different wall thicknesses on the same geometry.

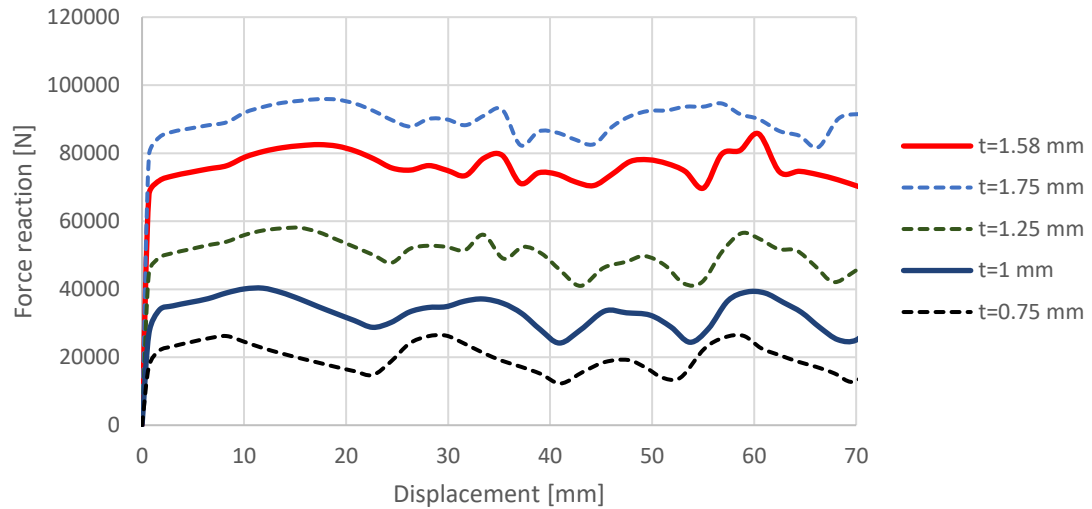


Figure 70 Sensitivity to tube wall-thickness variation

Weight decreases linearly with the wall thickness, while the absorbed energy has a stronger decreasing trend. Furthermore, according to FEM simulation, the amplitude of force oscillation around its average is similar for all the samples, while the medium force drastically changes. It results in lower crushing efficiency and specific energy absorption of thinner configurations. CFE and SEA decrease from 82.4 % and 13.9 kJ/kg to 73.0 % and 9.75 kJ/kg, by comparing 1.58 mm (first experiment) and 1 mm thick tubes. Furthermore, the first force peak and the transition in module folding stage happen at a shorter stroke in tubes with lower wall thickness. By comparing the evolution of the deformed shape during crushing of the 1 mm and 1.58mm thick tube it is possible to notice that, for the thinner structure a larger area surrounding the stress concentration point deforms so that the lobe expands beyond the prefolded shape.

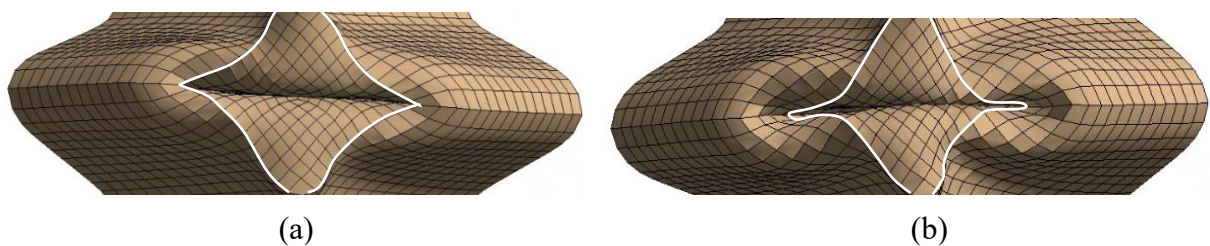


Figure 71 Lobe deformation: (a) 1.5 mm wall thickness, (b) 1 mm wall thickness

Von-mises equivalent stress is presented, for comparison with the 1.58 mm thick case. The equivalent stress plot is employed only to display the qualitative behaviour of the origami since the shell model implies a zero-stress component through the shell thickness and to neglect 3D stress effects in the material. The stress is more distributed on the lobe expansion area.

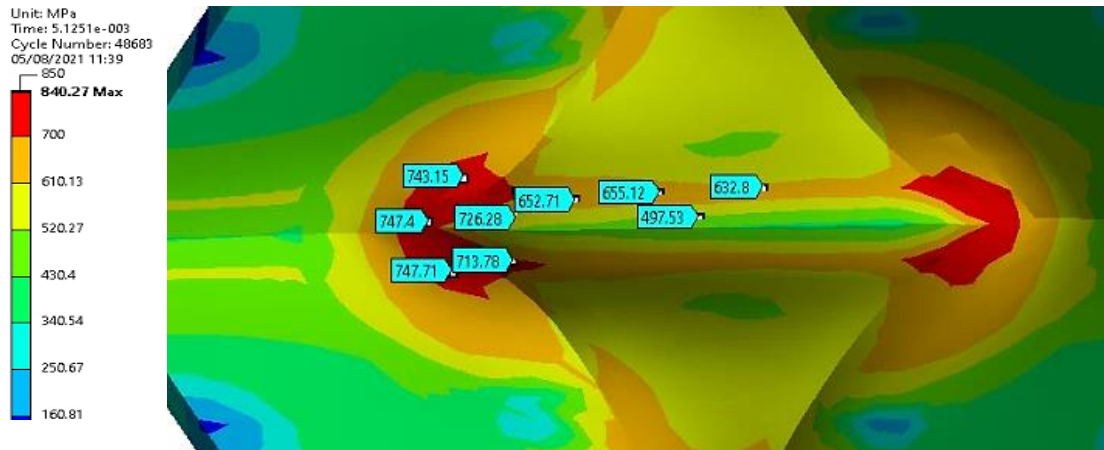


Figure 72 FEM Von-Mises stress, 1 wall thickness at 15mm stroke

The 3D stress field at the stress concentration point have to be further investigate by employing a more accurate numerical technique, capable to account stress and strain through the thickness. A solid element FE analysis can be considered for this purpose.

Fillet radius influence

Previous investigations on thin-walled origami tubes are performed on stamped specimens. Stamping a pattern with a mould implies the presence of a fillet at the pattern creases, with a radius around two times the wall thickness. No previous investigation over the fillet radius of origami patterned tubes is found in literature.

No differences are observed in the first buckling point, while peak and averaged force are slightly lower in the rounded case.

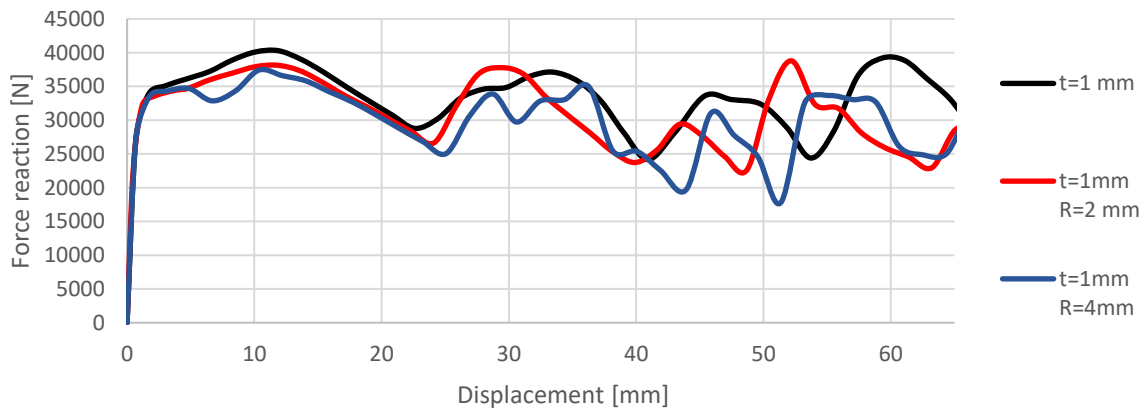


Figure 73 Sensitivity to pattern creases fillet radius variation

A bottomed out central lobe is shown for the sharp edge and rounded edge (2mm of radius) configuration. It is clearly visible that rounded edges can enlarge the area that undergoes large deformation around the lobe plastic hinges, resulting in a larger bending radius of the module.

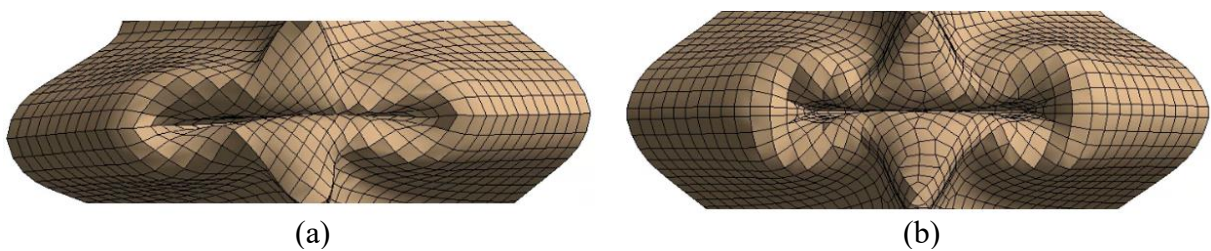


Figure 74 Lobe deformation of 1 mm thick origami: (a) sharp edges, (b) rounded edges

A factor which can influence the results, is the mesh size and morphology. The mesh realized for accounting the presence of fillets has less uniform size than the one for meshing the flat surfaces which constitute the theoretical origami shape. This is due to the fact that the characteristic dimensions of tube and fillets significantly differs, which it is not advisable for explicit analysis. Also, the computation time required changes from 25 to 200 minutes.

3.6 Considerations

The aluminium origami tube had a brittle failure during the initial elastic slope, which was not predictable from the relative FE model, due to the low stress in the cracked area. The crack initiation point at the external edge can be due to the presence of an imperfection which triggered the failure. This highly brittle material cannot be used for realizing structure that need to undergo large plastic deformation. Its collapsing mode is fully dominated by fracture propagation, which lead to extremely poor performances and predictability.

The first experiment on the stainless-steel tube, characterized by a geometry with sharp edges and higher wall thickness, shows cracks which heavily hinder the energy-absorbing performances. From the explicit FEA and DIC analysis is possible to notice a concentration of tensile stress in the area that undergoes cracking. Therefore, a comparative FEM study is performed in order to understand the highly nonlinear crushing behaviour of the SUS316L origami tube. After studying the possible causes of the failure, a more compliant tube was manufactured and tested.

A problem was found in the stiff behaviour of the surfaces that compose the origami geometry. It is outlined their tendency to concentrate the stress at plastic hinges rather than deforming themselves. A rounded fillet is applied to all the pattern edges, in order to avoid any stress concentration at the corner of sharp edges and also enlarge the area which undergoes deformation around plastic hinges. In regard to the energy-absorbing performances, the FE study suggests that a higher wall thickness is beneficial for SEA and CFE, with a prolonged initial flat force trend. The edge fillet is found to affect the tube performance in a far lesser extent.

Both DIC and shell FE model have the limitation of computing only a 2D strain field on the surface of the tube. A complete insight on the 3D field, including the strain across the wall thickness, might be crucial for the study. However, the CFL condition for explicit analysis makes nearly unfeasible the of use solid finite elements for modelling thin-walled structures.

The numerical model of the SUS316L origami slightly differs in force trend from the experiment. The simulation shows a lower buckling point and a higher upward force trend. It is observed through a sensitivity analysis that the reaction force output is highly dependent on the material yield point. A higher yield stress leads to higher buckling force, while higher strain hardening results in an upward force trend after the first buckling. The high uncertainty on material properties for the additive manufactured material might affect the numerical simulation reliability and consequently an optimization based on such a FEM model.

The few materials currently available for metal 3D printing at the local manufacturer do not permit to choose more suitable materials. A different approach has to be developed in order to manufacture origami-patterned tubes for energy absorption, in different materials.

4. DESIGN EXPLORATION

Additive Manufacturing materials SUS316L and AlSi10Mg are found not to be suitable for the origami energy-absorbing device. A new manufacturing method is under development, to stamp origami tubes in different materials from a sheet of metal. The process involves two stamping phases in succession: embossing and folding. Embossing phase is used to shape the pattern on the metal sheet, while the following folding phase is employed to close it into a half-tube, which is subsequently welded to form the origami tube. The present manufacturing method reduces the plastic deformation needed to form the part, that is confined only in the proximities of the folding edges of the pattern. A one-step deep drawing process is avoided due to its complexity.

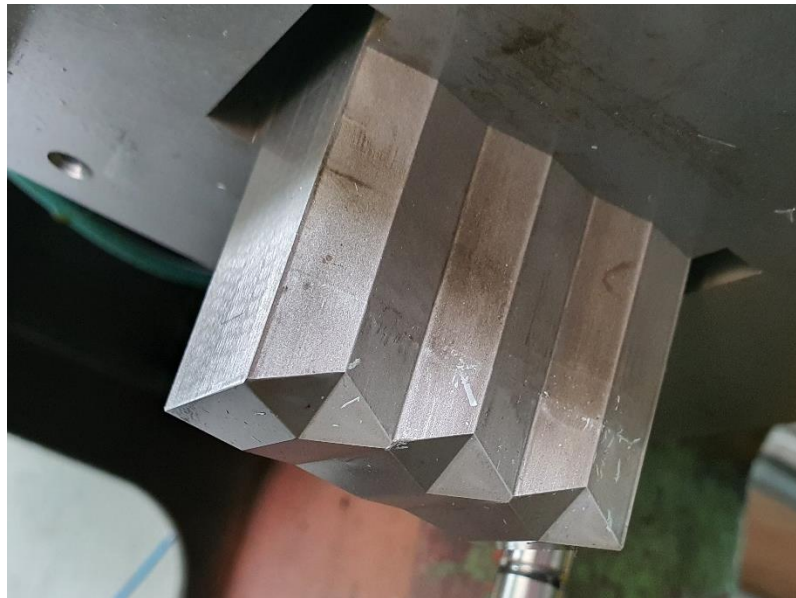


Figure 75 Punch mould for folding the origami tube from an embossed sheet

A few materials are already successfully employed for realizing crashworthy origami tubes, such as mild steel (low carbon steel) [28] [5] [61], brass [3], AM brass [39]. Furthermore, several types of aluminium alloy (6063 T3/T4/T6/T7 and EN AW-7108 T6) are used for energy-absorbing devices which make use of large plastic deformations [62]. Their employment for manufacturing lightweight origami tubes has yet to be considered.

4.1 Goals and methodology

A preliminary design exploration study is performed to understand the influence of the pattern on the overall energy absorbing performances. Four representative geometric inputs and several outputs, including performance indicators CFE and SEA, are chosen for this purpose.

In the first place, statistical methods which make use of Design of Experiments (DOEs) techniques are employed to assess the sensitivity of the desired output to the geometrical parameters and individuate the ones with a major influence on the problem. In a later step, a mathematical response surface is computed, which is capable to model the output trend for each input. Finally, an optimization is carried out to investigate the potential benefits of a new pattern.

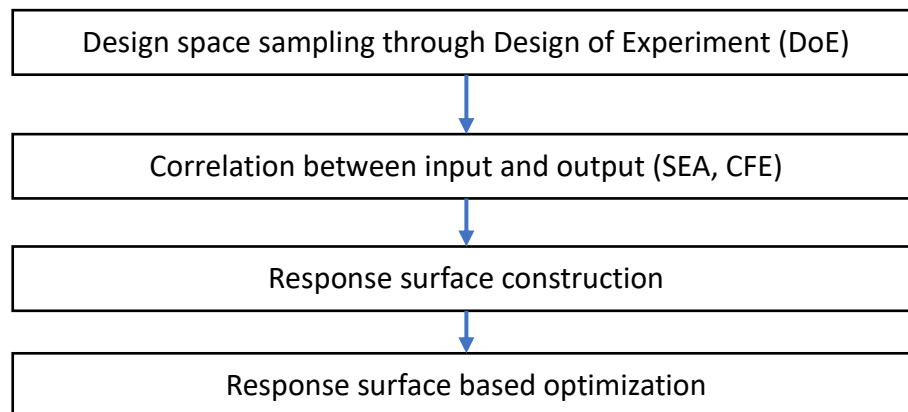


Figure 76 Design exploration schematic

The construction of statistical surfaces allows to solve the optimization problem by using a mathematical maximum seeking algorithm without extensively employing the FE model. Furthermore, the response surface construction gives an important overview on the problem, which is extremely valuable for its understanding.

The requirements which lead the optimization are chosen in accordance with the conclusions drafted in the literature review chapter. By focussing on the two main parameters SEA and CFE it is possible to consider and include effects of structure weight variation, force fluctuation, mean force, buckling force peak, and set a limit for the minimum effective crushing distance. The crushing efficiency (CFE) drops if the tube bottoms out within the simulated stroke, the mode has a high buckling force peak or high force trend fluctuation. In the same way, a heavier tube and a lower mean reaction force will reduce the energy absorption (SEA).

The present geometric optimization aims to maintain a low-cost manufacturing, hence the resulting tube is developable from a simple metal sheet, by only bending along specific folding lines. The origami congruency equations are respected, and no local thickness variations are employed for the geometry construction.

CAD software Design Modeller is used for constructing the parametric geometry while the DesignXplorer tool by ANSYS is employed for the sensitivity study and optimization.

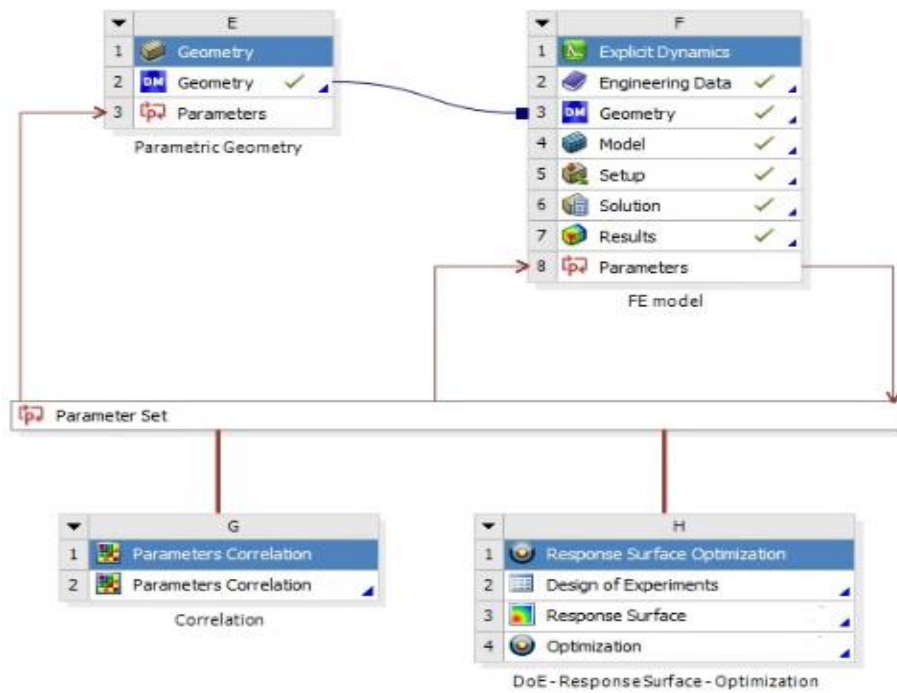


Figure 77 ANSYS Workbench tools configuration

The FE model in this study is validated against an experimental study found in literature on stamped origami tubes made in mild steel [5], with a view of employing the stamping process mentioned above for manufacturing mild steel origami samples.

Boundary conditions at the interface between tube and rigid plate are set at both sides of the origami in order to model the real application scenario in which the tube is welded to its support. Edge nodes (in contact with the plates) have translational DOFs fully constrained. This “pinned” boundary condition aims to model the lack of resistance to bending moment of the real thin-walled structure welded to the origami tube. For this preliminary investigation dynamic effects and material strain rate sensitivity are not considered, and material data are assumed from the publication mentioned above.

4.2 Correlation and model creation

4.2.1 Parametric Geometry

The three modules geometry is fully described by 29 parameters, which are dependent on 4 design parameters through the origami congruence equations written below. Only one quarter of geometry is modelled, according to the considerations in chapter 3.3.2.

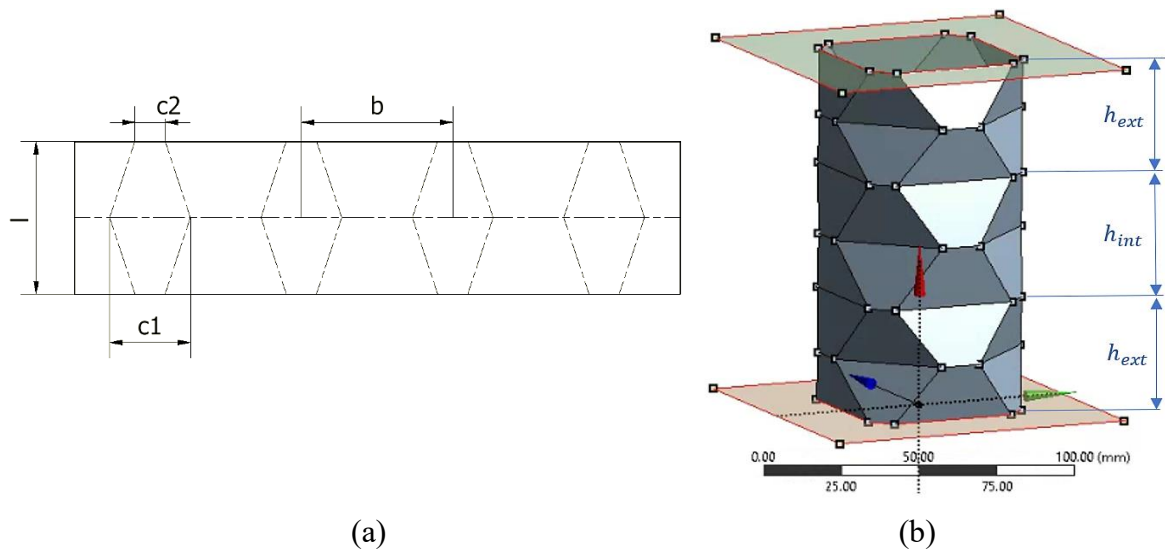


Figure 78 Parametric geometry: (a) folding lines on sheet, (b) folded origami tube

Design Parameters:

- ϑ Prefolding angle
- $\left(\frac{c_2}{c_1}\right)$ Lobe aspect ratio
- b Edge length
- $\left(\frac{h_{module\ internal}}{h_{module\ externals}}\right)$ Height ratio (resulting in prefolding variation)

Geometric constraints:

- $h_{tube} = 120\ mm$ Overall height limitation
- $M_{modules} = 3$
- $b > c_1$ Lobe geometric intersection

Origami congruence geometric relations, for each module:

$$\bullet \quad \theta = 2 \arccos \left((\sqrt{2} - 1) \left(\frac{c_2 - c_1}{l} \right) \right) \quad (17)$$

$$\bullet \quad h_{module} = l \sin \left(\frac{\theta}{2} \right) \quad (18)$$

$$\bullet \quad b_1 = b - c_1 \quad (19)$$

$$\bullet \quad b_2 = b - c_2 \quad (20)$$

Height ratio

A novel design parameter, the height ratio, is introduced in the analysis. The reason for its implementation comes from the fact that internal and external modules have different boundary conditions at their edges. External edges have fixed translational DOFs at their nodes, and therefore an increased overall stiffness. For internal modules instead, a shrinkage at the module interface section is always observed. The aim is to tune the module prefolding angle in regard to their different boundary conditions, without affecting the tube manufacturing complexity.

The origami congruence equations are rewritten for taking into account the height ratio that changes each module sheet length (l_{int} , l_{ext}) and thus its prefolding angle (θ_{int} , θ_{ext}).

$$\theta_{int,ext} = 2 \arccos \left((\sqrt{2} - 1) \left(\frac{c_1 \left(1 - \left(\frac{c_2}{c_1} \right) \right)}{l_{int,ext}} \right) \right) \quad (21)$$

$$l_{int} = \frac{h_{tube}}{\sin \left(\frac{\theta_{int}}{2} \right) \left(1 + \frac{2}{\left(\frac{h_{int}}{h_{ext}} \right)} \right)} \quad (22)$$

$$l_{ext} = \frac{h_{tube}}{\sin \left(\frac{\theta_{ext}}{2} \right) \left(2 + \left(\frac{h_{int}}{h_{ext}} \right) \right)} \quad (23)$$

Since the prefolding angle is tuned by the height ratio, the angle reported in the following pages refers to the internal module. External modules will have increased prefolding if $\left(\frac{h_{int}}{h_{ext}} \right) > 1$ and vice versa.

4.2.2 FE model

The present optimization procedure is based on the FE model utilized in chapter 3.3.2; only a few modifications are introduced:

- ❖ Mass scaling is applied to speed up the analysis, for compensating the smallest elements of the non-mapped mesh.
- ❖ Tube edges nodes DoFs are fully constrained to zero displacement, except for the axial component of the bottom edge which has a velocity constraint.
- ❖ Strain hardening is modelled through the Ludwik equation, following the procedure illustrated in chapter 3.2.3. The material strain-stress curve is available in the publication [5].
- ❖ The fully mapped Quad mesh employed in the previous study is not suitable for the parametric geometry, which can induce highly distorted mapped elements. The global meshing algorithm “Uniform MultiZone Quad/Tri method” permits a higher degree of reliability during the automated solving process. The method autonomously determines whether to create mapped or unstructured mesh. The mesh size is reduced to 1.5 mm according to the mesh sensitivity on the non-structured mesh.

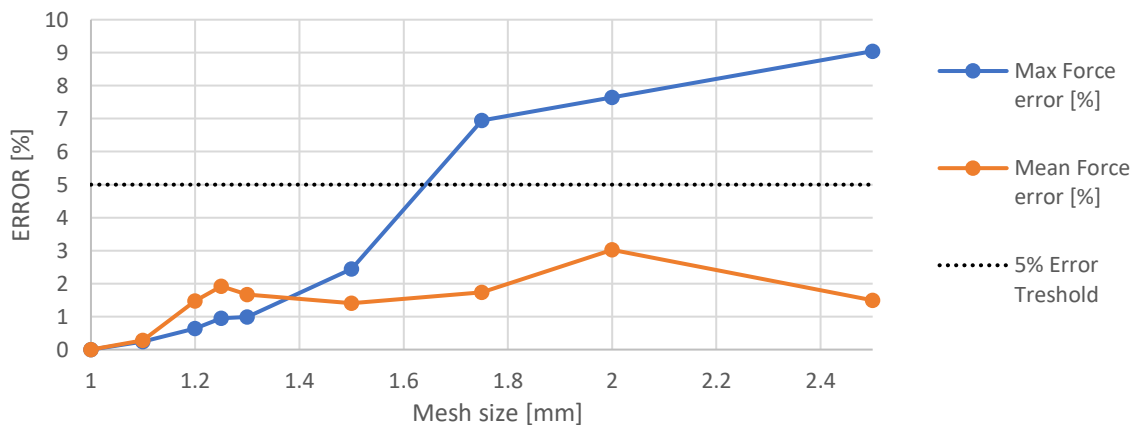


Figure 79 Mesh sensitivity non-structured mesh

The origami geometry varies consistently during the design exploration, therefore mesh and solution quality are manually checked at the extreme points of the design domain. Control outputs are also checked in every simulation for ensuring their reliability throughout the process:

- $Kinetic\ energy / Internal\ energy \leq 5\ %$
- $Energy\ error < 10\ %$
- $Total\ mass\ scaling \leq 6\ %$

Model validation

The model validation study is performed by removing the “pinned” edges constraint and applying a 0.2 friction coefficient between tube and plate, as pointed out in the publication [5].

Three different geometries are tested in order to account the real factors that can affect the behaviour. Force output from rounded and sharp-edged geometries are compared, as well as a geometry with a simulated double thickness in the overlapped region used for spot-welding the two tube halves.

A good agreement is found between the set FE model and the two experiments available in literature, with a higher general force for the numerical result. The evolution of crushing and folding from external to internal modules also proves the consistency with the experiment.

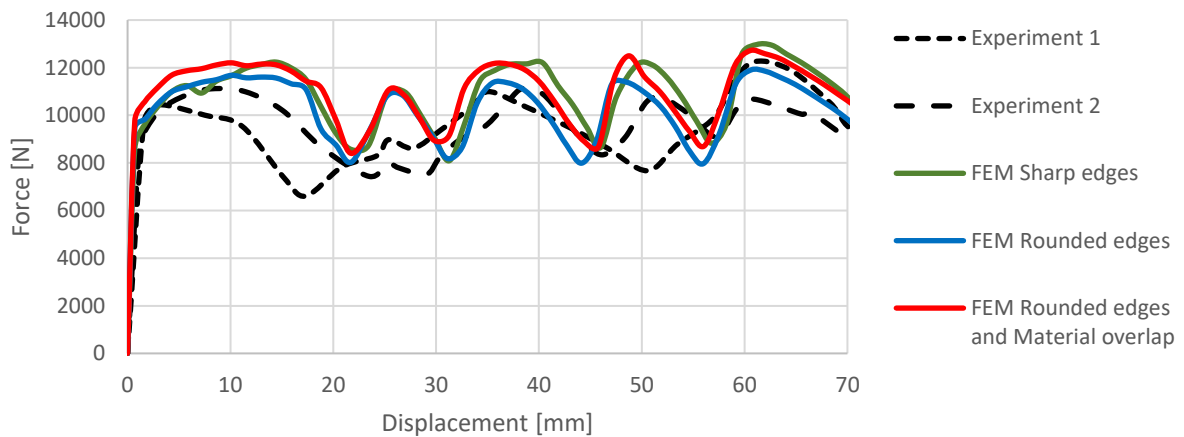


Figure 80 FEM model validation

The three cases are found comparable in force trend. Therefore, the sharp-edged geometry is used for the FE model in the following analysis, since it represents a defeatured configuration which guarantees the lowest computational time.

4.2.3 Parameter correlation

As a first approach to the optimization problem, a parameter correlation is carried out in order to better understand the influence that each independent geometrical parameter has on the outputs. This study employs the Design Exploration toolbox of ANSYS to find statistical correlations between input and output. A better insight of the sensitivity that each input parameter has on SEA and CFE allows to refine the design space where to seek the optimum solution and to evaluate the magnitude of the influence of each parameter on the solution.

The *coefficient of determination* (R^2) represents the portion of each output variation predictable from the chosen input geometric parameter [63].

$$R^2 = 1 - \frac{\sum_{i=1}^N (y_i - f_i)^2}{\sum_{i=1}^N (y_i - \bar{y})^2} \quad (24)$$

With:

y_i the output at the i sampling point

f_i the regression model at the i sampling point

\bar{y} the output mean value

N Number of sampling points

The closer the model R^2 is to 100% the more certain the output y results from the inputs. On the other hand, a low coefficient of determination implies the dependence from other factors, including noise and mesh. It can be also due to an insufficient number of sampling points.

The linear and quadratic regression models are drawn to display the dependence trend of outputs from a given input. A stop criterion based on prediction accuracy on F_{mean} and F_{max} is utilized to reduce the number of design points needed for the DoE sampling process.

The introduced method has the advantage of being relatively convenient in computational time and broad in describing the parameter behaviour. Therefore, it is employed to choose the parameters that will guide the following optimization.

Prefolding angle (ϑ)	Edge length (b)	Lobe area ratio ($\frac{c_2}{c_1}$)	Height ratio ($\frac{h_{int}}{h_{ext}}$)
150° to 170°	50 mm to 60 mm	5% to 25%	0.75 to 1.25

Table 6 Design exploration range

The correlation successfully converged to the stop criteria after 80 iterations. Sensitivity and R^2 values are reported below. The sensitivity chart summarizes correlation values (linear regression) between each input-output couple. Negative values imply inverse proportionality. It is a powerful tool to identify and visualize patterns in the given data.

	ϑ	b	c_2/c_1	h_{int}/h_{ext}
<i>Mass</i>		97%		
F_{max}	11%			18%
F_{mean}	37%			31%
$\vartheta_{Von Mises}$	8%		17%	
<i>CFE</i>	26%	47%		18%
<i>SEA</i>		97%		

Table 7 Coefficient of determination values ($R^2 \geq 5\%$ only)

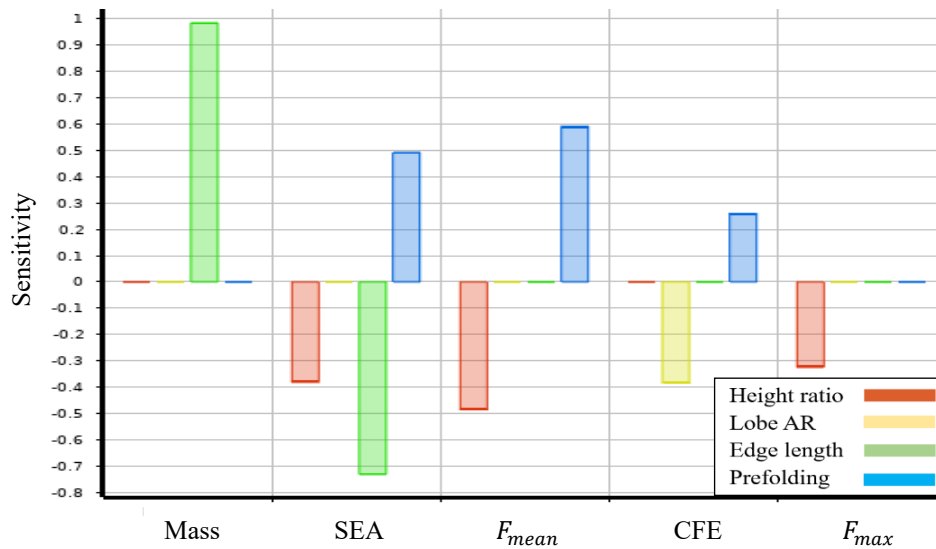


Figure 81 Sensitivity analysis

The Von Mises stress at the corner area under tension is also included among the outputs, in order to study its dependence on the pattern geometry. However, no consistent dependence is found to any of the inputs.

Prefolding Angle

Prefolding angle is the characteristic parameter this origami configuration. Higher absorption is achieved in less prefolded patterns since all tubes fall in diamond mode within the studied domain.

However, describing the trend of CFE is not trivial. By checking each simulation, it is possible to notice that highly prefolded configurations are affected by a reduction of effective crushing stroke, resulting in higher forces in the ending part of the stroke, while tubes with ϑ close to 170° are likely to trigger non-complete diamond modes and local buckling.

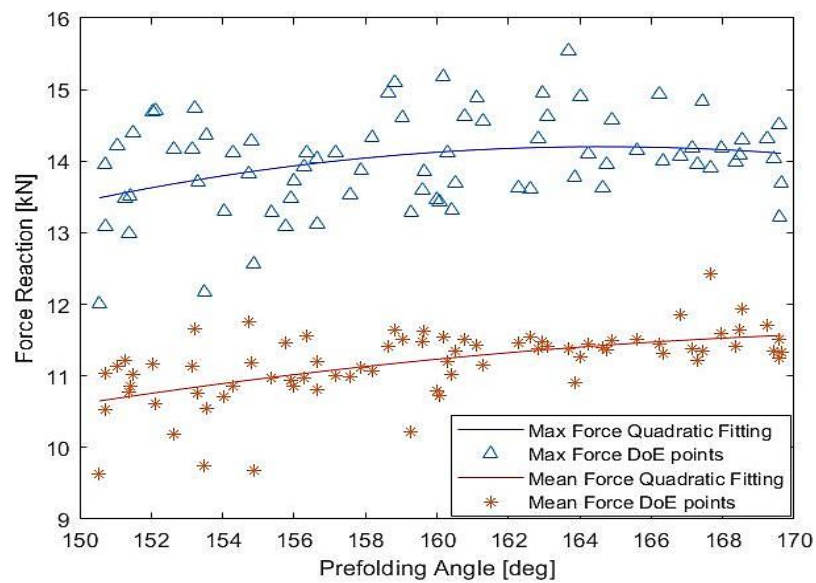


Figure 82 Prefolding angle influence on reaction force

Module height ratio

Height ratio has direct influence on external modules prefolding; thus, it must be considered as a leading parameter. A shorter central module ($h_{int}/h_{ext} < 1 \Rightarrow \vartheta_{int} < \vartheta_{ext}$) positively influences SEA. On the other hand, longer central modules have lower maximum reaction force.

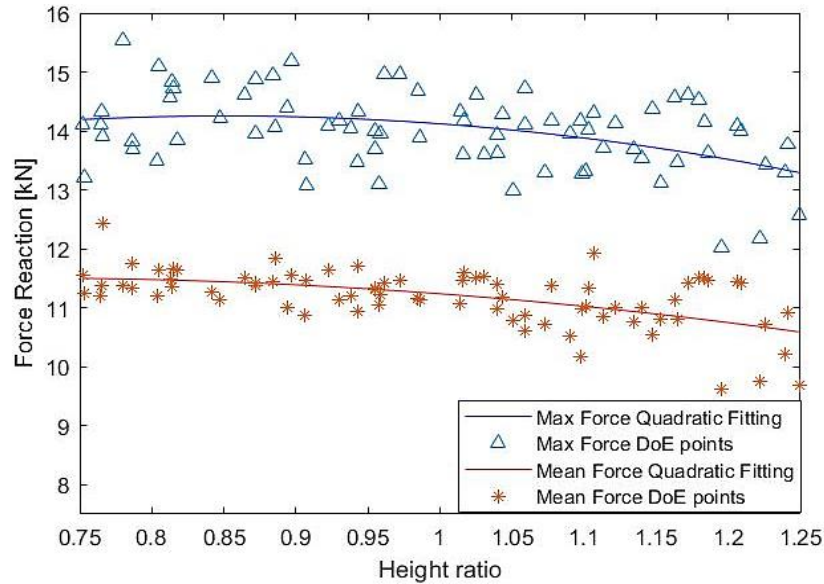


Figure 83 Height ratio influence on reaction force

Lobe aspect ratio

The parameter is found to have a minor correlation and sensitivity on the energy-absorbing performances. A diamond shaped lobe ($c_2 = 0$) appears to have better CFE than a rhomboid lobe, therefore lobe aspect ratio is removed from the set of inputs for the following step of optimization.

Edge length

The total structural mass is influenced nearly completely by the edge length, while mean and maximum reaction forces appear to have a lower sensitivity to this parameter. A low edge length advantages SEA in the selected range of values, despite the fact that it decreases the slenderness ratio of the tube, making it more susceptible to Eulerian Global Bending in case of oblique load.

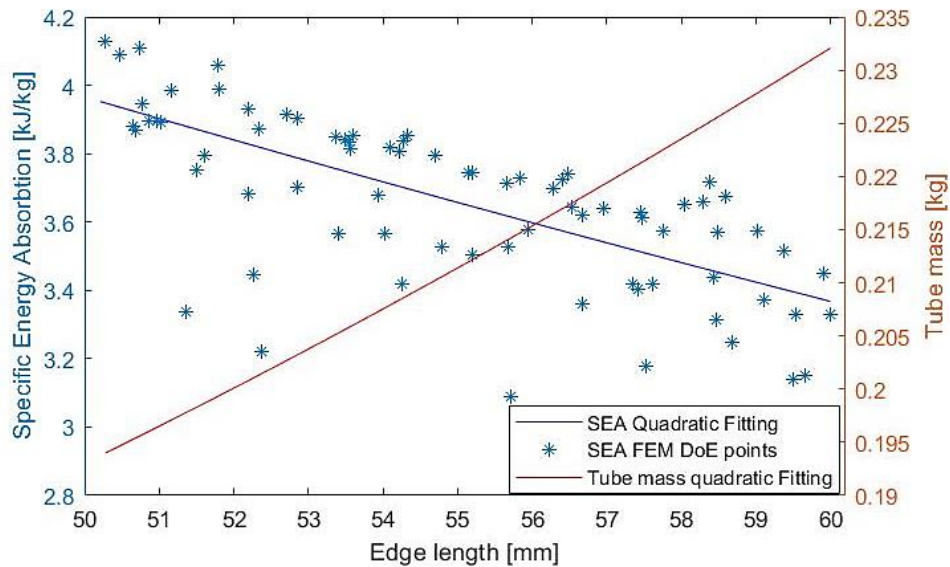


Figure 84 Edge length influence on weight and SEA

In the way it is defined, the edge length (b) does not influence the lobe geometry which is fully defined by ϑ , h_{int}/h_{ext} and c_2/c_1 . It suggests that the post-buckling stiffness is mainly driven by the lobe geometry. Equivalent plastic strain is also concentrated around lobe creases area.

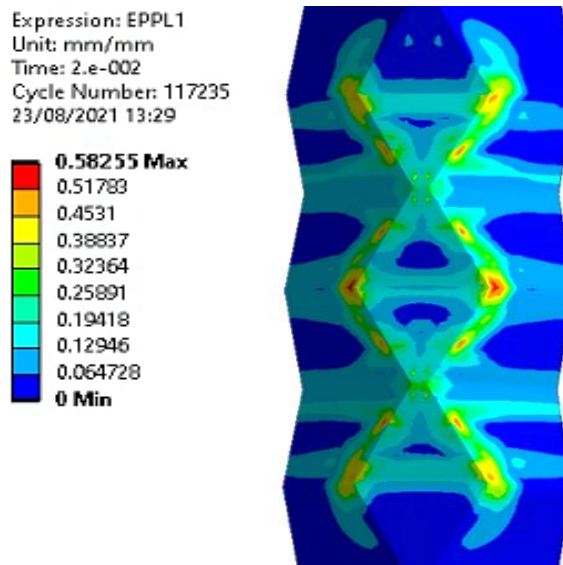


Figure 85 Equivalent Plastic Strain distribution

4.3 Optimization

The optimization procedure aims to maximise the specific energy absorption within a maximum reaction force. At the present time the force requirements for the PAV are not known, therefore the investigation is limited to investigate the advantages in terms of performances in morphing the origami pattern used for the model validation.

According to the precedent design exploration a few modifications are implemented:

- $c_2 = 2.1 \text{ mm}$ The lobe aspect ratio is removed, a $1.5 \times 45^\circ$ fillet is used instead
- $155^\circ \leq \vartheta \leq 165^\circ$ Restricted design space to avoid bottoming out and local buckling

Boundaries and geometric constraints of the optimization problem:

- $F_{max} \leq 13.75 \text{ kN}$ Maximum force reaction of the original configuration
- $b - c_1 \geq 20 \text{ mm}$ To avoid adjacent lobes interaction and leave space for welding
- $b \geq 40 \text{ mm}$ Minimum moment of inertia of the narrowest section

A slender tube due to short edges implies an increased sensitivity to bending buckling modes and a reduced structural resistance to bending moments. The side edges minimum value has to be assessed in accordance with structural requirements which not available at this time, thus its minimum value is set to 1/3 of the total tube height.

Response surfaces

The resulting response surface is locally refined, in order to reduce the estimated error of the response surface, until 0.3 kN and 13 J (0.2 kN of mean force) of maximum force reaction and energy absorption respectively. The output geometry of the optimization is directly simulated though FE analysis with and without symmetry conditions, in order to verify the initial assumption of purely axial crushing.

Few representative response surfaces are presented, in order to visualise the overall trend under the input height ratio vs prefolding and edge length vs prefolding. The surfaces display strong nonlinearities in few localised areas.

As already observed during the correlation analysis; prefolding angle and edge length have a direct dependence on maximum and mean force reaction, while height ratio has an inverse trend. On the contrary, crushing efficiency has plateaus for low prefolding angles and high height ratio.

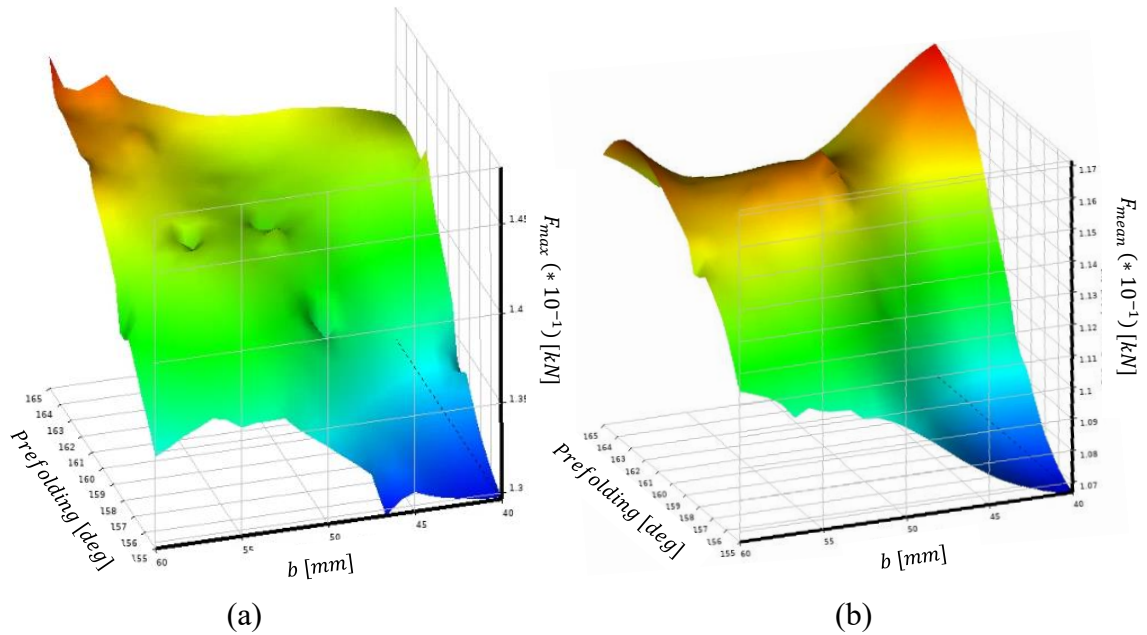


Figure 86 Response surfaces input ϑ - b for output: (a) max force, (b) mean force

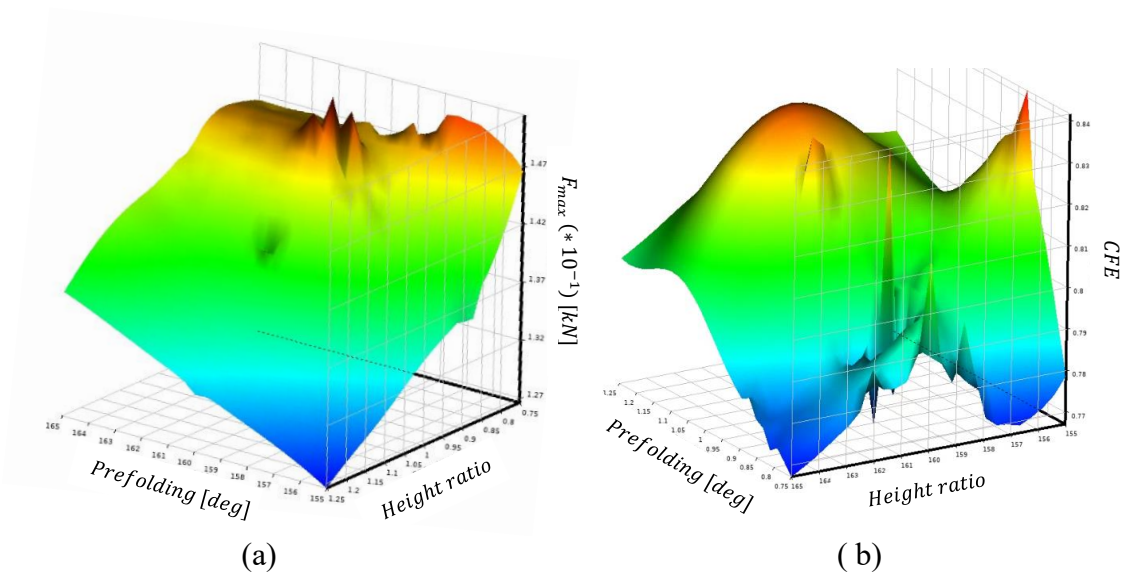
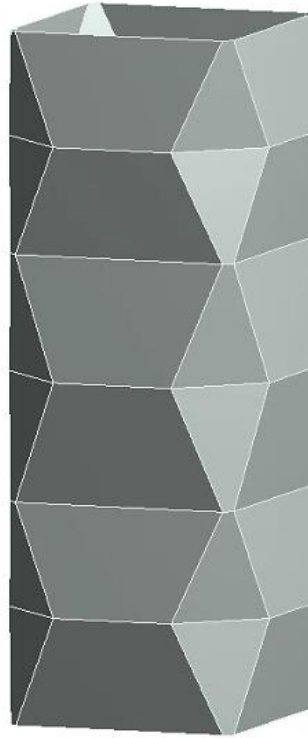


Figure 87 Response surfaces input ϑ -height ratio for output: (a) max force, (b) CFE

Optimized geometry

The optimized geometry (rounded to feasible values) is presented along with its force trend. Its smaller cross section drastically reduces to tube mass, while its post-buckling stiffness is compensated by a lower prefolding of the pattern.



Prefolding angle (ϑ)	Edge length (b)	Height ratio ($\frac{h_{int}}{h_{ext}}$)
162°	40 mm	1.11

Figure 88 Optimised geometry

	<i>Mass</i> [g]	F_{max} [kN]	F_{mean} [kN]	<i>CFE</i> [%]	<i>SEA</i> [kJ/kg]
Reference	232.3 g	13.76	10.97	79.8 %	3.271
Optimized	153.6 g	13.01	11.01	84.7 %	4.963
Difference [%]	↓↓ 34 %	↓ 5.4 %	≈	↑ 4.9 %	↑↑ 51.7 %

Table 8 Optimised origami performances

The comparison between reference and optimised origami tube is showed in the following figure. Furthermore, the hypothesis of pure axial folding is validated through a full-model analysis which shows an almost identical force-displacement trend. The small difference at the end of the crushing stroke, characterized by strong nonlinearities, does not significantly influence any crushing performance indicator.

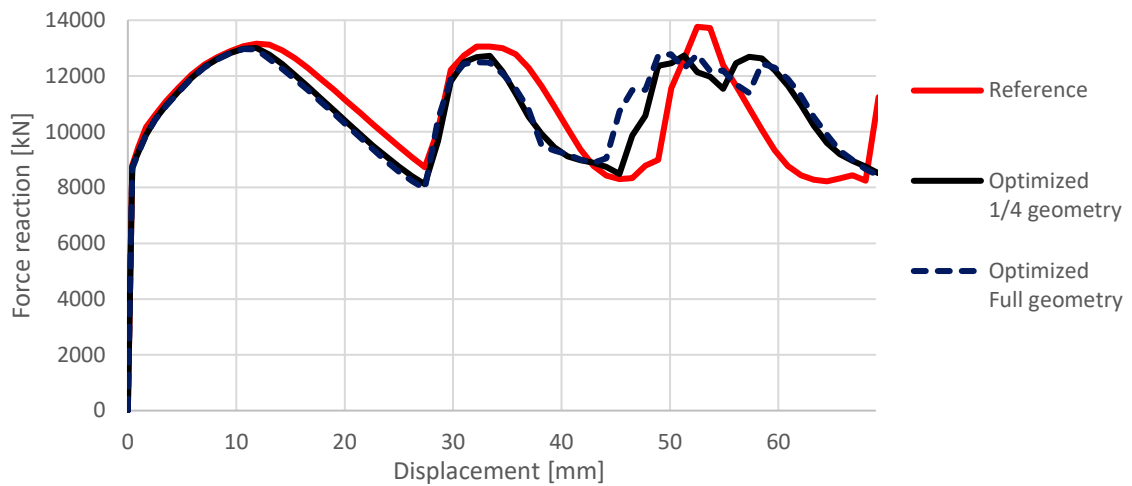


Figure 89 Optimized vs reference geometry force - displacement trend and validation

The stiffness is maintained at almost the same level as the reference geometry. A further beneficial effect is the longer effective crushing stroke before bottoming out. It results from a more compliant behaviour of external modules, due to their lower prefolding angle ($h_{\text{int}}/h_{\text{ext}} > 1$).

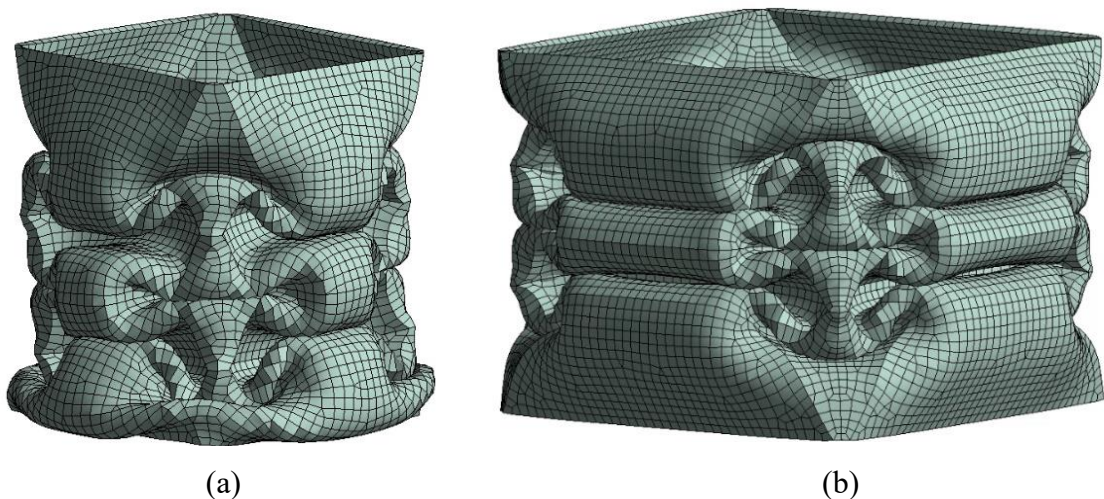


Figure 90 Crushed origami tubes (70 mm stroke): (a) optimized, (b) reference geometry

Dynamic analysis

Finally, the optimized and reference tubes are evaluated in a dynamic case. This study is fundamental to validate the quasi-static approach utilised for the optimization, by evaluating the influence of inertia and strain rate on mode induction.

The full-geometry FE model employed for the previous optimization is modified in two points:

- A constant crushing velocity of 9.1 m/s is set, according to the EASA CS-27.561/.562 regulation [4].
- Strain rate dependency is accounted through the Cowper-Symonds material model. Strain rate exponent q and strain rate coefficient D are assumed as 5 and 40.4 s respectively, from a previous study on dynamic crushing of mild steel tubes [10].

As a result, no differences are observed in both geometries between dynamic and quasi-static case in terms of buckling mode and final crushed shape. A mayor difference is played by strain rate hardening, which results in a higher energy absorption and peak force in the first part of crushing.

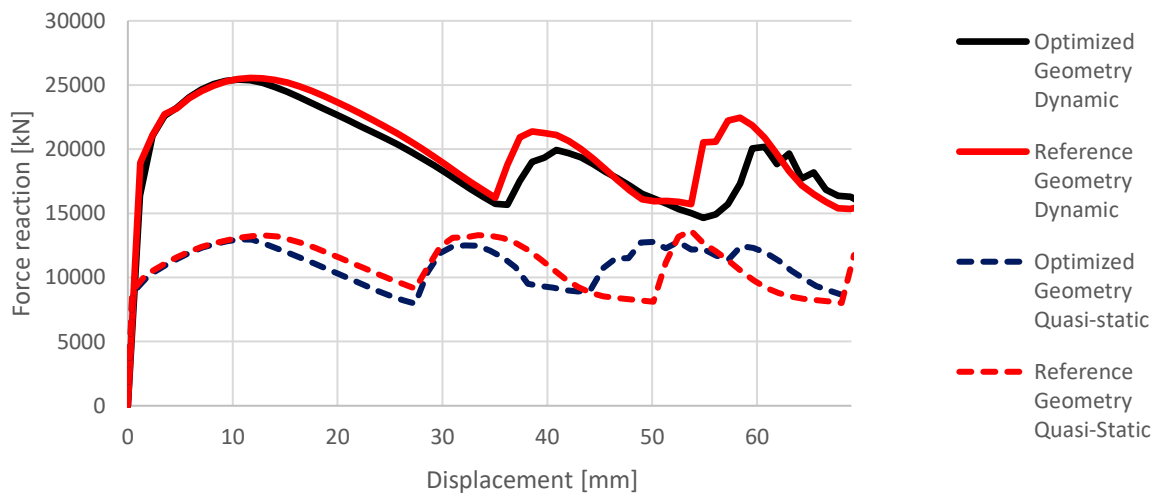


Figure 91 Comparison between dynamic and quasi-static cases

The results are in accordance with the experimental investigations from C. Zhou and B. Wang on a geometry equivalent to the “reference geometry” utilised in this study. The publications show an increment of 108 % and 85.5 % in maximum and mean force value respectively, when comparing the dynamic case (T26 case) [6] to the quasi-static one (B3_1) [5].

Strain rate, and the consequent hardening is found to be evenly distributed in the modules which are folding. In addition, lobe edges experience higher hardening during the first crushing stage. The following figure displays the qualitative distribution of strain rate.

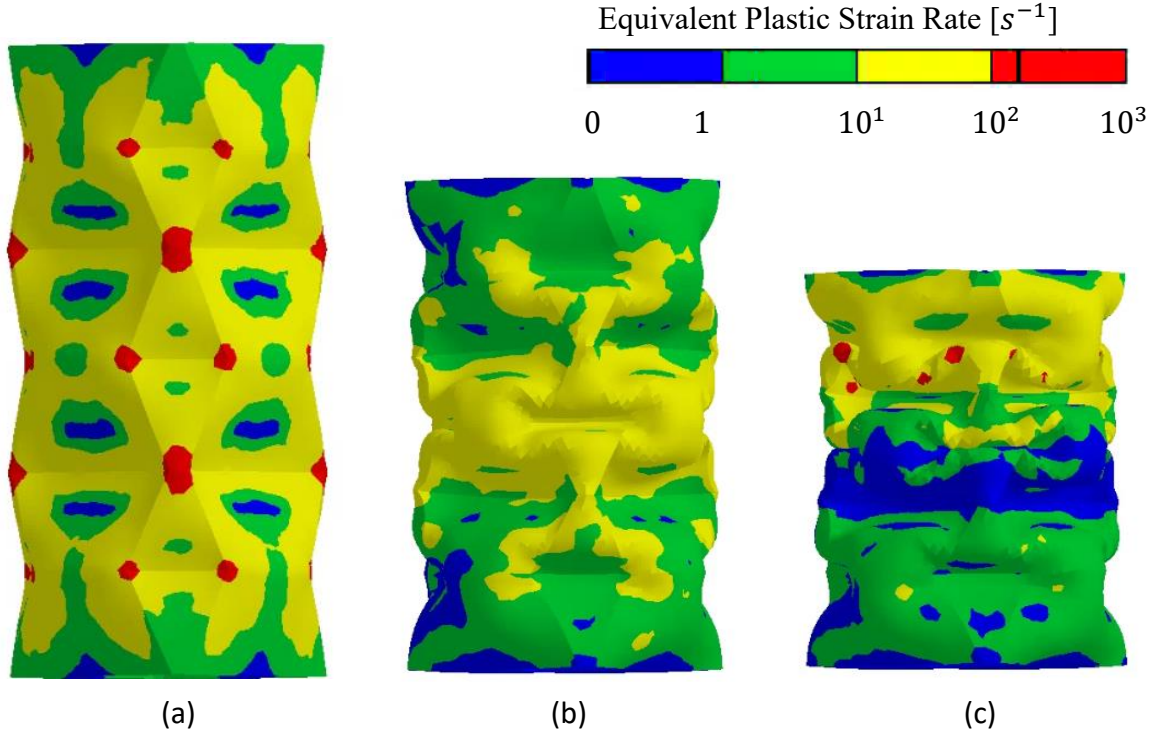


Figure 92 Strain rate distribution at different stroke: (a) 8 mm, (b) 30 mm, (c) 50 mm

A logarithmic scale is chosen for better representing the strain rate field, according to the Cowper-Symonds model. The dependency between material strength increment and strain rate is reported in the following equation.

$$\frac{\sigma_{\text{Cowper-Symonds}}}{\sigma_{\text{Ludwik}}} = 1 + \left(\frac{\dot{\epsilon}}{40.4}\right)^{\frac{1}{5}} \propto \sqrt[5]{\dot{\epsilon}} \quad (25)$$

In conclusion, the initial assumption of progressive buckling mode is confirmed for both numerical simulations (reference and optimized). At 9.1 m/s, inertia effects do not introduce any detectable difference in the way the origami-patterned tube buckles. However, strain rate effects can heavily affect CFE and increase the maximum reaction force, which represents a main issue for crashworthiness application since it can exceed the survivable force limits. A further optimization cycle needs to be run considering the dynamic loading and the subsequent material strain hardening.

Conclusions

All manned vehicles must be designed to limit accelerations on the occupants in the event of crash, therefore a crashworthy design has become a main requirement. Therefore, a device capable to reduce the magnitude of acceleration acting on the human body is fundamental.

The origami patterned crash box is a thin-walled energy-absorber which dissipates energy through its plastic deformation. Its prefolded origami pattern is designed to trigger the high SEA diamond mode and to act as induced geometrical imperfection to flatten the initial buckling force and achieve high CFE and mode predictability.

Crashworthiness characteristics of the origami-patterned tube are analysed in the current dissertation, as an initial study aimed at its employment as energy-absorber component on a Personal Air Vehicle (PAV).

Two approaches are adopted in this thesis. At first, a series of quasi-static crushing tests are performed on origami tubes with different materials and geometrical features. Metal Additive Manufacturing is individuated as a cost-efficient method to produce a small batch of complex specimen and to have possibility of conveniently printing different geometries. Two additive materials are chosen, AlSi10Mg aluminium alloy and SUS316L stainless steel. Finite Element analysis (FEM) and Direct Image Correlation (DIC) are employed for a better insight on the crushing behaviour.

The aluminium origami reveals a brittle behaviour which results in a collapsing mode fully dominated by crack propagation. Its energy-absorbing performances drops as a consequence of several fractures originated during the initial elastic slope. The stainless steel origami, which has excellent mechanical properties in terms of strength and elongation, also exhibits localised fractures at lobe corners under tension.

A second geometry with lower wall-thickness and rounded edges is numerically studied to overcome the issue due to tensile stress localization, by enlarging the area undergoing deformation around the plastic hinge. Eventually, also this geometry shows cracking although in a much lower extent, as a result the tube stiffness is partially preserved. Influence of wall-thickness and edge rounding are examined at this phase; FE analysis indicate that higher wall-thickness is beneficial for SEA and CFE, while the influence of a round fillet influences the overall performance in a lesser extent.

Furthermore, the equivalent stress at the cracking point obtained from the FEM is lower than the estimated true ultimate tensile stress. This can attribute to the shell elements used for discretizing the geometry that do not account the stress component in thickness direction. Deformation though the thickness at the cracking point is instead clearly noticeable in the experiments. The chosen AM process imposes limitations in terms of materials and minimum wall-thickness, which do not allow to proceed further with the investigation. Furthermore, despite the accurate geometric tolerances, AM samples have material properties highly dependent on their printing process, which introduce an inevitable uncertainty factor in the tube modelling.

Secondly, a numerical design exploration study is executed with the aim of assessing the sensitivity of origami pattern features over the energy-absorption. Potential benefits of a new pattern are investigated through geometrical optimization, and consequently, an improved geometry is proposed. The correlation and optimization output suggest that the tube axial stiffness in post-buckling regime is highly dependent on the lobe's geometry rather than on the side edge length. Also, most of the plastic deformation is concentrated around the pattern creases.

For the explicit FE model, a previous experimental work was adopted for validation, while a stamping method based on embossing and folding is currently under development at the hosting university. The present optimization procedure can be tailored to the PAV case, once structural and crashworthiness requirements will be available in a later stage of its design.

Crashworthiness performances and proper mode induction must be validated also under dynamic load, since the application as a crash box involves both inertia and strain rate sensitivity. The material model used in this thesis is conceived for the implementation of strain rate dependency through the Cowper-Symonds equation.

A numerical dynamic case is eventually performed, qualitatively accounting the EASA CS-27 velocity range. No influence of inertia is found in the way the tube buckles. However, the material hardening due to strain rate sharply increases the tube force reaction. It imposes the need of a deeper investigation on the dynamic case, in order to satisfy the crashworthiness requirements in terms of maximum force.

Additionally, the assumption of constrained translational DOFs at the tube edges has to be checked when more information about the PAV assembly will be available.

The origami pattern offers a wide design space in which SEA and CFE can be enhanced, by reducing post-buckling force fluctuation and tube weight. Prefolding angle and its distribution due to height ratio are found to be influent on the resulting reaction force as well as edge length, which, at the same time, is directly correlated with the tube weight.

An endless number of configurations can be generated from a metal sheet, introducing new geometrical parameters, such as for tapered, polygonal or rectangular tubes. Findings of this numerical study indicate that a topological optimization of the metal sheet could potentially improve the specific absorption, since plastic deformation and stresses appear to be localized in specific regions. Material can be removed from areas with less contribution to the tube post-buckling stiffness.

References

- [1] X. e. a. Yang, “Crashworthy design and energy absorption mechanisms for helicopter structures: A systematic literature review,” *Progress in Aerospace Sciences* , vol. 114, 2020.
- [2] Y. Z. a. B. W. C. Zhou, “Crashworthiness design for trapezoid origami crash boxes,” vol. 117, no. 257-267, 2017.
- [3] H. D. M. S. L. Y. Y. C. a. Z. Y. J. Ma, “Quasi-static axial crushing of hexagonal origami crash boxes as energy absorption devices,” vol. 10(1), no. 133-143, 2019.
- [4] EASA, “Workshop 2 website: <https://nari.arc.nasa.gov/crashworthiness>,” 2020.
- [5] B. W. e. a. C. H. Zhou, “Quasi-static axial compression of origami crash boxes,” *International Journal of Applied Mechanics*, vol. 9(5), 2017.
- [6] B. W. J. M. a. Z. Y. C. Zhou, “Dynamic axial crushing of origami crash boxes,” Vols. 118, 1-12, 2016.
- [7] J. Ma, “Thin-walled tubes with pre-folded origami patterns as energy absorption devices,” 2011.
- [8] L. e. a. Yuan, “Quasi-static impact of origami crash boxes with various profiles,” vol. 141, no. 435-446, 2019.
- [9] B. W. a. C. Zhou, “The imperfection-sensitivity of origami crash boxes,” *International Journal of Mechanical Sciences*, Vols. 121, 58-66, 2017.
- [10] L. J. K. X. B. a. B. W. C. Zhou, “Origami crash boxes subjected to dynamic oblique loading,” vol. 84(9), 2017.
- [11] P. a. Z. a. M. a. B. Astori, “Validation of Numerical Models of a Rotorcraft Crashworthy Seat and Subfloor,” *Aerospace*, Vols. 7(12), 174, p. 174, 2020.
- [12] W. e. a. Gao, “Crash Energy-Absorption Structure Design Based on an Innovated Lightweight Technology,” 2017.
- [13] A. Alghamdi, “Collapsible impact Energy absorbers. An overview.,” *Thin-Walled Structures*, Vols. 39(2), 189-213, pp. 189-213, 2001.
- [14] E. A. S. Agency, “EASA CS 27 Certification Specifications for Small Rotorcraft, Amendment 7,” 2020.
- [15] D. Hu, J. Yang and M. Hu, “Full-Scale Vertical Drop Test and Numerical Simulation of a Crashworthy Helicopter Seat/Occupant System.,” Vols. 14, 565–583, 2009.
- [16] S. P. Desjardins, “The evolution of energy absorption systems for crashworthy helicopter seats,” vol. 51.2, no. 150-163, 2006.
- [17] B. C., “Crashworthiness of helicopter subfloor structures. *International Journal of Impact Engineering*,” vol. 27(10), no. 1067-1082, 2002.
- [18] F. M. B. M. M. B. M. Guida, “Innovative anti crash absorber for a crashworthy landing gear,” vol. 21, no. 483–494, 2014.
- [19] G. J. Alessandro Airoidi, “A design solution for a crashworthy landing gear with a new triggering mechanism for the plastic collapse of metallic tubes,” Vols. 9 (5), 445-455, 2005.
- [20] Nasaspaceflight images, [Online]. Available: <https://forum.nasaspaceflight.com/index.php?PHPSESSID=5siq0n9q92ueietih1jid70vje&action=dlattach;topic=51332.0;attach=1969821;image>.

- [21] UNECE, “Regulation No. 94,” 2007.
- [22] A. M. S. a. A.-G. O. Baroutaji, “On the crashworthiness performance of thin-walled energy absorbers: recent advances and future developments,” *Thin-Walled Structures*, Vols. 118, 137-163, 2017.
- [23] G. L. a. R. H. G. S. R. Guillow, “Quasi-static axial compression of thinwalled circular aluminium tubes,” vol. 43 (9), no. 2103–2123, 2001.
- [24] G. a. Y. T. X. Lu, *Energy absorption of structures and materials*, 2003.
- [25] F. C. a. S. K. Bardi, “Plastic buckling of circular tubes under axial compression - part I: experiments,” *International journal of mechanical sciences*, Vols. 48.8, 830-841, 2006.
- [26] Q. A.-H. S. T. S. a. S. P. D. Meng, “Axial crushing of square tubes,” Vols. 25(9-10), no. 747-773, 1983.
- [27] S. e. a. Ming, “Energy absorption of thin-walled square tubes designed by kirigami approach,” vol. 157, no. 150-164, 2019.
- [28] J. a. Z. Y. Ma, “Energy absorption of thin-walled square tubes with a prefolded origami pattern—part I: geometry and numerical simulation,” vol. 81(1), 2014.
- [29] W. H. a. S. C. D. Horton, “Imperfections, a main contributor to scatter in experimental values of buckling load,” vol. 1(1), no. 59-72, 1965.
- [30] A. G. M. D. E. B. A. K. a. V. G. L. Mamalis, “Energy dissipation and associated failure modes when axially loading polygonal thin-walled cylinders,” vol. 12(1), no. 17-34, 1991.
- [31] M. M. G. a. Y. S. Yamashita, “Axial crush of hollow cylindrical structures with various polygonal cross-sections: Numerical simulation and experiment,” *Journal of Materials Processing Technology*, Vols. 140(1-3), pp. 59-64, 2003.
- [32] D. C. a. S. H. P. Han, “Collapse behavior of square thin-walled columns subjected to oblique loads,” *Thin-Walled Structures*, vol. 35(3), pp. 167-184, 1999.
- [33] X. a. H. Z. Zhang, “Relative merits of conical tubes with graded thickness subjected to oblique impact loads,” vol. 98, no. 111-125, 2005.
- [34] A. A. a. E.-S. H. Singace, “Behaviour of axially crushed corrugated tubes,” vol. 39(3), no. 249-268, 1997.
- [35] W. a. N. J. Abramowicz, “Dynamic axial crushing of square tubes,” *International Journal of Impact Engineering*, vol. 2(2), pp. 179-208, 1984.
- [36] T. a. A. W. (. Wierzbicki, “On the crushing mechanics of thin-walled structures,” vol. 50(4), no. 727-734, 1983.
- [37] Z. S. T. L. K. D. C. Z. a. B. W. S. Ming, “The energy absorption of thin-walled tubes designed by origami approach applied to the ends,” vol. 192, 2020.
- [38] Y. C. G. L. J. Song, “ Axial crushing of thin-walled structures with origami patterns,” Vols. 54, 65–71, 2012.
- [39] K. e. a. Yang, “Energy absorption of thin-walled tubes with pre-folded origami patterns: Numerical simulation and experimental verification,” Vols. 103, 33-44, 2016.
- [40] A. B. e. a. Spierings, “Production of functional parts using SLM—Opportunities and limitations,” *5th International Conference on Advanced Research in Virtual and Rapid Prototyping* , pp. 785-790, 2011.
- [41] A. Y. Hussein, “The Development of Lightweight Cellular Structures for Metal Additive Manufacturing,” *Doctoral dissertation*, 2013.
- [42] L. e. a. Jiao, “Femtosecond laser produced hydrophobic hierarchical structures on

- additive manufacturing parts,” *Nanomaterials*, Vols. 8.8, 601, 2018.
- [43] “ANSYS Explicit Dynamics Analysis Guide,” 2020.
- [44] A. a. U. S. Söderberg, “Modelling of strain hardening and strain rate hardening of dual phase steels in finite element analysis of energy-absorbing components,” vol. 69, 2005.
- [45] M. a. D. W. J. Murugesan, “Johnson Cook material and failure model parameters estimation of AISI-1045 medium carbon steel for metal forming applications,” vol. 12(4), 2019.
- [46] EOS, “Material data sheet Flexline StainlessSteel 316L M400-4”.
- [47] EOS, “Material data sheet Aluminium AlSi10Mg”.
- [48] I. A. S. a. N. F. Rosenthal, “Strain rate sensitivity and fracture mechanism of AlSi10Mg parts produced by selective laser melting,” *Materials Science and Engineering*, vol. 682, pp. 509-517, 2017.
- [49] A. M. L. a. O. S. H. Reyes, “Crashworthiness of aluminum extrusions subjected to oblique loading: experiments and numerical analyses,” *International Journal of Mechanical Sciences*, vol. 44(9), pp. 1965-1984, 2002.
- [50] D. e. a. Gu, “Selective laser melting additive manufacturing of TiC/AlSi10Mg bulk-form nanocomposites with tailored microstructures and properties,” Vols. 56, 108-116, 2014.
- [51] M. e. a. Costas, “Testing and simulation of additively manufactured AlSi10Mg components under quasi-static loading,” vol. 81, 2020.
- [52] “Getting Started with ABAQUS/Explicit, v6.6”.
- [53] ABAQUS, “<https://abaqus-docs.mit.edu/2017/English/SIMACAEELMRefMap/simaelm-c-shelloverview.htm>”.
- [54] T. J. I. L. a. T. C.-S. Belytschko, “Explicit algorithms for the nonlinear dynamics of shells,” *Computer methods in applied mechanics and engineering*, Vols. 42(2), 225-251, 1984.
- [55] T. H. S. a. N. C. Belytschko, “A C0 triangular plate element with one-point quadrature,” *International Journal for Numerical Methods in Engineering*, Vols. 20(5), 787-802, 1984.
- [56] ABAQUS, “<https://abaqus-docs.mit.edu/2017/English/SIMACAEGSARefMap/simagsa-c-ctmreduced.htm>”.
- [57] D. P. a. T. B. Flanagan, “A uniform strain hexahedron and quadrilateral with orthogonal hourglass control,” Vols. 17(5), 679-706., 1981.
- [58] W. a. J. N. Abramowicz, “Transition From Initial Global Bending to Progressive Buckling of Tubes Loaded Statically and Dynamically,” Vols. 19(5–6), 415–437, 1997.
- [59] “ANSYS Meshing user's guide, release 13.0,” 2010.
- [60] D. F. e. a. Susan, “The Effects of Annealing Treatments on AM 316L Stainless Steel,” *Sandia National Lab*, 2018.
- [61] M. a. G. B. Boreanaz, “Master's thesis Development of crash box for automotive application,” 2018.
- [62] J. A. V. A. D. a. A. K. Marzbanrad, “A Numerical and experimental study on the crash behavior of the extruded aluminum crash box with elastic support,” *Latin American Journal of Solids and Structures*, vol. 11, pp. 1329-1348, 2014.
- [63] “ANSYS DesignXplorer User's Guide,” 2021.

List of figures

Figure 1 Typical car frontal bumper assembly configuration [12]	1
Figure 2 Qualitative thin-walled structure crushing behaviour	2
Figure 3 Crashworthy seat energy absorbing devices [16].....	4
Figure 4 Helicopter subfloor layout [11]	4
Figure 5 SpaceX Starship SN6 energy absorbers [20]	5
Figure 6 Origami patterned tube: (a) 2D folding lines on metal sheet, (b) folded tube	7
Figure 7 Cylindrical tube buckling modes: (a) Concertina, (b) Diamond [25]	9
Figure 8 Squared tube buckling modes: (a) symmetric, (b) extensional, (c-d) asymmetric [27]	10
Figure 9 Deformed shape and specific mean force of polygons, with different number of edges and wall-thickness [31].....	11
Figure 10 Mean force under oblique load for squared tubes [32]	12
Figure 11 Tube patterns: (a) Corrugated tube, (b) Grooved tube, (c) Dented tube [7].....	13
Figure 12 Single module origami: first crushing stage [37].....	16
Figure 13 Basic folding element crushing phases: (a) stage I, (b) stage II [3].....	16
Figure 14 Hexagonal origami module: (a) folded tube, (b) folding lines on sheet [3].....	17
Figure 15 Trapezoidal lobes origami pattern	18
Figure 16 Effects of prefolding angle on mode stability and mean force [37].....	18
Figure 17 Influence of number of modules on mean force [7].....	19
Figure 18 Area ratio influence on origami force output and stability [2].....	20
Figure 19 Example origami tube manufacturing process [5] [6].....	21
Figure 20 Crushing of origami patterned 3D printed brass tube [39]	22
Figure 21 End-origami: (a) origami pattern, (b) lobe developing during crushing	22
Figure 22 Local buckling in lobe intersection (quarter of tube FE model) [2]	23
Figure 23 Crushed cross-sections modes: (a) diamond, (b) local, (c) symmetric [6].....	24
Figure 24 Tapered origami tube: (a) 2D folding lines on metal sheet, (b) folded tube [7].....	25
Figure 25 Manufacturing imperfection capable to trigger symmetric mode [9]	25
Figure 26 Crushing force trend in quasi-static [5] and dynamic case [6].....	27
Figure 27 Bulkhead stiffener [9]	27
Figure 28 Nominal surface geometry	29
Figure 29 Schematic illustration of powder bed SLM process [42].....	30
Figure 30 Printing configuration	31
Figure 31 Edge rounding in the 3D printed origami tube	31
Figure 32 Lobe intersection bevel	33
Figure 33 Stress strain 3D printed origami along two printing directions	35
Figure 34 Modelled isotropic strain hardening SUS316L material	36
Figure 35 Specimens surface roughness: (a) AlSi10Mg, (b) SUS316L	38
Figure 36 Strain rate field from DIC data.....	39
Figure 37 Experimental setup.....	40
Figure 38 Predicted noise level in DIC analysis.....	41
Figure 39 Explicit and Implicit FEM applications [43]	42
Figure 40 Free body diagram of stress wave propagation [52]	43
Figure 41 Quadrilateral element with 3 integration points through the thickness [43].....	46
Figure 42 Hourglass deformation mode [56]	47
Figure 43 Contact detection by trajectory method [43].....	48
Figure 44 Quarter of model FE geometry and boundary conditions.....	49
Figure 45 Buckling mode map for squared tubes: (a) Quasi static, (b) Dynamic [58]	50
Figure 46 Non-mapped mesh problems: (a) element distortion, (b) energy error.....	51

Figure 47 Time increment plot: (a) Non-mapped mesh, (b) Fully Quad mapped mesh.....	51
Figure 48 Mesh sensitivity – Mapped mesh.....	52
Figure 49 Meshed tube	53
Figure 50 Mesh characteristic parameters illustration [59]	54
Figure 51 Timestep sensitivity.....	55
Figure 52 Cylindrical tube Force – Displacement curve.....	56
Figure 53 Natural 3 lobes diamond mode	56
Figure 54 Straight tube strain rate distribution.....	57
Figure 55 AlSi10Mg specimen fractures	57
Figure 56 DIC axial strain: (a) pre-fracture, (b) post-fracture.....	58
Figure 57 SUS316L 1.5 mm thick origami Force – Displacement curve	59
Figure 58 Fracture initiation points	60
Figure 59 Partially crushed second module.....	60
Figure 60 Principal strain field components: (a) 1 st tensile, (b) 2 nd compressive.....	61
Figure 61 Comparison between as-built and annealed SUS316L origami.....	62
Figure 62 SUS316L 1 mm thick origami Force – Displacement curve	63
Figure 63 Lobe geometry before cracking: (a) 1.5 mm thick, (b) 1 mm thick rounded.....	63
Figure 64 Crack developed on one side.....	64
Figure 65 Comparison between numerical and experiment force reaction	65
Figure 66 Strain hardening curves for yield stress sensitivity.....	66
Figure 67 Sensitivity to yield stress variation	66
Figure 68 Sensitivity to elastic module variation	67
Figure 69 FEM Von-Mises stress, 1.5 wall thickness at 15mm stroke.....	67
Figure 70 Sensitivity to tube wall-thickness variation	68
Figure 71 Lobe deformation: (a) 1.5 mm wall thickness, (b) 1 mm wall thickness.....	68
Figure 72 FEM Von-Mises stress, 1 wall thickness at 15mm stroke.....	69
Figure 73 Sensitivity to pattern creases fillet radius variation	70
Figure 74 Lobe deformation of 1 mm thick origami: (a) sharp edges, (b) rounded edges.....	70
Figure 75 Punch mould for folding the origami tube from an embossed sheet.....	73
Figure 76 Design exploration schematic	74
Figure 77 ANSYS Workbench tools configuration	75
Figure 78 Parametric geometry: (a) folding lines on sheet, (b) folded origami tube	76
Figure 79 Mesh sensitivity non-structured mesh.....	78
Figure 80 FEM model validation	79
Figure 81 Sensitivity analysis.....	81
Figure 82 Prefolding angle influence on reaction force	82
Figure 83 Height ratio influence on reaction force.....	83
Figure 84 Edge length influence on weight and SEA	84
Figure 85 Equivalent Plastic Strain distribution.....	84
Figure 86 Response surfaces input θ -b for output: (a) max force, (b) mean force	86
Figure 87 Response surfaces input θ -height ratio for output: (a) max force, (b) CFE.....	86
Figure 88 Optimised geometry	87
Figure 89 Optimized vs reference geometry force - displacement trend and validation.....	88
Figure 90 Crushed origami tubes (70 mm stroke): (a) optimized, (b) reference geometry.....	88
Figure 91 Comparison between dynamic and quasi-static cases.....	89
Figure 92 Strain rate distribution at different stroke: (a) 8 mm, (b) 30 mm, (c) 50 mm	90